Christian-Albrechts-Universität zu Kiel
Institut für Theoretische Physik und Astrophysik

Dissertation
zur Erlangung des Doktorgrades
der Mathematisch-Naturwissenschaftlichen Fakultät
der Christian-Albrechts-Universität zu Kiel

Dynamics of a Spherically Confined Yukawa Plasma: Shell Formation and Collective Excitations

vorgelegt von
Hanno Kählert

Kiel, 2011

Referent:	Prof. Dr. Michael Bonitz Christian-Albrechts-Universität zu Kiel
Korreferenten:	Prof. Dr. Hartmut Löwen Heinrich-Heine-Universität Düsseldorf
	Prof. Dr. James W. Dufty University of Florida, Gainesville
Tag der mündlichen Prüfung:	Di., 13. Dezember 2011
Zum Druck genehmigt:	Di., 13. Dezember 2011

Dekan

Abstract

The dynamics of spherical dust crystals created in a gaseous plasma (so-called “Yukawa Balls”) is investigated by means of first-principle simulations and an analytic “cold-fluid” theory. The analysis focuses on the dynamic formation of the characteristic shell structure and the collective excitations in the strongly coupled liquid state. It is based on a model of charged particles with screened Coulomb (Yukawa) interaction confined in an isotropic harmonic trap.

The emergence of the shell structure in spherically confined plasmas is analyzed by time-resolved Langevin dynamics and thermodynamic Monte Carlo simulations. The former are used to cool a Yukawa Ball from a weakly coupled initial state to a strongly coupled final state. In this scenario, shell formation generally begins at the outer plasma edge, but the screening parameter strongly determines the time for the formation of the shells inside the cluster. Monte Carlo simulations are then used to study other trapping potentials. It is found that the process can be initiated inside the plasma if the confinement is modified such that the particles cannot enter the inner region of the trap.

The second main topic concerns the collective modes of Yukawa Balls in the strongly coupled liquid phase. They are studied analytically by solving the linearized fluid equations for a cold plasma. In this “cold-fluid” theory, the mode spectrum of Yukawa Balls is fully characterized by three mode numbers and a single parameter describing the effective range of the interaction potential. Since the cold-fluid theory is based on the mean-field approximation and does not account for thermal effects, its results are compared with mode spectra from molecular dynamics (MD) simulations. The comparison shows that the cold-fluid theory accurately describes the low-order modes in systems with weak to moderate screening. Larger deviations, however, are observed for the high-order modes and in the strong screening regime. The MD simulations of strongly coupled Yukawa Balls further contain additional low-frequency excitations that are not predicted by the cold-fluid theory. Both the cold-fluid theory and the MD simulations yield additional insights into the properties of the “breathing mode” in a confined Yukawa plasma and thereby complement existing results in the literature.

Kurzfassung

Die Dynamik sphärischer Staubkristalle, die in einem gasförmigen Plasma hergestellt werden (sogenannte *Yukawa Bälle*), wird mit Hilfe von *first-principle* Simulationen und einer analytischen *Cold-Fluid* Theorie untersucht. Die Untersuchung befasst sich primär mit der dynamischen Entstehung der charakteristischen Schalenstruktur und den kollektiven Anregungen in der stark gekoppelten flüssigen Phase. Ihr liegt ein Modell geladener Teilchen zugrunde, die in einer isotropen harmonischen Falle eingeschlossen sind und mit einem abgeschirmten Coulomb (Yukawa) Potential wechselwirken.

Die Entstehung der Schalenstruktur in sphärisch eingeschlossenen Plasmen wird mit zeitaufgelösten Langevin-Dynamik und thermodynamischen Monte Carlo Simulationen untersucht. Die Ersteren werden verwendet, um einen Yukawa Ball aus einem schwach gekoppelten Anfangszustand in einen stark gekoppelten Endzustand zu überführen. In diesem Szenario beginnt der Aufbau der Schalenstruktur generell am äußeren Rand des Plasmas, der Abschirmparameter bestimmt jedoch maßgeblich den Zeitpunkt für die Entstehung der inneren Schalen. Monte Carlo Simulationen werden dann verwendet, um andere Einfangpotentiale zu untersuchen. Es zeigt sich hierbei, dass es möglich ist die Bildung der Schalenstruktur innerhalb des Plasmas auszulösen, wenn das äußere Potential derart verändert wird, dass die Teilchen das Zentrum der Falle nicht erreichen können.

Die kollektiven Moden von Yukawa-Bällen in der stark gekoppelten flüssigen Phase bilden das zweite Kernthema. Sie werden analytisch durch Lösen der linearisierten Fluidgleichungen für ein kaltes Plasma untersucht. In dieser *Cold-Fluid* Theorie wird das Modenspektrum eines Yukawa-Balls vollständig durch die Angabe von drei Modenzahlen und einem einzelnen Parameter, der die effektive Reichweite der Wechselwirkung beschreibt, bestimmt. Da die *Cold-Fluid* Theorie auf der *Mean-Field* Näherung basiert und keine thermischen Effekte berücksichtigt, werden ihre Resultate mit denen aus Molekulardynamik-Simulationen (MD) verglichen. Der Vergleich macht deutlich, dass die Theorie Moden niedriger Ordnung in Systemen mit schwacher Abschirmung gut beschreibt, dass jedoch bei Moden hoher Ordnung und bei starker Abschirmung größere Abweichungen auftreten. Die MD-Simulationen für stark gekoppelte Yukawa-Bälle enthalten darüber hinaus zusätzliche, niedrig-frequente Anregungen, die nicht von der *Cold-Fluid* Theorie vorhergesagt werden. Sowohl die *Cold-Fluid* Theorie als auch die MD-Simulationen liefern weitere Erkenntnisse über die Eigenschaften der “Breathing” Mode in einem eingeschlossenen Yukawa-Plasma und ergänzen damit bereits aus der Literatur bekannte Ergebnisse.

Contents

CHAPTER 1

Motivation and Outline

This work aims at a theoretical investigation of dynamic processes in "Yukawa Balls" [1]. These clusters are created in dusty plasma experiments at the universities in Kiel and Greifswald [2]. Dusty plasmas differ from ordinary plasmas by (i) the presence of macroscopic (μm-sized) particles in addition to the atomic constituents and (ii) their strong Coulomb interaction. The latter aspect brings the dust subsystem into the parameter regime of strongly coupled plasmas, which share many properties with liquids or even solids compared to weakly coupled plasmas with gas-like behavior. Dusty plasma physics constitutes a wide field of research because it combines the strong coupling of the dust component with the properties of the weakly coupled background plasma. This leads to interesting phenomena caused by the interplay between the different particle species.

The distinctive property of Yukawa Balls is their spherical shell structure, which is a consequence of the experimental confinement conditions and the strong dust-dust interaction [3]. Due to the universal behavior of strongly coupled plasmas, similar particle arrangements are found in experiments with (spherically) confined ions [4, 5] and simulations of ultracold neutral plasmas [6, 7]. The latter revealed a fundamental difference regarding the order of shell formation: While shell formation was found to proceed outward starting near the core in ultracold neutral plasmas [6], the opposite direction was observed in trapped ions [8]. A central concern of this thesis is to study the dynamic formation of the shell structure and the associated correlation buildup in Yukawa Balls. Further, the influence of the confinement potential on the order of shell formation in strongly coupled plasmas is investigated.

The normal modes of finite plasmas, which are the counterparts of waves in extended systems, constitute the second main topic of this thesis. They determine the linear response to external fields and the fluctuation spectra in unperturbed systems, i.e., they carry valuable information about the plasma properties. In *crystalline* Yukawa plasmas, the normal modes are well explained by the harmonic approximation of the potential energy [9, 10]. The second part of this thesis is concerned with the collective modes of Yukawa Balls in the strongly coupled *liquid* phase, which resemble the dust acoustic wave in a uniform dusty plasma [11, 12]. As a special excitation of spherical clusters, the "breathing"

mode (a radial expansion and contraction of the system) is studied in further detail. While the existence conditions [13] and the temperature dependence [14] for uniform breathing modes have been studied, deviations from this behavior have been demonstrated for harmonically confined Yukawa systems [13]. The main goals of the analysis are the determination and classification of collective excitations in Yukawa Balls and to further study the modifications of the breathing mode.[1]

Thesis Outline

- Chapter 2 serves as a brief survey on the physics of strongly coupled plasmas and discusses a few examples with particular relevance for this work. This is followed by an introduction to the properties of dusty plasmas in general and Yukawa Balls in particular.
- Chapter 3 deals with the methods for the theoretical investigation of a strongly coupled dusty plasma. The first part reviews how the dielectric response formalism can be employed to include the screening properties of the plasma environment in an effective interaction potential between the dust grains. In the second part, the derivation of the plasma fluid equations is outlined, with special emphasis on the involved approximations and their applicability to the determination of collective plasma modes. The algorithms utilized for the numerical simulation of Yukawa Balls are discussed in the third part. Results obtained with these methods are reported in Chapters 4–6.
- In Ch. 4, Langevin dynamics simulations are used to study the time-dependent correlation buildup in Yukawa Balls. The focus lies on the formation of the shell structure. In addition, Monte Carlo simulations are performed to investigate density profiles in other confinement potentials and to determine their influence on the emergence of concentric shells in strongly coupled plasmas.
- Chapters 5 and 6 are concerned with the collective excitations of Yukawa Balls. A continuum theory for the normal modes of Yukawa Balls based on the cold-fluid equations is presented in Ch. 5. Its results are compared with previous theories for harmonically confined particles with long-range Coulomb and short-range Dirac delta interaction. The eigenfrequency spectrum and the eigenmodes of Yukawa Balls are discussed in detail.
- The results of the cold-fluid theory are compared with molecular dynamics simulations in Ch. 6. They reveal the complete excitation spectrum of Yukawa Balls, which includes additional modes not predicted by the fluid approach. Furthermore, the eigenmodes of crystallized plasmas are computed to investigate the breathing mode and the temperature dependence of its frequency in more detail.
- The thesis concludes with a summary of the main results in Ch. 7. Some supplementary mathematical details are presented in the Appendix.

[1] The relevant publications for the results presented in this thesis are indicated at the end of Chapters 4–6. A complete list can be found in the List of Publications.

CHAPTER 2

Introduction

The general properties and phenomena associated with strongly coupled plasmas are reviewed in the first part of this chapter. In particular, the Coulomb coupling parameter is introduced as the key quantity for the classification of plasmas with respect to the importance of inter-particle correlations. The discussion of a few examples for strongly coupled plasmas is complemented by a closer inspection of the properties of dusty plasmas and Yukawa Balls in the second part.

2.1 Strongly Coupled Plasmas

2.1.1 Coupling Parameter

The classification of classical plasmas into the weak and strong coupling regime is based on the Coulomb coupling parameter [15][1]

$$\bar{\Gamma} = \frac{q^2 / a_{\mathrm{ws}}}{k_{\mathrm{B}} T}, \tag{2.1}$$

where the Wigner-Seitz radius $a_{\mathrm{ws}} = \sqrt[3]{3/4\pi n}$ is a typical inter-particle distance in a plasma with density n. It measures the characteristic potential energy of two adjacent particles (q^2/a_{ws}) in units of the thermal energy ($k_{\mathrm{B}}T$), where q denotes the particles' charge, k_{B} Boltzmann's constant, and T the temperature.

The hot plasmas in the sun or in fusion reactors are weakly coupled plasmas with $\bar{\Gamma} \ll 1$. They are mostly dominated by collective effects due to the long-range Coulomb interaction, and the weak collisional effects are caused by many small-angle collisions [16]. These plasmas exhibit no internal structure, and their thermodynamic behavior is well described by the ideal gas law [15]. On the other hand, strongly coupled plasmas ($\bar{\Gamma} \gtrsim 1$) have liquid-like features and may even undergo a phase transition toward the solid state, see, e.g., Ref. [17].

[1] The overbar is introduced to distinguish the macroscopic coupling constant ($\bar{\Gamma}$) from the corresponding parameter (Γ) in finite Yukawa Balls, which will be used throughout this work.

The plasmas considered in this work are classical. However, quantum effects may become important at high densities or low temperatures—depending on the value of the quantum degeneracy parameter $\chi(n, T, m)$, where m denotes the particles' mass [18]. In this regime, the classical coupling parameter (2.1) must be replaced by the Brueckner parameter $r_s \sim q^2/(a_{\mathrm{ws}} E_{\mathrm{F}})$, where the Fermi energy E_{F} has been substituted for $k_{\mathrm{B}} T$ [17].

Theoretically, many properties of strongly coupled plasmas have been obtained from investigations of the one-component plasma (OCP) model ("…a system consisting of a single species of charged particles embedded in a uniform background of neutralizing charges" [15]). The properties of the classical OCP are solely determined by the coupling parameter $\bar{\Gamma}$, which makes it an ideal system for studying the transition from weak to strong coupling without the influence of other effects. Its natural extension is the Yukawa OCP with a polarizable background, see, e.g., Ref. [19].

In the strong coupling regime, the (Yukawa) OCP shows several remarkable phenomena, such as the existence of shear modes and viscosity [20–23], negative mode dispersion [11, 20], anomalous diffusion (in two-dimensional layers) [24, 25], or a liquid-solid phase transition [26].

2.1.2 Examples

Since the coupling parameter (2.1) depends on several plasma variables (n, T, q), the strong coupling regime can be reached in various ways. Consequently, there exists a great variety of plasmas that are affected by strong correlations. The charge states are typically low, which leaves the density and the temperature to achieve the necessary conditions.

Non-neutral plasmas composed of a single particle species can be realized in Paul or Penning traps, see Ref. [5] for an overview. In such experiments, ions are laser-cooled to very low temperatures in the mK regime, which allows for the creation of highly correlated systems. They constitute experimental plasmas in which the assumptions of the OCP are satisfied to a great extent, because the harmonic trapping potential mimics the properties of a homogeneous background [5]. The finite system size, however, leads to the formation of concentric shells near the crystallization temperature in addition to (or instead of) the bcc lattice structure of infinite Coulomb systems—depending on the particle number [4, 8, 27], see Fig. 2.1.

Strong ionic correlations are also present in so-called warm dense matter (WDM). A recent overview on the properties of these plasmas can be found in Ref. [28]. As a consequence of its high (solid matter) density and low temperature, WDM is characterized by quantum degenerate electrons and strongly coupled classical ions, which makes a theoretical treatment particularly challenging, see also Ref. [29]. Such plasmas are naturally found inside giant planets or white dwarf stars but are also relevant to inertial confinement fusion [28, 30]. X-ray Thomson scattering provides valuable information about their properties from laboratory experiments [31].

Ultracold neutral plasmas constitute another class of plasmas with strong ion coupling, see Ref. [7] for a review. They are created by photoionization of laser-cooled neutral atoms in magneto-optical traps. This produces an expanding plasma cloud with a lifetime of about 100 μs [33]. Measurements of the time-dependent plasma density and temperature

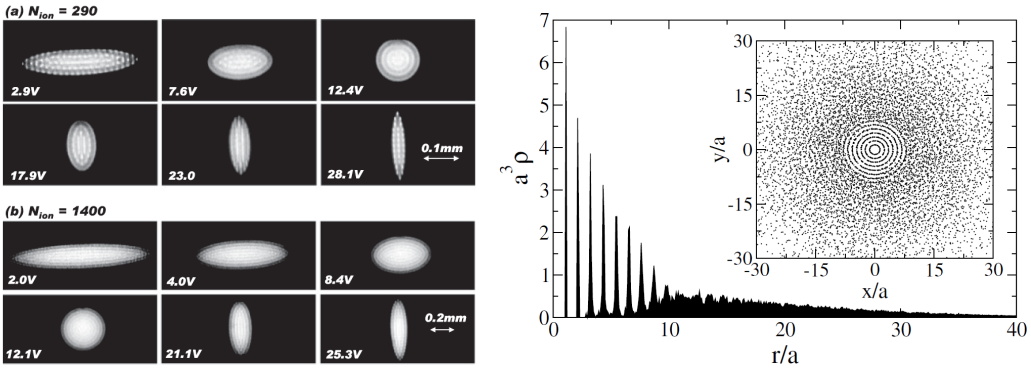

Figure 2.1: Left: CCD images of ion crystals of various shapes in a linear Paul trap. (Reprinted with permission from [32]. Copyright 2010 by the American Physical Society). Right: Radial ion density in a simulation of an ultracold neutral plasma showing the formation of spherical shells. (Reprinted with permission from [6]. Copyright 2004 by the American Physical Society.)

yield information about the equilibration properties [34] and collective phenomena [35]. Strong ion correlations manifest themselves as oscillations of the kinetic energy [7, 34]. Even though the formation of highly correlated ions is usually hampered by the initial disorder of the system, simulations show that crystallization should become feasible by laser-cooling the ions in the expansion phase [6], see Fig. 2.1.

For a summary of various strongly coupled plasmas in a density-temperature phase diagram, the interested reader is referred to Refs. [7, 36].

2.2 Dusty Plasmas

2.2.1 General Properties

Plasmas enriched with small (sub) micron-sized particles are known as dusty plasmas. They are found in, e.g., many space environments, humble candle flames, and (possibly) in ball lightning [37, 38], see Ref. [39]. Today, dusty plasmas are routinely produced in rf or dc discharges in laboratory experiments by particle injection into the plasma. As a result of their interaction with the plasma environment (electrons, ions and neutrals), the dust grains become highly charged with thousands of electrons. Despite the low dust density and relatively high temperatures (for Yukawa Balls, $n_\mathrm{d} \sim 3\,\mathrm{mm}^{-3}$ and $T_\mathrm{d} \sim 300-400\,\mathrm{K}$, see Refs. [1, 10, 40]), the enormous charges lead to coupling strengths well within the parameter regime of strongly coupled plasma physics.

Compared to plasmas where the ions represent the strongly correlated component, the timescale for the dynamics of the dust particles is slowed down by several orders of magnitude. In combination with their size and the low particle density, this allows for a direct optical observation of their trajectories. The possibility of obtaining the complete phase space information and thus all correlation properties offers unique experimental advantages over other strongly coupled systems [41]. Even though similar favorable aspects ap-

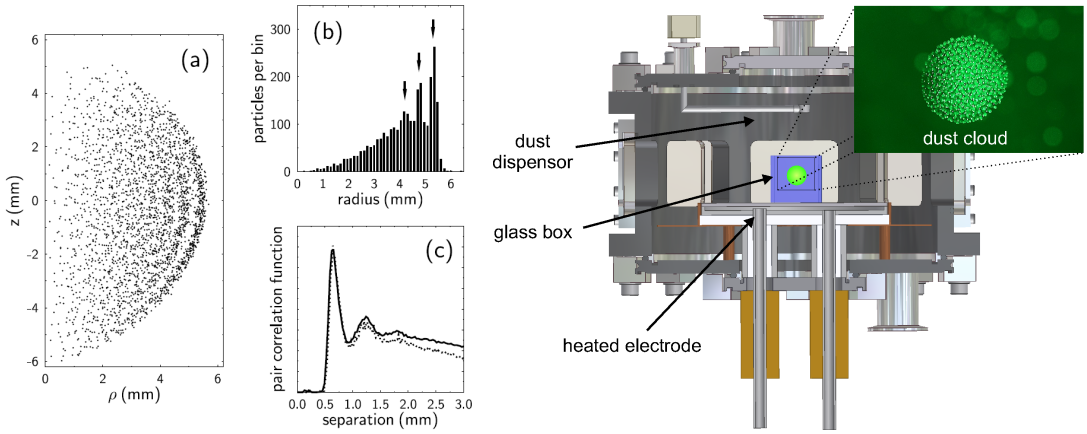

Figure 2.2: Left: Structural properties of a Yukawa Ball with 2823 particles: (a) particle positions in cylindrical coordinates, (b) radial particle histogram, (c) pair correlation function. The data reveal the existence of spherical shells and strong correlations. (Reprinted with permission from [1]. Copyright 2004 by the American Physical Society.) Right: Experimental setup showing the dielectric glass box on the heated electrode for the confinement of Yukawa Balls. (From [43]. Figure kindly provided by D. Block.)

ply to colloidal dispersions [42], they are subject to heavy damping, and are less suited for the investigation of dynamic processes on short timescales. On the other hand, they have other advantages, such as perfectly attained equilibrium conditions, and thus contribute different (complementary) aspects to the study of classical systems at a kinetic level, see Ref. [42].

2.2.2 Yukawa Balls: Spherical Dust Clusters

Yukawa Balls are spherically confined dust clouds and were created for the first time by Arp *et al.* in 2004 [1], see Fig. 2.2. Due to their pronounced shell structure, they can be regarded as the dusty plasma analog of spherical ion crystals, cf. Sec. 2.1.2. Compared to the latter, Yukawa Balls allow for a fully kinetic investigation of structural and dynamic phenomena in finite three-dimensional plasmas under the influence of strong correlations.

The experimental setup for Yukawa Balls requires modifications to the conventional design used for the confinement of two-dimensional crystals [1, 3], see Fig. 2.2. In comparison to the light plasma components, the dust particles are severely affected by gravity, which must be compensated for a proper vertical confinement. For this purpose, the lower electrode is heated, which generates an upward thermophoretic force that is complemented by the electric field force. The application of this method often goes along with the formation of a dust-free "void" region due to an outward ion flow, see Ref. [44] for a recent investigation. A glass box on the lower electrode avoids this phenomenon in Yukawa Balls [1]. The combination of all the various forces (electric field, thermophoresis, gravity, ion-drag) was shown to provide an isotropic harmonic trap for the dust particles [3].

Since their discovery, the ground and metastable states of Yukawa Balls [45–48] and their normal modes [10] have been analyzed experimentally. In the last few years, there has

also been considerable progress regarding the particle observation techniques. They have evolved from scanning video microscopy [1, 3] to stereoscopic [49] and holographic methods [50] toward a combination of the latter two [51], see also Ref. [2].

Yukawa Ball experiments with larger particles and at lower gas pressure have been performed by Kroll *et al.* [52]. The clusters created in their experiments are characterized by two forms of competing order: a shell-like order induced by the confinement and the formation of vertical strings. They have shown that the latter is due to the presence of an ion wake below the dust grains caused by a downward ion flow. Its implication on the interaction potential between the dust particles in Yukawa Balls is discussed in Sec. 3.1. Anisotropic clusters have recently been studied by Killer *et al.* [53].

CHAPTER 3

Theoretical Background and Simulation Methods

This chapter deals with the theoretical methods for the investigation of a strongly coupled dusty plasma. The various particle species in the multi-component system make a consistent theoretical description of a dusty plasma very difficult. For this reason, the first part reviews how the inclusion of the light particles into an effective interaction potential between the heavy dust grains [54] helps to circumvent this problem (Sec. 3.1). This is accompanied by a discussion of the model Hamiltonian for Yukawa Balls.

Section 3.2 briefly discusses the derivation of the cold-fluid equations. They serve as the basis for the analytic investigation of collective modes in Ch. 5. The applicability of the fluid equations to the analysis of plasma waves is discussed.

Molecular dynamics and Monte Carlo simulations allow for a numerically exact treatment of the model system. In addition to the former method, a Langevin dynamics simulation accounts for the presence of frictional forces caused by the neutral gas and extends the range of applications to dusty plasmas. The concepts of these methods are discussed in Sec. 3.3. They are employed to study the shell formation dynamics in Yukawa Balls (Ch. 4) and their collective excitations (Ch. 6).

3.1 Model System

Maxwell's equations form the basis for the calculation of the electric and magnetic fields in a plasma. They are coupled to Newton's equations of motion via the Lorentz force. The combined set of equations determines the dynamics of the (classical) plasma particles under the influence of the electromagnetic fields. However, the different timescales for the dynamics of electrons, ions, and dust grains make a direct numerical solution of these equations extremely difficult. It is therefore necessary to use a simplified physical model which is less demanding but at the same time captures the essential physics involved in the process of interest. The focus thereby lies on a proper description of the dust dynamics.

In the following, it will be reviewed how the complexity of the system can be reduced, and the effect of the light particles (electrons, ions and neutrals) can be integrated into an

effective potential for the interaction between the heavy dust grains [29, 54]. This procedure reduces the system to a single component and only requires the solution of Newton's equations for the dust component, while plasma effects are retained in the pair potential. The important effect of dust-neutral collisions can directly be incorporated into the equation of motion, which leads to the Langevin method, see Sec. 3.3.2.

3.1.1 Dust Interaction Potential

The Plasma as a Dielectric Medium

The properties of highly charged massive dust particles are mainly determined by their electrostatic interactions, and the effect of internal magnetic fields on their dynamics is negligible. The ions and electrons can be eliminated from the equations by treating them as a (possibly anisotropic) dielectric medium with a frequency (ω) and wavenumber ($\boldsymbol{k}$) dependent dielectric tensor $\epsilon_{\alpha\beta}(\boldsymbol{k},\omega)$ ($\alpha,\beta \in \{x,y,z\}$) that describes their response to the perturbation induced by the dust grains [55]. Linear response theory can then be used to calculate the shielded potential of a moving test charge, $\phi(\boldsymbol{r},t)$ (e.g., Refs. [54, 56–59]).

In the dielectric formalism, Gauss' law becomes [55]

$$\nabla \cdot \boldsymbol{D}(\boldsymbol{r},t) = 4\pi\rho_\mathrm{d}(\boldsymbol{r},t), \tag{3.1}$$

where $\boldsymbol{D}(\boldsymbol{r},t)$ is the dielectric displacement, and the right-hand-side of the equation involves only the *dust* charge density $\rho_\mathrm{d}(\boldsymbol{r},t)$. Due to the simple relation between the dielectric displacement and the electric field in Fourier space, $\hat{\boldsymbol{D}}_\alpha(\boldsymbol{k},\omega) = \sum_\beta \epsilon_{\alpha\beta}(\boldsymbol{k},\omega)\hat{\boldsymbol{E}}_\beta(\boldsymbol{k},\omega)$, Eq. (3.1) is readily solved by a Fourier transform [55]. The result for a single (dust) particle with charge q moving at a velocity $\boldsymbol{u}_\mathrm{d}$ is the dynamically screened potential [29]

$$\phi(\boldsymbol{r},t) = \int \frac{d\boldsymbol{k}}{2\pi^2}\frac{q}{k^2}\frac{e^{i\boldsymbol{k}\cdot(\boldsymbol{r}-\boldsymbol{u}_\mathrm{d}t)}}{\epsilon(\boldsymbol{k},\boldsymbol{k}\cdot\boldsymbol{u}_\mathrm{d})}, \tag{3.2}$$

where the full linear response of the electrons and ions is now contained in the longitudinal dielectric permittivity [55] (or dielectric function)

$$\epsilon(\boldsymbol{k},\omega) \equiv \sum_{\alpha,\beta}\frac{k_\alpha k_\beta}{k^2}\epsilon_{\alpha\beta}(\boldsymbol{k},\omega).$$

The electric field of the test particle simply follows from $\boldsymbol{E}(\boldsymbol{r},t) = -\nabla\phi(\boldsymbol{r},t)$.

Equation (3.2) involves the Fourier transform of the unscreened Coulomb potential, $\hat{\phi}_\mathrm{C}(k) = 4\pi q/k^2$, which is shielded by the ambient plasma. Since Maxwell's equations are linear, the full potential of N particles is just the sum of the individual potentials. This makes the dielectric response approach particularly interesting for the numerical simulation of the dynamics of a large collection of dust particles [54, 59, 60], where more elaborate Particle-in-Cell based simulations [61] reach their computational limitations.

Ion Wake Effects

The particular form of the dielectric function depends on the plasma properties. For a collisionless Maxwellian plasma, it can be derived from the Vlasov equation, see, e.g., Ref. [16], while the inclusion of ion-neutral collisions requires the addition of a collision term to the kinetic equation [55]. In many dusty plasma experiments, electric fields create a downward ion flow (e.g., Ref. [62]), which can be incorporated into the dielectric function by using a shifted Maxwellian velocity distribution [63]. For electrons, these effects are negligible due to their high thermal velocities. They are typically treated in the static approximation, see Ref. [63] for an overview.

The dielectric function for a plasma with streaming ions yields an anisotropic wake-field potential with non-reciprocal forces and several minima and maxima behind the test charge—depending on the electron-ion temperature ratio, the ion Mach number, and the pressure [54, 59, 63]. It has further been shown that the ion flow causes instabilities in the dust subsystem [54, 60, 64, 65]. Additional effects such as magnetized ions [66–68] can be included in the linear response model.

3.1.2 Yukawa Balls

Interaction Potential

The first experiments with Yukawa Balls were performed at a rather high gas pressure of about $20-120\,\mathrm{Pa}$ [3]. Under these conditions, the emergence of the ion focus behind the grains is suppressed due to the high ion-neutral collision rate [2]. Further, the dust is confined near the bulk region of the plasma, where the ion flow velocity is lower than in the sheath [3]. Then, the effect of streaming ions in the dielectric response may be neglected, and a static approximation can be used [46], i.e. [16],

$$\epsilon(\boldsymbol{k}, \boldsymbol{k}\cdot\boldsymbol{u}_\mathrm{d}) \approx \epsilon(\boldsymbol{k}, 0) = 1 + \frac{1}{k^2\lambda_\mathrm{De}^2} + \frac{1}{k^2\lambda_\mathrm{Di}^2}, \qquad |\boldsymbol{u}_\mathrm{d}| \ll v_\mathrm{e}, v_\mathrm{i}. \tag{3.3}$$

Here, the electron and ion thermal velocities and Debye lengths are $v_\mathrm{e,i} = (k_\mathrm{B}T_\mathrm{e,i}/m_\mathrm{e,i})^{1/2}$ and $\lambda_\mathrm{De,Di} = (k_\mathrm{B}T_\mathrm{e,i}/4\pi n_0 e^2)^{1/2}$, respectively. Their common density (n_0) and respective temperatures ($T_\mathrm{e,i}$) determine the shielding properties of the background plasma. Electron and ion masses are denoted by $m_\mathrm{e,i}$, while e is the elementary charge.

The resulting electrostatic potential from Eq. (3.2) is the Yukawa (or Debye-Hückel) potential [16]

$$\phi(\boldsymbol{r}, t) = \frac{q}{|\boldsymbol{r} - \boldsymbol{u}_\mathrm{d}t|}\exp\left(-|\boldsymbol{r} - \boldsymbol{u}_\mathrm{d}t|/\lambda_\mathrm{D}\right), \qquad |\boldsymbol{u}_\mathrm{d}| \ll v_\mathrm{e}, v_\mathrm{i}, \tag{3.4}$$

where $\lambda_\mathrm{D} = \lambda_\mathrm{De}\lambda_\mathrm{Di}/(\lambda_\mathrm{De}^2 + \lambda_\mathrm{Di}^2)^{1/2}$ is the combined Debye length of electrons and ions. Equation (3.4) accounts for the relative motion of the particle with respect to the background but neglects the *dynamic* shielding of the environment, i.e., the plasma responds adiabatically. Although the linear response approach may be questionable in the absence of streaming [63], the Yukawa model is widely used in the literature and successfully describes the properties of Yukawa Balls at high pressure [46].

As already mentioned in Sec. 2.2.2, more recent Yukawa Ball experiments have been performed with hollow glass spheres at significantly lower gas pressure ($p \sim 0.5 - 6\,\mathrm{Pa}$) [52]. This reduces the ion-neutral collision rate and consequently the ion flow can no longer be disregarded. The result is a chain-like ordering of dust particles, where the typical shell structure of Yukawa Balls remains detectable only in the outer region of the cloud [52], see also Ref. [53]. Besides the ion-neutral collision rate, also the dust-neutral friction coefficient is decreased at lower gas pressure. This makes the observation of dynamic phenomena easier because the dust motion is significantly less damped [52].

Hamiltonian

In this work, the effects of the ion flow are neglected, and the grains are assumed to have identical charge (q) and mass (m). The Hamiltonian for spherical Yukawa Balls composed of N particles then reads [46]

$$H = \sum_{i=1}^{N} \frac{\boldsymbol{p}_i^2}{2m} + \underbrace{\sum_{i=1}^{N} V(|\boldsymbol{r}_i|) + \frac{1}{2}\sum_{i\neq j}^{N} v(|\boldsymbol{r}_{ij}|)}_{U(\boldsymbol{r}_1,\ldots,\boldsymbol{r}_N)}, \tag{3.5}$$

where $\boldsymbol{r}_{ij} = \boldsymbol{r}_i - \boldsymbol{r}_j$, and the sum of the confinement and the interaction energy yields the total potential energy $U(\boldsymbol{r}_1,\ldots,\boldsymbol{r}_N)$. Explicitly, the isotropic confinement [3] and interaction potentials are given by [46]

$$V(r) = \frac{m}{2}\omega_0^2 r^2, \qquad v(r) = \frac{q^2}{r}\exp(-\kappa r), \tag{3.6}$$

respectively. The frequency of the harmonic trap is denoted by ω_0, and the screening parameter is $\kappa = \lambda_\mathrm{D}^{-1}$. In the limit $\kappa = 0$ ($\lambda_\mathrm{D} \to \infty$), the Yukawa potential reduces to the unscreened Coulomb potential, and the Hamiltonian (3.5) is frequently applied to investigate the properties of confined ions, e.g., Refs. [69, 70].

This simple model has been shown to reproduce the experimentally observed concentric shell structures with the correct occupation numbers [46] and the occurrence probability of metastable states [47, 71]. Here, it turned out that a Hamiltonian description without dissipation is not sufficient to reproduce the experimental results, and damping by neutrals must be taken into account, see Sec. 3.3.2.

The ground states of the Hamiltonian (3.5) for Coulomb and Yukawa interaction have been analyzed extensively with simulations [69, 72–75] and analytical theories [76–78]. Their typical shell structure has led to the development of simplified shell models [69, 72, 79, 80]. They accurately predict the occupation numbers and shell radii of the exact ground states for Coulomb interaction, but more work is required for Yukawa systems [76, 81]. While an improved shell model for such systems has been derived in Ref. [82], a wider class of confining potentials has been addressed in Ref. [83]. Further theoretical studies include the investigation of melting transitions [70, 84–86], normal modes [9, 13, 74], and density profiles at finite temperature [87–90].

Simulations with the full ion wake potential for confined systems have been performed, e.g., in Refs. [54, 59, 60]. This is expected to be necessary for the analysis of very low pressure Yukawa Ball experiments such as those of Kroll *et al.* [52].

3.2 Theoretical Methods

In order to study the collective excitations of Yukawa Balls analytically, one needs to use suitable approximations for the dynamic equations of motion of the complicated N-body problem. The Liouville equation of Classical Mechanics is a convenient and often used starting point [16]. In the following, the approximations involved in the derivation of the cold-fluid equations are discussed—mainly based on Refs. [16, 91]. They are used for the calculation of the normal modes of spherical Yukawa Balls in Ch. 5.

3.2.1 BBGKY Hierarchy

The BBGKY (Bogolyubov–Born–Green–Kirkwood–Yvon) hierarchy converts the exact Liouville equation for the N-particle distribution function $f^{(N)}(\boldsymbol{r}^N, \boldsymbol{p}^N, t)$ into a set of coupled equations for the reduced distribution functions $f^{(n)}(\boldsymbol{r}^n, \boldsymbol{p}^n, t)$, where $n \leq N$.[1] The latter are obtained by integration of $f^{(N)}$ over a subset of $N-n$ degrees of freedom [91]. Even though the hierarchy itself is equally complex as the Liouville equation, closure relations can be used to derive simpler (manageable) equations [16, 91].

For the derivation of the fluid equations, the first equation for the one-particle distribution function $f^{(1)}(\boldsymbol{r}, \boldsymbol{p}, t) \equiv f$ is needed. It is linked to the second equation of the hierarchy via the two-particle distribution function $f^{(2)}(\boldsymbol{r}, \boldsymbol{p}, \boldsymbol{r}', \boldsymbol{p}', t)$, which is required for the evaluation of the interaction term. The latter can be expressed as an uncorrelated part (product of two one-particle distribution functions) and the two-particle correlation function $c(\boldsymbol{r}, \boldsymbol{p}, \boldsymbol{r}', \boldsymbol{p}', t)$ as [16]

$$f^{(2)}(\boldsymbol{r}, \boldsymbol{p}, \boldsymbol{r}', \boldsymbol{p}', t) = f(\boldsymbol{r}, \boldsymbol{p}, t) f(\boldsymbol{r}', \boldsymbol{p}', t) + c(\boldsymbol{r}, \boldsymbol{p}, \boldsymbol{r}', \boldsymbol{p}', t).$$

The first equation of the hierarchy [91] can then be written as [18]

$$\left[\frac{\partial}{\partial t} + \frac{\boldsymbol{p}}{m} \cdot \frac{\partial}{\partial \boldsymbol{r}} - \frac{\partial U}{\partial \boldsymbol{r}} \cdot \frac{\partial}{\partial \boldsymbol{p}}\right] f(\boldsymbol{r}, \boldsymbol{p}, t) = \iint \frac{\partial}{\partial \boldsymbol{r}} v(|\boldsymbol{r} - \boldsymbol{r}'|) \cdot \frac{\partial}{\partial \boldsymbol{p}} c(\boldsymbol{r}, \boldsymbol{p}, \boldsymbol{r}', \boldsymbol{p}', t)\, d\boldsymbol{r}' d\boldsymbol{p}', \tag{3.7}$$

where $U(\boldsymbol{r}, t) = V(r) + q\phi(\boldsymbol{r}, t)$ is an effective one-particle potential composed of the external harmonic confinement (V) and the mean-field potential produced by the particles themselves (Yukawa interaction v). The latter is given by [91]

$$q\phi(\boldsymbol{r}, t) = \iint v(|\boldsymbol{r} - \boldsymbol{r}'|) f(\boldsymbol{r}', \boldsymbol{p}', t)\, d\boldsymbol{p}' d\boldsymbol{r}' \equiv \int v(|\boldsymbol{r} - \boldsymbol{r}'|) n(\boldsymbol{r}', t)\, d\boldsymbol{r}', \tag{3.8}$$

where the second equality defines the one-particle density $n(\boldsymbol{r}, t)$, see Sec. 3.2.2.

The right-hand side of Eq. (3.7)—the so-called collision integral $I(\boldsymbol{r}, \boldsymbol{p}, t)$ [18, Ch. 3]—accounts for the corrections to the dynamics arising from discrete particle effects, see Refs. [16, 91] for a detailed discussion. Dust-neutral collisions could be incorporated by means of a Fokker-Planck collision operator [14], cf. Sec. 3.3.2.

[1] The vectors $\boldsymbol{r}^n$ and $\boldsymbol{p}^n$ refer to the coordinates and momenta of n particles.

3.2.2 Fluid Equations

The fluid equations constitute a further simplification of more general kinetic equations. Instead of calculating the full one-particle distribution function, they reduce the problem to finding solutions for its (low-order) moments [16], e.g.,[2]

$$\langle \boldsymbol{p} \rangle \equiv \frac{1}{n(\boldsymbol{r},t)} \int \boldsymbol{p}\, f(\boldsymbol{r},\boldsymbol{p},t)\, d\boldsymbol{p} \equiv m\,\boldsymbol{u}(\boldsymbol{r},t), \qquad n(\boldsymbol{r},t) \equiv \int f(\boldsymbol{r},\boldsymbol{p},t)\, d\boldsymbol{p}. \tag{3.9}$$

The first moment is associated with the (macroscopic) fluid velocity $\boldsymbol{u}(\boldsymbol{r},t)$, where the one-particle density $n(\boldsymbol{r},t)$ is required for a proper normalization [see also Eq. (3.8)]. Dynamic equations for the moments can be obtained in a straightforward manner from Eq. (3.7). They represent another hierarchy of equations coupling successive moments of the distribution function—similar to the BBGKY hierarchy [16].

In many cases, only the first two equations for the density and the velocity are considered. Upon multiplying Eq. (3.7) by unity and $\boldsymbol{p}$, followed by an integration over $\boldsymbol{p}$, the continuity and the momentum equation can be derived [16]. This leads to ($\nabla = \partial/\partial \boldsymbol{r}$)

$$\frac{\partial n}{\partial t} + \nabla \cdot (n\boldsymbol{u}) = 0, \tag{3.10a}$$

$$m \frac{\partial}{\partial t}(n\boldsymbol{u}) + \frac{1}{m} \nabla \cdot \big(n \langle \boldsymbol{p} \otimes \boldsymbol{p} \rangle\big) = -n \nabla U + \boldsymbol{K}, \tag{3.10b}$$

where $\langle \ldots \rangle$ denotes a momentum average over f [Eq. (3.9)], $\otimes$ the dyadic product, and $\boldsymbol{K}$ the contribution from the collision integral. They are coupled to Eq. (3.8) for the electrostatic potential $\phi(\boldsymbol{r},t)$ that is contained in $U(\boldsymbol{r},t)$. For Yukawa systems, $\phi(\boldsymbol{r},t)$ can also be calculated from the *screened* Poisson equation [76]

$$\big(\Delta - \kappa^2\big)\phi(\boldsymbol{r},t) = -4\pi q n(\boldsymbol{r},t). \tag{3.11}$$

3.2.3 Closure Relations and Application to Waves

The momentum equation (3.10b) has two essential drawbacks: First, the quantity $\boldsymbol{K}$ is not known explicitly because it contains the correlation function c which, in turn, is determined by the higher order equations of the BBGKY hierarchy. Second, the momentum tensor $\langle \boldsymbol{p} \otimes \boldsymbol{p} \rangle$ is coupled to the higher order moments of f. While there exist methods to approximate these terms, a particularly simple form can be obtained by neglecting thermal and correlation effects entirely.

Mean-Field Approximation

In the mean-field (Vlasov) approximation, the BBGKY hierarchy is truncated by the assumption of completely uncorrelated particle motion, i.e., $c(\boldsymbol{r},\boldsymbol{p},\boldsymbol{r}',\boldsymbol{p}',t) \equiv 0$. The result is the famous Vlasov equation [16, 91], cf. Eq. (3.7). In this case, the inter-particle forces are solely determined by the mean-field potential (3.8). For the momentum equation (3.10b) this implies $\boldsymbol{K} = 0$.

[2] The normalization in Ref. [16] uses velocities instead of momenta.

For weakly coupled plasmas ($\bar{\Gamma} \ll 1$), this is usually a good approximation. However, especially for coupling parameters on the order $\bar{\Gamma} \gtrsim 1$, the particles begin to exhibit short-range correlations with their nearest neighbors, which become increasingly important and more long-ranged at stronger coupling. Under these conditions, the existence of the underlying potential landscape becomes apparent and can even lead to the "caging" of particles in potential wells created by the other particles [92, 93]. For many problems, it then becomes essential to find an adequate approximation for the (dynamic) correlation function, e.g., by resorting to results in the static limit [94, 95].

Cold-Fluid Limit

In the cold-fluid approximation, the hierarchy of fluid equations is closed by approximating the one-particle distribution function as $f(\boldsymbol{r},\boldsymbol{p},t) \approx n(\boldsymbol{r},t)\delta(\boldsymbol{p}-m\boldsymbol{u}(\boldsymbol{r},t))$, see Ref. [16]. This assumes that all particles at point $\boldsymbol{r}$ move at the same speed and neglects any superimposed thermal motion. The second-order momentum average then simplifies considerably, $\langle \boldsymbol{p}\otimes\boldsymbol{p}\rangle = m^2(\boldsymbol{u}\otimes\boldsymbol{u})$, and Eq. (3.10b) reduces to [16]

$$m\left[\frac{\partial \boldsymbol{u}}{\partial t} + (\boldsymbol{u}\cdot\nabla)\boldsymbol{u}\right] = -\nabla U, \tag{3.12}$$

where Eq. (3.10a) has been used. Improvements are possible by, e.g., giving the particles an isotropic finite-width velocity distribution in addition to $\boldsymbol{u}(\boldsymbol{r},t)$, which would lead to thermal pressure forces in Eq. (3.12) [16].

Contrary to the mean-field treatment of the interactions, the neglect of thermal effects is typically a reasonable approximation in a strongly coupled plasma , see the following discussion.

Dispersion Relation in an Uncorrelated Cold Yukawa Plasma

Within the approximations introduced above, the dispersion relation for the dust acoustic wave in a Yukawa model is (e.g., Ref. [19])

$$\omega(k) = \omega_\mathrm{p}\sqrt{\frac{k^2}{k^2+\kappa^2}}, \tag{3.13}$$

see Refs. [96, 97] for a more general overview on waves in dusty plasmas. Here, $\omega_\mathrm{p} = \sqrt{4\pi q^2 n/m}$ is the dust plasma frequency and n the uniform dust density. It is briefly shown in Ch. 5 how the result can be derived from the cold-fluid equations.

Compared to the dispersion relation in a Coulomb plasma ($\kappa \equiv 0$ and $\omega \equiv \omega_\mathrm{p}$), the wave is acoustic in the long-wavelength regime, $\omega \sim c_\mathrm{s}k$, where $c_\mathrm{s} = \omega_\mathrm{p}/\kappa$ is the dust acoustic speed [19, 96]. The relation (3.13) is valid for a weakly coupled plasma when thermal effects are negligible. Since the mean-field treatment is appropriate for a weakly correlated plasma with $\bar{\Gamma} \ll 1$, but the neglect of thermal motion requires a cold plasma, these conditions are hard to satisfy simultaneously. Consequently, both strong correlations [11, 95, 98, 99] and finite temperature effects [98, 100] lead to a modification of the

acoustic speed and the dispersion relation. Furthermore, the former give rise to shear waves [12, 98, 99]; see the review articles by Donkó *et al.* [19] and Piel and Melzer [97].

In the strong coupling regime, the quasi-localized charge approximation (QLCA) developed by Kalman and Golden [101] provides a good description of the dispersion relation [12, 19]. It neglects thermal pressure forces (the so-called "direct thermal effect")—just like the cold-fluid equations—but includes correlation effects via the equilibrium pair distribution function $g(r)$. The "indirect thermal effect" is implicitly included in $g(r)$ and is associated with the coupling dependence of the internal liquid structure [92]. The reason for the success of the QLCA in the strongly coupled liquid phase was argued to be a scaling relation [92]: The importance of correlation effects exceeds that of the direct thermal effect by a factor $\mathcal{O}(\bar{\Gamma})$ (based on free energy calculations for the OCP [102–104]). For the cold-fluid theory, this indicates that the mean-field treatment is a far more severe approximation than the neglect of thermal effects at high $\bar{\Gamma}$.

The accuracy of the cold-fluid theory with respect to the calculation of normal modes for Yukawa Balls will be assessed in Ch. 6.

3.3 Simulation Methods

Computer simulations have become increasingly important and almost indispensable for many-particle physics. Molecular dynamics and Monte Carlo simulations yield numerically exact solutions of the full N-body problem and are usually only limited by the assumptions of the underlying physical model. The results of analytical methods often suffer from severe approximations but typically offer a deeper insight into the physical processes than a simulation. Therefore, the methods complement each other, and a theoretical study greatly benefits from a combined investigation. The basic principles of the simulations methods used in this work are briefly reviewed in this section, see Refs. [18, 91, 105, 106] for more details.

3.3.1 Molecular Dynamics

Introduction

Molecular dynamics (MD) simulations (e.g., Ref. [18, Ch. 10]) solve the equations of motion associated with the Hamiltonian (3.5) and yield the particles' positions $\{\boldsymbol{r}_i\}$ and momenta $\{\boldsymbol{p}_i\}$ as a sequence of snapshots separated by a timestep Δt. This establishes a certain analogy with dusty plasma experiments, where the particle motion is recorded in a similar fashion by video cameras with a particular frame rate.

The trajectories $\{\boldsymbol{r}_i(t)\}$ are the solutions of the $3N$ coupled equations ($i \in \{1,\ldots,N\}$)

$$m\ddot{\boldsymbol{r}}_i = \boldsymbol{F}_i = -\nabla_i U(\boldsymbol{r}_1,\ldots,\boldsymbol{r}_N), \tag{3.14}$$

and describe the phase space evolution of the system at constant total energy E. In terms of Statistical Mechanics, a molecular dynamics simulation thus represents the microcanonical ensemble. The forces $\boldsymbol{F}_i$ are derived from the total potential energy U and include the pairwise interaction and the external confinement, see Eq. (3.5). As the confinement

potential for Yukawa Balls is isotropic, the total angular momentum is another conserved quantity [107].

Since the complete N-particle distribution function is available, the MD method is very versatile and widely used for strongly correlated systems [108]. In this thesis, MD simulations are applied to investigate the excitation spectrum of Yukawa Balls. More details on the simulation procedure are given in Ch. 6.

Verlet Integration

The Verlet integrator [109] has become a popular method for MD simulations since it is very stable and has the ability to conserve the total energy over considerable time intervals. Like Hamilton's equations, it is time-reversible and phase space conserving (symplectic) [18, 91].

The algorithm can be derived from a Taylor expansion for the coordinates or an expansion of the Liouville operator [18, 91]. In the velocity Verlet implementation, the integration is carried out in three steps as

$$\begin{aligned} \boldsymbol{v}\left(t+\frac{\Delta t}{2}\right) &= \boldsymbol{v}(t)+\boldsymbol{a}(t)\frac{\Delta t}{2}, \\ \boldsymbol{r}(t+\Delta t) &= \boldsymbol{r}(t)+\boldsymbol{v}\left(t+\frac{\Delta t}{2}\right)\Delta t, \\ \boldsymbol{v}(t+\Delta t) &= \boldsymbol{v}\left(t+\frac{\Delta t}{2}\right)+\boldsymbol{a}(t+\Delta t)\frac{\Delta t}{2}, \end{aligned} \tag{3.15}$$

where the acceleration is denoted by $\boldsymbol{a}(t)=\boldsymbol{F}(t)/m$. Calculating the $N(N-1)$ interactions is the most expensive part of the algorithm.

3.3.2 Langevin Dynamics

Langevin Equation

In dusty plasma experiments, the dust grains are embedded in a partially ionized plasma where they collide with neutral gas atoms. Instead of treating the dust-neutral collisions explicitly, the Langevin dynamics method uses a stochastic approach to include their effects: A friction term emulates a damping mechanism, and a stochastic force accounts for random heating effects. The neutral gas can be regarded as a large heat bath for the dust particles, see Refs. [18, 36, 110].

The equation of motion for Langevin dynamics then becomes [36]

$$m\ddot{\boldsymbol{r}}_i = -\nabla_i U(\boldsymbol{r}_1,\ldots,\boldsymbol{r}_N) - \nu m\dot{\boldsymbol{r}}_i + \boldsymbol{f}_i(t). \tag{3.16}$$

The random force $\boldsymbol{f}_i(t)$ and the friction term are related by the fluctuation-dissipation theorem

$$\langle f_i^\alpha(t) f_j^\beta(t')\rangle = 2m\nu k_\mathrm{B}T\delta_{ij}\delta_{\alpha\beta}\delta(t-t'), \tag{3.17}$$

where $\alpha, \beta \in \{x, y, z\}$ and $i, j \in \{1, \ldots, N\}$[36]. The neutral gas temperature and the dust-neutral friction coefficient are denoted by T and ν, respectively. Correlations of the random force between different particles and coordinates, and at successive times are assumed negligible. Due to the additional forces, the total energy and angular momentum are no longer conserved. Langevin dynamics corresponds to the canonical ensemble in the sense that the Boltzmann distribution (cf. Sec. 3.3.3) is a time-independent solution of the associated Fokker-Planck equation for the distribution function [110].

Langevin dynamics is routinely used for simulations of dusty plasmas, e.g., Refs. [24, 25]. In highly damped systems inertial terms are of minor importance, and the resulting overdamped *Brownian* motion is widely being studied in the context of colloidal suspensions [42]. In this work, Langevin dynamics simulations are performed to investigate the formation of radial shells in Yukawa Balls (Ch. 4) and to complement the molecular dynamics simulations of the collective modes (Ch. 6) by adding dissipation effects.

Integration Scheme

Two integration methods for the stochastic Langevin equation (3.16) with good performance have been derived by Manella in Ref. [111]. The first is the SLO (symplectic low order) algorithm, which advances the trajectories according to

$$\begin{aligned} \boldsymbol{r}\left(t+\frac{\Delta t}{2}\right) &= \boldsymbol{r}(t) + \boldsymbol{v}(t)\frac{\Delta t}{2}, \\ \boldsymbol{v}(t+\Delta t) &= c_1\left[c_2\boldsymbol{v}(t) + \boldsymbol{a}\left(t+\frac{\Delta t}{2}\right)\Delta t + c_3\boldsymbol{w}\right], \\ \boldsymbol{r}(t+\Delta t) &= \boldsymbol{r}\left(t+\frac{\Delta t}{2}\right) + \boldsymbol{v}(t+\Delta t)\frac{\Delta t}{2}, \end{aligned} \tag{3.18}$$

where the acceleration $\boldsymbol{a}(t)$ only includes the potential forces. While the friction force is implicitly included in the coefficients,

$$c_1 = \frac{1}{1+\nu\Delta t/2}, \qquad c_2 = 1-\frac{\nu\Delta t}{2}, \qquad c_3 = \sqrt{\frac{2k_\mathrm{B}T}{m}\nu\Delta t},$$

the stochastic character of the Langevin equation enters the algorithm via the random variable $\boldsymbol{w}$. Its components are drawn from a normal distribution with unit variance and zero mean, see also Ref. [18].

3.3.3 Metropolis Monte Carlo

Statistical Mechanics

The classical Metropolis Monte Carlo algorithm [112] approaches the N-body problem from the viewpoint of equilibrium Statistical Mechanics. Rather than following the phase space trajectory of an isolated system with constant energy, one considers the phase space distribution of an ensemble of systems that share a common temperature T, volume V,

and particle number N (in the canonical ensemble). The equivalency in the limit of large system sizes is established by the ergodic hypothesis, see Ref. [91].

The ensemble average of a momentum independent quantity $\chi(\boldsymbol{r}^N)$ in the canonical ensemble is calculated with the Boltzmann probability distribution as [91, 105]

$$\langle\chi\rangle(N,T) = \frac{1}{Z(N,T)} \int \chi(\boldsymbol{r}^N) e^{-\beta U(\boldsymbol{r}^N)}\, d\boldsymbol{r}^N, \tag{3.19}$$

where the configuration integral is denoted by $Z(N,T) = \int e^{-\beta U(\boldsymbol{r}^N)} d\boldsymbol{r}^N$, $\beta = 1/(k_\mathrm{B}T)$, and $U(\boldsymbol{r}^N)$ is the total potential energy, see Eq. (3.5). As a particular example, consider the ensemble averaged density profile in an isotropic confinement $V(r)$ [87, 91],

$$\langle n(\boldsymbol{r})\rangle(N,T) = \left\langle \sum_{i=1}^{N} \delta(\boldsymbol{r}-\boldsymbol{r}_i) \right\rangle = \frac{N}{Z(N,T)} \int e^{-\beta U(\boldsymbol{r},\boldsymbol{r}_2,\ldots,\boldsymbol{r}_N)}\, d\boldsymbol{r}_2 \ldots d\boldsymbol{r}_N,$$

which has an additional spatial dependence. In the liquid state, it only depends on $r = |\boldsymbol{r}|$ due to the spherical symmetry of the chosen confinement.

Metropolis Algorithm

In order to solve the high-dimensional integral in Eq. (3.19), the Metropolis algorithm [112] can be used. It creates a sequence of microstates $\{\boldsymbol{r}_p^N\}$ from a Markov chain ($p \in \{1,\ldots,M\}$) that are distributed according to the Boltzmann distribution in the limit of an infinite simulation time ($M \to \infty$), see Refs. [91, 105]. By employing the method of importance sampling, the canonical average (3.19) is transformed into a simple mean of the quantity $\chi(\boldsymbol{r}^N)$ at the sampled phase space points,

$$\langle\chi\rangle(N,T) \approx \frac{1}{M} \sum_{p=1}^{M} \xi(\boldsymbol{r}_p^N) \pm \sigma_\mathrm{MC}, \tag{3.20}$$

where the statistical error $\sigma_\mathrm{MC} \propto 1/\sqrt{M}$ decreases with the simulation length [105].

The success of the Metropolis algorithm in solving the integral (3.19) stems from sampling the particle configurations with the Boltzmann distribution—compared to a straightforward method with uniform sampling probability. This yields a weighted average with a significantly reduced statistical error, where the weighting is implicitly included in the sampling mechanism [105].

The explicit transition probability for a move from $\boldsymbol{r}_p^N$ to $\boldsymbol{r}_{p+1}^N$ in the Metropolis algorithm is given by [105]

$$\pi(\boldsymbol{r}_p^N, \boldsymbol{r}_{p+1}^N) = \begin{cases} e^{-\beta\Delta U}, & \Delta U = U(\boldsymbol{r}_{p+1}^N) - U(\boldsymbol{r}_p^N) > 0, \\ 1, & \Delta U \le 0, \end{cases}$$

and depends on the potential energy difference ΔU and the temperature. It satisfies the detailed balance condition, which ensures that all necessary criteria are met for the convergence toward the Boltzmann distribution. For further details, see Refs. [91, 105].

One of the numerous applications of the Metropolis algorithm was the calculation of the free energy of the one-component plasma in the liquid and solid phase [102–104]. Here, it is used to determine the finite temperature density profiles of confined particles in various isotropic potentials (Ch. 4).

CHAPTER 4

Shell Formation Dynamics

In recent years, the ground states of spherically confined plasmas and their shell structures have been investigated in detail by numerical simulations [46, 69, 73–75] and theoretical methods [76, 77]. In particular, the screening dependence of the ground state properties is well understood by now [36]. On the other hand, the *dynamic* correlation buildup and the associated time-resolved *formation* of the shell structure have received little attention, and interesting questions arise when similar processes are considered in related strongly coupled plasmas.

Simulations by Pohl *et al.* [6] showed that an ultracold neutral plasma can form concentric ion shells that are very similar to those in *trapped* ion experiments [4] if the ions are laser-cooled during the expansion phase. They observed that shells started to emerge in the *inner* region of the plasma. Previous investigations [113, 114] had indicated that it would be difficult to reach the required coupling strength in these systems. A contrary observation regarding the direction of shell formation was made by Totsuji *et al.* [8], whose simulations for confined ions showed shell formation starting at the surface and proceeding toward the core upon increase of the coupling parameter, see also Ref. [115]. Schiffer performed a general investigation on the influence of the trapping potential on the structure of confined ions [116]. The question of how the trapping potential affects the formation of radial shells in confined plasmas, and, particularly, the time-dependent correlation buildup in *dusty plasmas* (Yukawa Balls) have been investigated during the course of this work.

In order to answer these questions, a series of simulations have been performed [117, 118], which will be presented in the following. Langevin dynamics and Monte Carlo simulations are used to emulate the cooling process from a weakly coupled system without shell structure toward the strongly coupled limit. They reveal that both the screening parameter and the confinement potential qualitatively affect the evolution of the density profile and the emergence of the shell structure. While generally starting at the plasma edge, shell formation can be triggered inside the plasma by making the central region inaccessible to the particles.

This chapter is organized as follows.[1] Some details on the Langevin dynamics simulations are given in Sec. 4.1. The correlation buildup and the formation of the shell structure are studied in Sec. 4.2. This is followed by an investigation of different confinement potentials and their influence on the order of shell formation in Sec. 4.3. The findings are summarized in Sec. 4.4.

4.1 Simulation Method

The static equilibrium properties (e.g., the density profile) of the system described by the Hamiltonian (3.5) and the Langevin equation (3.16) are fully determined by the dimensionless coupling parameter $\Gamma = q^2/(a\,k_\mathrm{B}T)$ and the screening parameter κa. Here, T denotes the heat bath temperature, and $a = \sqrt[3]{q^2/m\omega_0^2}$ corresponds to the Wigner-Seitz radius in a Coulomb system ($\kappa = 0$), cf. Ch. 2. The latter follows from the constant mean density profile [76] and the analogy between a homogeneous background and a harmonic confinement [5], see also Ref. [87]. In Yukawa systems, the mean density is not constant, and Γ should rather be interpreted as an inverse dimensionless temperature. For dynamic processes such as the cooling process described next, the dimensionless dust-neutral friction parameter ν/ω_0 must be specified.

The correlation buildup is investigated in the following manner. In order to create a well-defined initial state, the Langevin method is used with a friction coefficient ν_i to equilibrate the system at low coupling ($\Gamma_\mathrm{i} = 0.2$). At these conditions, correlation effects are weak, and the density profile shows no signs of a shell structure. In experiments, this should be possible by using laser radiation pressure to transfer small random amounts of momentum to the dust particles, which was demonstrated by Nosenko *et al.* [119] for 2D dust layers. The Langevin method was also used to model laser cooling in an ultracold neutral plasma [6]. Once the laser is turned off ($t = 0$), the particles will cool down due to friction with the neutral gas until a new equilibrium state is attained at the neutral gas temperature T_n. In the simulations, this amends to changing the heat bath temperature from T_i to T_n, i.e., $\Gamma_\mathrm{i} \to \Gamma_\mathrm{n}$. The cooling rate is then determined by the value of the friction coefficient ν. The final coupling is chosen as $\Gamma_\mathrm{n} = 125$—corresponding to a strongly coupled state with well-defined shells—and should be within experimental feasibility [10]. For each set of parameters, several hundred to a few thousand independent simulation runs are performed. This corresponds to averaging over the time evolution of a canonical distribution of initial states. In an isotropic trap, the ensemble averaged time-dependent density profile, $n(r,t)$, then only depends on the radial coordinate r.

Following the time evolution of the kinetic and potential energy, this scenario makes it possible to study the time-dependent correlation buildup and the formation of radial shells in a confined plasma (identified here by examining the radial density profile). During the cooling process, the system undergoes a transition from a weakly coupled initial state toward a strongly coupled final state and thereby strides through the relevant coupling regimes for shell formation. The feasibility of the cooling scenario for experiments should make a direct comparison between experiment and theory possible.

[1] This chapter is based on a revised version of Ref. [117] with additional results from Ref. [118].

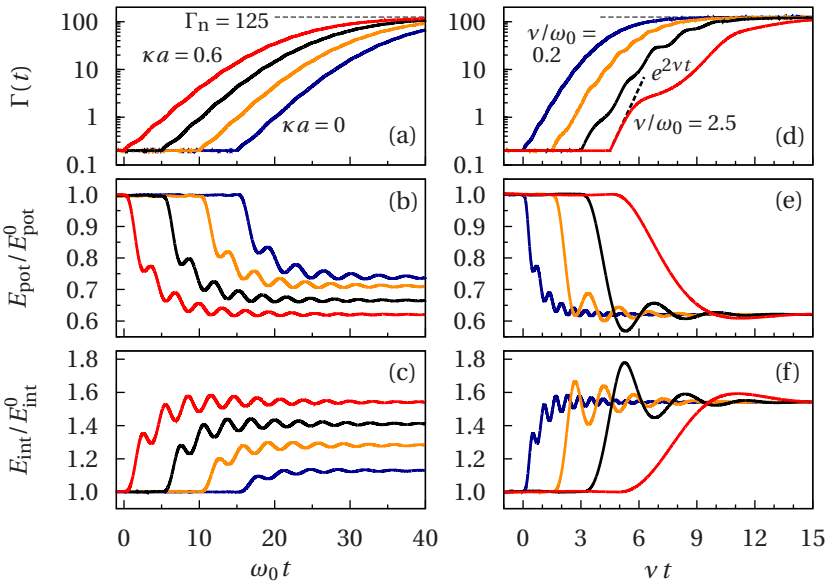

Figure 4.1: Time dependence of the coupling parameter, and the potential and interaction energy for $N = 400$. For the sake of clarity, the graphs for different parameters are shifted by $\omega_0 t = 5$ (left) and $\nu t = 1.5$ (right). (a)-(c) Influence of screening for $\nu/\omega_0 = 0.2$ and $\kappa a = 0.6, 0.4, 0.2, 0$ (from left to right). (d)-(f) Influence of the damping rate for $\kappa a = 0.6$ and $\nu/\omega_0 = 0.2, 0.5, 1, 2.5$. Note the different scaling of the time axes. The potential and interaction energy are normalized to the respective equilibrium energy at $t = 0$ ($\Gamma_i = 0.2$). From Ref. [117]. Copyright (2010) by the American Physical Society.

4.2 Correlation Buildup

4.2.1 Coupling Parameter and Potential Energy

The coupling parameter Γ is the key factor that determines the extent of the shell structure. In a system out of equilibrium, the definition of a well-defined temperature is difficult since it is connected with the existence of a Maxwellian velocity distribution. In the limits $t = 0$ and after a sufficiently long equilibration time after the cooling process, the system has reached an equilibrium state, and this condition is fulfilled. However, in between these two stages, this is not *strictly* valid. Nevertheless, it is possible to define a temperature [i.e., a coupling parameter $\Gamma(t) \propto 1/T(t)$] via $E_{\mathrm{kin}}(t) = 3Nk_{\mathrm{B}}T(t)/2$. Even though the kinetic energy also contains macroscopic (ballistic) motion, this definition should give a reasonable estimate of the coupling strength.

The so-defined coupling parameter and the potential energies are shown in Fig. 4.1. On the one hand, the behavior of the time-dependent coupling parameter $\Gamma(t)$ is only weakly affected by the screening parameter, see Fig. 4.1(a). Starting at $\Gamma(0) = \Gamma_i = 0.2$, it gradually increases to a value within a few percent of Γ_n after a cooling time of roughly $\omega_0 t \approx 35 - 40$ has elapsed. Especially the last phase is characterized by a very slow increase of $\Gamma(t)$. On the other hand, the friction parameter influences the results considerably, cf. Fig. 4.1(d). While at low friction ($\nu/\omega_0 = 0.2$) the increase is very smooth, it is accompanied by small

modulations at intermediate values ($\nu/\omega_0 = 0.5, 1$) and transforms into an almost stepwise behavior at large damping ($\nu/\omega_0 = 2.5$). Here, the initial correlation buildup follows $\Gamma(t) \propto \exp(2\nu t)$, which is the expected behavior for a damped free particle (ballistic regime), cf. Fig. 4.1(d). Note that the typical timescale (in units of ν^{-1}) for reaching Γ_n is significantly longer in the high damping limit, see Fig. 4.1(d) and Ref. [118].

The potential and interaction energy,

$$E_\mathrm{pot} = \frac{m}{2}\omega_0^2 \sum_{i=1}^{N} r_i^2, \qquad E_\mathrm{int} = \frac{1}{2}\sum_{i\neq j}^{N} q^2 \frac{e^{-\kappa|\boldsymbol{r}_{ij}|}}{|\boldsymbol{r}_{ij}|}, \tag{4.1}$$

show a similar time evolution during the cooling process [Figs. 4.1(b),(c),(e) and (f)]. The former is proportional to the mean squared radius of the cluster and hence related to the size of the plasma. As the temperature drops, the cluster contracts, E_pot decreases and performs small amplitude oscillations. On the other hand, the interaction energy *increases*, but it exhibits the same kind of modulations as the potential energy. Due to the reduced plasma size at strong coupling, the mean separation between the particles is being reduced, thus, the coupling strength increases.

The effect of the screening parameter is to enhance the effective loss (gain) of potential (interaction) energy between the initial and the final state. This difference is unaffected by the choice of the friction coefficient since the equilibrium states are independent of ν. However, the time evolution *is* affected by the damping rate, see Figs. 4.1(e) and (f). While the oscillations appear as rather weak modulations at low friction, they clearly lead to an overshooting of E_pot and E_int at intermediate values and diminish at high damping.

4.2.2 Breathing Mode Excitation

Oscillations of the mean squared radius are usually associated with a monopole oscillation of the plasma [13]. At $t = 0$, the particles' kinetic energy is being removed from the system by the friction force, which aims at establishing a new equilibrium at $\Gamma_\mathrm{n} = 125$—in combination with the random force. Depending on the damping coefficient, the temperature drops at a rate $\sim \nu$, which leads to an initial compression of the cluster. In a hypothetical scenario with an infinitesimally low damping rate, the cluster evolves from one equilibrium state to another, because the particles always have sufficient time to adjust to the current coupling parameter. At finite damping, however, this is not possible, and the particles' inertia leads to the excitation of a normal mode after the initial compression. The excitation amplitude is rather weak at $\nu/\omega_0 = 0.2$, since the removal of kinetic energy is performed slowly. After an initial growth of the amplitude for $\nu/\omega_0 = 0.5, 1$, the excitation is rapidly damped out at strong friction, see Figs. 4.1(e) and (f).

The frequency of the oscillations is analyzed in Fig. 4.2(a). A low damping rate of $\nu/\omega_0 = 0.1$ makes it possible to observe several oscillations during the cooling process. A time dependent frequency $\omega^*([t_i + t_{i+1}]/2)$ can be determined from two successive minima or maxima of E_pot at t_i and t_{i+1}. The rapid changes observed in the early phase vanish for $\omega_0 t \gtrsim 30$, and $\omega^*(t)$ approaches a value that can be interpreted as the breathing frequency of the new equilibrium state. The initial oscillations may be attributed to the non-equilibrium behavior of the system.

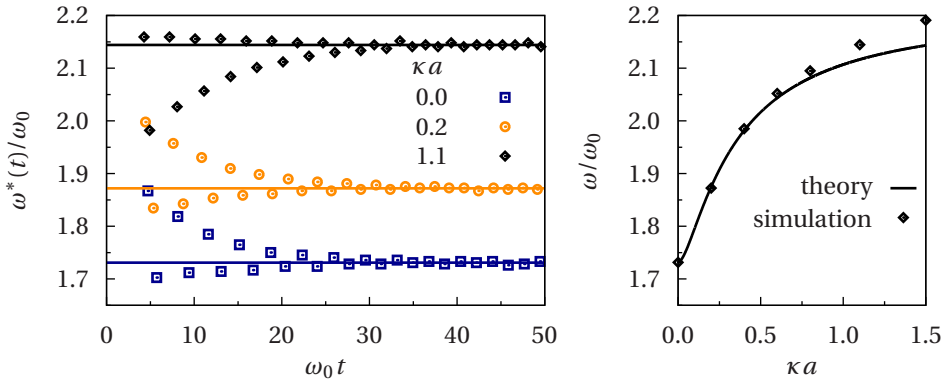

Figure 4.2: Instantaneous oscillation frequency of E_{pot} (cf. Fig. 4.1) for various κa and $\nu/\omega_0 = 0.1$. Horizontal lines denote the mean frequency in the interval $35 \leq \omega_0 t \leq 50$. Right: Mean frequency (corrected for friction, see text) compared to the analytic expression of Refs. [76, 120]. From Ref. [117]. Copyright (2010) by the American Physical Society.

Since the frequency is measured in a damped system, the intrinsic frequency ω of the plasma breathing mode can be extracted from the relation $\omega^* = \sqrt{\omega^2 - \nu^2/4}$, which describes the frequency variation of a harmonic oscillator subject to damping [9]. The continuum limit for the breathing frequency of a uniform sphere [120] is shown in Fig. 4.2(b) for comparison. The plasma radius is computed according to Ref. [76]. In the Coulomb limit, the simulation data agree well with the exact result for a crystallized plasma, $\omega/\omega_0 = \sqrt{3}$ [13, 121]. For $\kappa > 0$, the mean-field theory [120] accurately describes the simulation results at low screening but shows increasing deviations for $\kappa a \gtrsim 0.6$. The good agreement confirms that the observed oscillations correspond to the excitation of a breathing mode. Chapters 5 and 6 continue the discussion of normal modes in Yukawa Balls.

4.2.3 Shell Formation

Density Profile

In the next step, the emergence of the shell structure will be investigated, see Fig. 4.3 for a system with 1200 particles. At $t = 0$, i.e., $\Gamma_{\mathrm{i}} = 0.2$, the density monotonically decreases with the distance from the trap center. In this weakly coupled state, the profile is well described by a mean-field theory [87, 90],

$$n_{\mathrm{MF}}(r, T = T_{\mathrm{i}}) \propto \exp\left\{-\left[V(r) + q\phi(r)\right]/k_{\mathrm{B}}T_{\mathrm{i}}\right\}, \tag{4.2}$$

where $V(r)$ is the harmonic confinement and $\phi(r)$ the effective potential to be calculated self-consistently from Eq. (3.8). Equations (4.2) and (3.8) constitute a closed set of equations for the density at finite temperature but cannot describe the emergence of the shell structure at strong coupling. For this purpose, an improved theory, e.g., the hypernetted-chain approximation, is required [87–90].

As the system cools down, the first indications for the onset of the shell structure are observed after a time $\omega_0 t \approx 10$ at the cluster boundary, where small density maxima are

formed. At this stage, the density profile in the inner region of the plasma is well described by the zero temperature limit of Eq. (4.2) [76],

$$n_{\mathrm{MF}}(r, T=0) = (4\pi q^2)^{-1}\left[(\Delta-\kappa^2)V(r)+\kappa^2\mu(N)\right]\Theta(R-r), \tag{4.3}$$

where $\mu(N)$ is the chemical potential, R the plasma radius, and $\Theta(R-r)$ the Heaviside step function, see the dashed lines in Fig. 4.3. It should be noted that Eq. (4.3) also accurately describes the mean density of a crystallized system at the shell positions [76], at least up to moderate screening.

Upon further increase of $\Gamma(t)$, the inner shells (i.e., density modulations) are formed. For Coulomb interaction, shell formation clearly proceeds from the boundary toward the center with shells emerging at almost constant time intervals, see Fig. 4.3(d). In Yukawa systems, the general trend is the same, but the formation of the inner shells is being accelerated by an increase of the screening parameter: While the effect is still rather weak at $\kappa a = 0.6$, the shells form almost simultaneously at $\kappa a = 2$ [Figs. 4.3(e) and (f)]. The faster shell formation may partially be attributed to an inward force produced by particles on the outer shell [76], contrary to Coulomb systems, where only particles inside a sphere exert a net force. Nevertheless, in all three cases the inner shells are much less defined than the outer ones, where the density almost drops to zero between the maxima, while the central density is only weakly modulated.

Local Screening and Coupling Parameter

The properties of the *uniform* Yukawa OCP are completely specified by the screening parameter $\bar{\kappa} = \kappa a_{\mathrm{ws}}$ and the coupling parameter $\bar{\Gamma} = q^2/(a_{\mathrm{ws}} k_{\mathrm{B}} T)$ [19], see also Sec. 2.1.1. They determine the crystal structure (fcc or bcc) in a frozen system [26] and the effective coupling strength in the liquid state. The latter can be quantified by the height of the first maximum in the pair distribution function $g(r)$ [122, 123]. It compares the probability of finding two particles at a certain distance r with the same probability in an uncorrelated system. Strong correlations manifest themselves as a "correlation hole" around each particle near $r = 0$ and pronounced modulations of $g(r)$ at larger distances. Both effects indicate increased order and strong coupling. In general, an increase of the screening (coupling) parameter decreases (increases) the effective coupling strength [122–124]. Since the inclusion of a realistic pair distribution function (i.e., correlation effects) turns out to be the essential ingredient for the existence of a shell structure in confined systems [87, 88], these effects will be discussed in the following.

The order of shell formation described in the previous section is completely different from the observations in ultracold neutral plasmas [6], where the process starts near the center and proceeds outward. In Ref. [6], this was attributed to the higher density. In these plasmas, the weakly coupled electrons provide an effective background for the laser-cooled ions with an approximately Gaussian density profile [125, 126]. However, the plasma state is not stationary, and the whole system expands.

In the present case, the confinement potential can be regarded as an effective background with an *inhomogeneous* density profile $n_{\mathrm{MF}}(r, T = 0)$. Thus, one may define a local

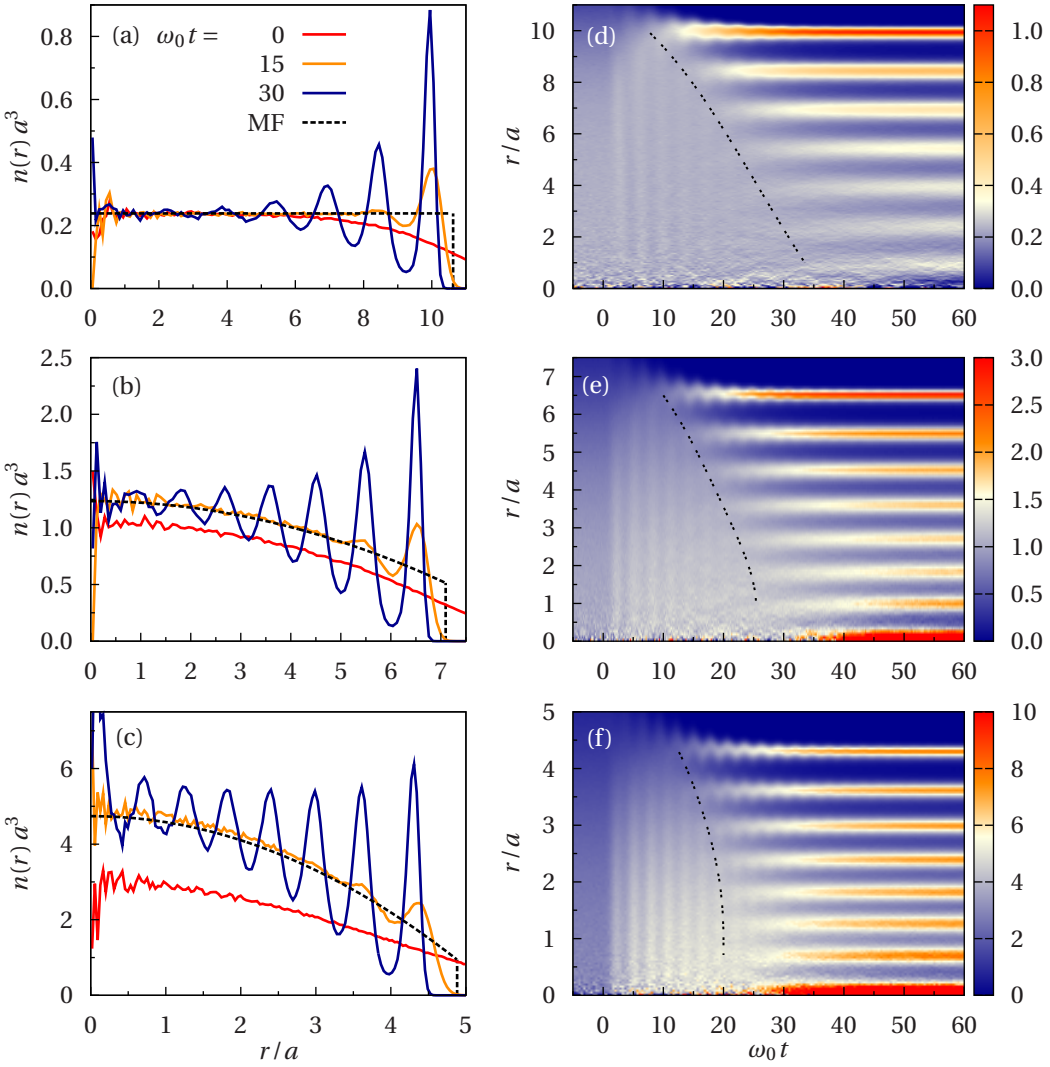

Figure 4.3: (a)-(c) Snapshots of $n(r,t)$ at $\omega_0 t = 0, 15, 30$ (oscillations grow with time) together with the $T = 0$ mean-field (MF) solution of Eq. (4.3). From top to bottom row: $\kappa a = 0, 0.6, 2$. (d)-(f) Evolution of the density profile for $N = 1200$ with $\nu/\omega_0 = 0.2$. The black dashed line connects the approximate times and positions at which the shells emerge. From Ref. [117]. Copyright (2010) by the American Physical Society.

radial coupling parameter

$$\bar{\Gamma}(r) = \frac{q^2/a_{\mathrm{ws}}(r)}{k_{\mathrm{B}}T} \propto n_{\mathrm{MF}}^{1/3}(r, T=0),$$

just like in a system with a *homogeneous* background (OCP). Here, the local Wigner-Seitz radius is denoted by $a_{\mathrm{ws}}(r) = \sqrt[3]{3/4\pi n_{\mathrm{MF}}(r, T=0)}$. For Coulomb interaction, this definition indeed coincides with the coupling parameter $\Gamma = q^2/(a\, k_{\mathrm{B}} T)$, cf. Sec. 4.1 and Eq. (4.3). The observation that the density profile prior to shell formation is well described by the cold mean-field limit (4.3) justifies the use of $n_{\mathrm{MF}}(r, T=0)$.

Based on the local coupling parameter, it now seems natural to assume that shell formation starts at the position with the highest density. For $\kappa > 0$, this is clearly the center of the trap, while the question cannot easily be answered for Coulomb interaction since $n_{\mathrm{MF}}(r, T=0)$ is constant. However, in the simulations, the density at the plasma boundary is lower than the mean-field result suggests, see Fig. 4.3(a), and the local coupling should be weaker than at the center. Thus, one would expect shell formation from the center, which is indeed the correct result for ultracold neutral plasmas but not for the present system. Hence, judging only by the local coupling parameter can lead to contradictory results.

Another mechanism that must be taken into account in screened systems is the effective range of the particle interaction, see also Ref. [127]. As was done for the coupling parameter, one may define a local (dimensionless) screening parameter via

$$\bar{\kappa}(r) = \kappa\, a_{\mathrm{ws}}(r) \propto n_{\mathrm{MF}}^{-1/3}(r, T=0).$$

From the homogeneous system, it is known that the effective coupling decreases when $\bar{\kappa}$ increases and $\bar{\Gamma}$ is kept constant [26, 123]. Since the density drops toward the boundary, the local screening parameter $\bar{\kappa}(r)$ should take its maximum at $r \approx R$. This would further enhance the effect of the reduced local coupling parameter at this point and should favor shell formation from the center. Since the curvature of $n_{\mathrm{MF}}(r, T=0)$ is determined by κ [76] [cf. Eq. (4.3) and Fig. 4.3], this effect should become more pronounced at strong screening.

The analysis shows that the radially decreasing density profile in Yukawa systems favors a more rapid formation of inner shells compared to the Coulomb case—in agreement with the simulations. The confinement model of Totsuji *et al.* [128, 129] uses a screening dependent trapping potential to produce a constant MF density profile for Yukawa interaction. In this sense, it is equivalent to the harmonic trap for $\kappa = 0$ and could be used to study the screening effect in more detail.

Effect of Cooling Speed

In dusty plasma experiments, the dust-neutral friction coefficient can become significant due to the high gas pressure [1, 2]. Since this was also found to have a large impact on the occurrence probability of metastable states [71], its effect on the formation of shells will be considered in the following [118].

It has already been shown in Fig. 4.1 that the friction coefficient determines the time at which the system reaches the neutral gas temperature. Figure 4.4 displays how it affects

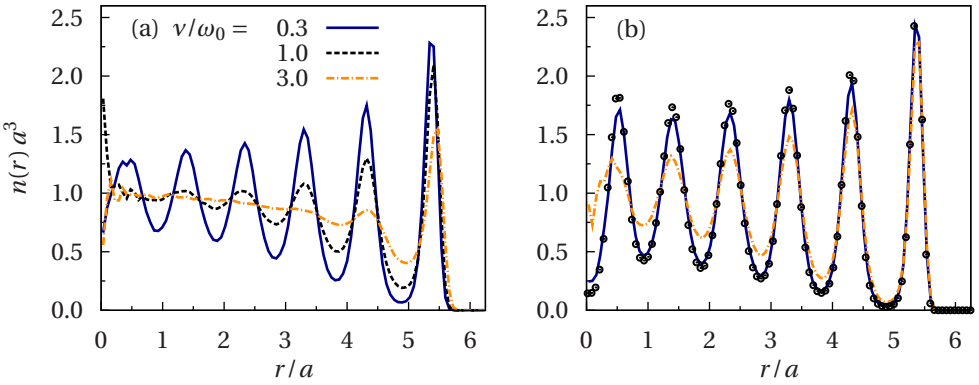

Figure 4.4: Density profiles for $N = 600$ particles shown at a time (a) when $\Gamma(t^*) \approx 120$ and (b) $\omega_0 t = 70$. The points in (b) correspond to equilibrium Monte Carlo results at $\Gamma_n = 125$. After Ref. [118].

the density profile. Consider first Fig. 4.4(a), which shows the density at $t = t^*$, where t^* is defined by $\Gamma(t^*) = 120$—slightly below the neutral gas limit $\Gamma_n = 125$. This coupling strength is reached first for $\nu/\omega_0 = 3$ at $\omega_0 t \approx 6$, closely followed by $\nu/\omega_0 = 1$ at $\omega_0 t \approx 11$, and finally by $\nu/\omega_0 = 0.3$ at $\omega_0 t \approx 30$. Even though the coupling strengths are identical, the density profiles are very different.

In the simulation with the highest friction coefficient ($\nu/\omega_0 = 3$), only the outermost shell has clearly developed, while the inner region of the plasma exhibits almost no modulations. More pronounced structures are observed at lower damping. The discrepancy between the density profiles indicates that the formation of the shell structure cannot follow the fast cooling process, i.e., the spatial profile does not correspond to the equilibrium state defined by $\Gamma = 120$. Rather, the weak modulations of $n(r,t)$ suggest that the spatial correlations correspond to a system at *weaker* coupling. One explanation for the different results is the elapsed cooling time: At low damping, the simulation time is about three times as long as for the high damping case, i.e., the particles had more time to equilibrate and form the shell structure.

However, the results displayed in Fig. 4.4(b) show that this is not the only reason. At a fixed time $\omega_0 t = 70$, both systems have reached the final coupling parameter but the densities still differ substantially. In the high damping case, the particles are readily being slowed down and have no time to adjust their density from the weakly coupled initial to the strongly coupled final state. Instead, the formation of spatial correlations is a slow diffusion-like process at a rather low temperature, where the particles' poor mobility hinders the buildup of the shell structure. On the other hand, if the system is cooled slowly, the particles can partially rearrange during the cooling process when the mobility is still high. Comparisons with a Monte Carlo simulation of the same system at $\Gamma_n = 125$ show that in the latter case equilibration is almost complete, while the density at high damping still deviates considerably from the equilibrium result. At later times, both densities further approach the Monte Carlo profile. Decreasing ν further does not necessarily lead to a faster equilibration. There should exist a lower limit below which the equilibration time is limited

by the rate at which the particles lose kinetic energy. This also influences the initial phase right after cooling has started, but this will not be studied in further detail.

The cooling scenario here is quite similar to the investigation in Ref. [71], where it was shown that rapid damping leads to a higher probability of metastable states and slow cooling favors the ground state. If the choice for the final temperature is $T_\mathrm{n} = 0$, the random force amplitude is zero, and the system can easily be trapped in a metastable state. This is possible because their is no supply of kinetic energy to overcome the potential barriers between the states. However, if $T_\mathrm{n} > 0$, equilibration toward the associated equilibrium state is always possible because the random force serves as a "reservoir" of thermal energy.

While affecting the time for the buildup of the shell structure, the damping rate has no significant influence on the *order* of shell formation. Hence, a sequence of equilibrium Monte Carlo simulations at different coupling strengths should be sufficient to answer this question. This corresponds to an infinitesimally small cooling rate [Sec. 4.3].

Finite System Size

One aspect that has not been taken into account so far is the finite system size. In a strongly coupled *macroscopic* plasma, the pair distribution function depends on $\bar{\kappa}$ and $\bar{\Gamma}$ and can be used to characterize the plasma state [123]. The ensemble averaged density, however, remains *constant* in the liquid state. In the finite system studied here, both the density and the pair distribution function are affected.

For Coulomb systems, the extent to which a finite system displays macroscopic behavior was investigated by Totsuji *et al.* [8]. It was shown that in large Coulomb crystals a bcc lattice may be formed in the core which is covered by a shell structure with a few layers at the boundary. Schiffer [116] argued that due to the finite size, the plasma has to satisfy "boundary conditions" at the surface that dictate the spherical symmetry. This indicates that the surface of the plasma is the key to understanding the formation of the shell structure. While the core is largely isolated from the surface and thus shows properties of a macroscopic system, the shell structure is a consequence of the isotropic confinement and the "vacuum" region around the plasma.

In the cold mean-field approximation for the density, the finite size and the surface are typically associated with a finite density step, and the fraction of particles near the plasma surface is largely determined by $n_\mathrm{MF}(r, T = 0)$. For a monotonically increasing (decreasing) profile, many (few) particles are located near the boundary. In particular, the number of particles in the edge layer is proportional to the height of the density step $n_\mathrm{MF}(R, T = 0)$. Since these are the particles forming the outermost shell, it can be expected that shell formation is more easily achieved in systems with a large density step at the boundary.

4.3 Other Confinement Potentials

Power Law Confinement

In this section, the effect of the confinement potential on the order of shell formation is investigated since it determines the height of the density step at the boundary. The class of

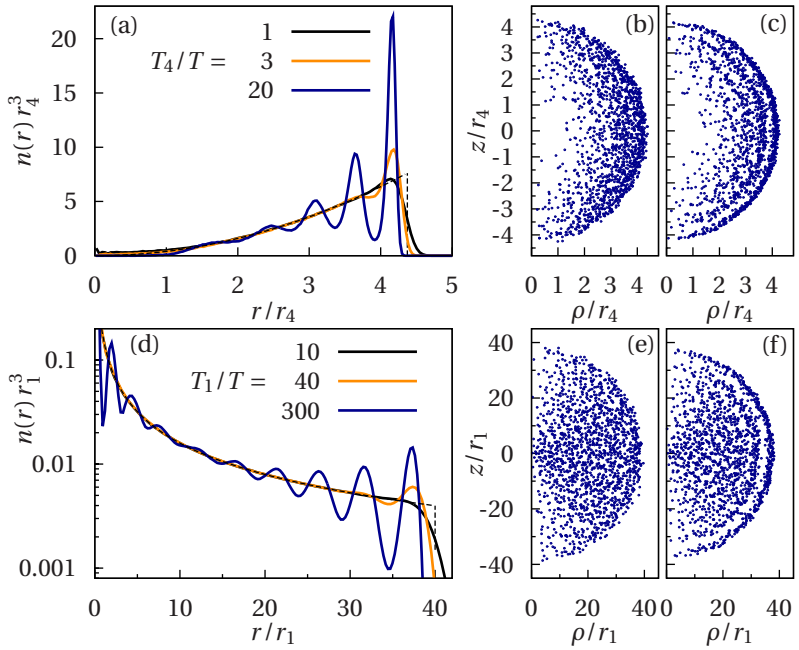

Figure 4.5: Density profiles from MC simulations for $N = 1600$ particles in (a) a quartic and (d) a linear confinement potential. The dashed lines refer to the cold mean-field density profile, Eq. (4.4). The figures on the right-hand side show snapshots (cylindrical coordinates) from the simulation with the respective confinements at (inverse) temperatures (b) $T_4/T = 3$, (c) $T_4/T = 20$, and (e) $T_1/T = 40$, (f) $T_1/T = 300$. The units are $T_{1,4} = q^2/(r_{1,4}k_B)$. After Refs. [117, 118].

isotropic power law confinements, $V_\alpha(r) = c_\alpha r^\alpha/\alpha$, is ideally suited for this purpose. Here, c_α is a numerical factor that determines the confinement strength.

In the Coulomb limit, these potentials create a mean density profile

$$n_{\mathrm{MF}}(r, T=0) = \frac{\alpha+1}{4\pi r_\alpha^{\alpha+1}} r^{\alpha-2}\,\Theta(R_\alpha - r), \tag{4.4}$$

see Eq. (4.3) for $\kappa = 0$. From the normalization condition $\int n_{\mathrm{MF}}(r, T=0)\,d\boldsymbol{r} = N$, the plasma radius R_α is determined as

$$\frac{R_\alpha}{r_\alpha} = \sqrt[\alpha+1]{N}, \qquad\qquad r_\alpha = \sqrt[\alpha+1]{q^2/c_\alpha}.$$

The exponent in Eq. (4.4) shows that the density monotonically decreases (increases) from the center outward for $\alpha < 2$ ($\alpha > 2$). The harmonic confinement with $\alpha = 2$ yields a constant density and has already been studied in the previous section. By choosing α appropriately, the height of the density step can now be manipulated. In the following, a quartic ($\alpha = 4$, large step) and a linear trap ($\alpha = 1$, small step) are studied. In the latter case, the exact form of $V_1(r)$ is slightly changed to $V_1(r) = c_1\sqrt{r_1^2 + r^2}$ to provide a stable position at

$r = 0$, which would not exist without this regularization. The analysis presented here extends previous results by Schiffer [116], who studied various combinations of confinement and interaction forces.

Density profiles in the quartic confinement obtained from MC simulations are displayed in Fig. 4.5(a). By changing the temperature, one can mimic the cooling process of a full Langevin dynamics simulation. As was observed for the harmonic trap, the density at moderate temperatures ($T_4/T = 1$) is well described by the respective cold mean-field result (4.4), except for a smoother decay at the surface. The parabolic density increase toward the plasma boundary is clearly visible. As the temperature is decreased, the first hints for a shell structure are observed slightly below $r = R_4 \approx 4.37\, r_4$ at the surface, while the central region of the trap is almost void of particles, see Figs. 4.5(b) and (c). Lowering the temperature further leads to the formation of radial shells from the boundary toward the center, as expected.

The MC results for the linear trap [Fig. 4.5(d)] show similar agreement with the associated cold mean-field result at $T_1/T = 10$ as the other two confinements for comparable temperatures. Despite the weak density step, shells start to emerge at the boundary. At low temperatures, there are additional density modulations near the center, but they are relatively weak and involve only few particles. The shell structure at the vacuum interface is much more pronounced, see also Ref. [116]. This shows that even if the mean density is manipulated in a way to favor outward shell formation, the general (opposite) trend is hard to reverse.

Harmonic Confinement with Hard Core

The attempt in the previous section to find a suitable confinement that enables shell formation from the core to the boundary has not been successful. Now, the trap will be modified in a different manner. Instead of merely changing the monotony of the mean density profile, the inner region of the plasma will be blocked. Specifically, the harmonic trap is shifted away from the center, and an infinite potential well is added for $r < R_\mathrm{w}$, i.e., the potential reads

$$V_\mathrm{w}(r) = \begin{cases} \infty, & r < R_\mathrm{w}, \\ \frac{m}{2}\omega_0^2 (r - R_\mathrm{w})^2, & r \geq R_\mathrm{w}. \end{cases}$$

Monte Carlo results for Coulomb and Yukawa interaction are shown in Fig. 4.6. Due to the infinite potential well, the inner part of the plasma now becomes a void region. The location of the wall is chosen to ensure that the ratio of the surface areas, $\sim R_\mathrm{o}^2/R_\mathrm{w}^2 \approx 31$, is comparable in both systems. Here, R_o is the (approximate) outer radius at which the density goes to zero.

The main difference between Coulomb and Yukawa interaction in this type of confinement is the density profile near the wall. At strong coupling, the density at $r = R_\mathrm{w}$ vanishes for Coulomb interaction, while the Yukawa system forms a shell of particles attached to the wall. This phenomenon can be understood with the help of Gauss' law. It ensures that only particles *inside* a sphere produce a net force on a particle located at a certain distance from

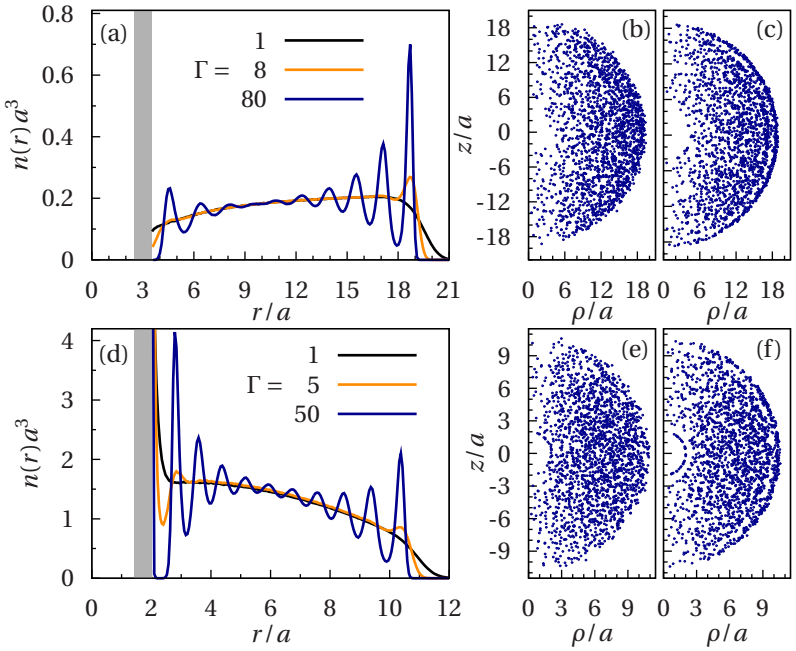

Figure 4.6: Density profiles for $N = 6000$ particles from Monte Carlo simulations for the harmonic confinement with inner hard core for (a) Coulomb ($R_w/a = 3.5$) and (d) Yukawa interaction ($R_w/a = 2$) with $\kappa a = 0.6$. The figures on the right-hand side show snapshots (cylindrical coordinates) from the simulation with the respective interaction at coupling parameters (b) $\Gamma = 8$, (c) $\Gamma = 80$, (e) $\Gamma = 5$, and (f) $\Gamma = 50$. Only a third of the particles are shown. After Ref. [117].

the center. For a particle at the wall, this implies that the force is very weak, since there are no particles for $r < R_w$, and the outer particle distribution is almost isotropic. This principle does not apply to Yukawa interaction [76], and the outer particles do produce an inward force pushing the particles toward the wall—thus the formation of a spherical layer.

The inner void region acts as a second surface just like the one around the plasma. Thus, it creates a set of new spherical boundary conditions the system has to fulfill [116]. This triggers the formation of spherical shells from the center. Inspecting the density profiles more closely, one finds that density modulations are simultaneously formed inside and outside the plasma. However, the trend is clearly more pronounced for Yukawa systems in which the mean density [approximated by the low coupling ($\Gamma = 1$) MC result in Fig. 4.6] decreases toward the outer boundary, whereas an increase is observed for Coulomb interaction. This is similar to the observations made for the harmonic confinement without hard core.

4.4 Summary

In this chapter, the shell formation dynamics in a spherically confined plasma has been investigated by means of Langevin dynamics and Monte Carlo simulations. Upon cooling

a weakly coupled initial state toward the strong coupling limit, the formation of spherical shell structures (pronounced radial density modulations) has been observed. During the cooling process, the confinement energy decreases, while the interaction energy increases. This goes along with the excitation of a plasma breathing mode, whose frequency is well described by a mean-field theory [120] at low screening. In a harmonic confinement, shell formation begins at the plasma boundary and proceeds inward after the initial formation of a density step. Increasing the screening parameter leads to a faster formation of the inner shells compared to the Coulomb limit. This can be explained by the inward force of the outer particles and the radially decreasing mean density profile [76]. In highly damped systems, the fast loss of kinetic energy slows down the buildup of correlations.

The influence of the confinement potential on the shell formation process has been studied by considering a linear and a quartic trap in addition to the harmonic confinement. By comparing equilibrium Monte Carlo density profiles at different coupling parameters, it has been shown that shell formation also proceeds inward. Even though the density in the linear trap displays small maxima near the center, no clear shell structure is observed.

In a shifted harmonic trap with a hard wall that prevents the plasma particles from entering the central region, shell formation can be triggered inside the plasma. In a Coulomb system the trend is relatively weak, but it becomes much more pronounced for Yukawa interacting particles. Here, the inner particles accumulate at the wall due to the inward forces of the outer particles, and shells start to form from the core to the periphery. This can be explained by the existence of a second vacuum region inside the plasma, which imposes a spherical symmetry [116]. However, this does not prevent the simultaneous formation of shells in the opposite direction.

The analysis leads to the conclusion that a possible explanation for the different directions of shell formation in confined plasmas [8] and the expanding ultracold neutral plasma [6] is not only the density profile, but also the absence of a well-defined surface in the latter. There, the Gaussian electron background is associated with a vanishingly small density step, because the electron potential vanishes for $r \to \infty$. Further, it does not confine the ions, and the *expansion* of the plasma hinders the formation of a shell structure in the outer region, which is accompanied by a *contraction* of the plasma in the harmonic confinement. Inner shells then form as a consequence of the increased coupling strength and the spherical symmetry of the plasma cloud.

Related Journal Publications

- H. Kählert and M. Bonitz,
  Time Evolution from Weak to Strong Coupling in a Spherically Confined Dusty Plasma,
  Contrib. Plasma Phys. **51**, 519 (2011)

- H. Kählert and M. Bonitz,
  How Spherical Plasma Crystals Form,
  Phys. Rev. Lett. **104**, 015001 (2010)

CHAPTER 5

Cold-Fluid Theory of Normal Modes

The collective excitations of many-particle systems can be regarded as the "fingerprints" of their intrinsic properties. For experimentalists, a normal mode analysis constitutes a non-invasive diagnostic tool for measuring various plasma parameters [10, 130]. However, a theoretical description is required in order to extract the desired information from the experimental data.

The ground state of spherical Yukawa Balls in the mean-field approximation was derived by Henning *et al.* [76]. In the frame of this thesis, this theory has been extended to time-dependent phenomena by solving the linearized cold-fluid equations [131]. For spheroidal Coulomb plasmas, this analysis was carried out by Dubin [132]. The fluid approach is expected to be reasonably accurate for long-wavelength excitations, which are less sensitive to the discrete particle nature than short-wavelength modes. Despite the approximations involved in the derivation of the equations (cf. Sec. 3.2), comparisons with MD simulations [121] showed indeed that the theory accurately describes the low-order modes in Coulomb plasmas. This was also verified experimentally [133] and recently in Ref. [134]. Thus, the cold-fluid theory is expected to be applicable to Yukawa plasmas as well, cf. Ref. [135] and Ch. 6.

The solution of the fluid equations yields the possible excitation frequencies of the *inhomogeneous* plasma and relates them to a particular spatial mode form [131]—analogous to the dispersion relation in a *homogeneous* plasma. It is shown that the mode spectrum of a harmonically confined Yukawa plasma is qualitatively different from the results in the Coulomb limit [132]. In particular, the analysis yields an explicit result for the deviation of the lowest spherically symmetric eigenmode from a uniform breathing mode, see Ref. [13].

The derivation of the eigenmode spectrum is presented as follows:[1] After the linearization of the fluid equations in Sec. 5.1, the density profile is reviewed, and the total energy in the mean-field approximation is calculated (Sec. 5.2). The normal mode equations are solved and discussed in detail in Sec. 5.3. A brief summary of the results is given in Sec. 5.4.

[1] This chapter is based on a revised and extended version of Ref. [131].

5.1 Linearization of Cold-Fluid Equations

For a spherically confined Yukawa plasma, the fluid equations (3.10) in the cold-fluid limit read [see Eqs. (3.10a) and (3.12)]

$$\frac{\partial n}{\partial t} + \nabla \cdot (n\boldsymbol{u}) = 0, \tag{5.1a}$$

$$m\left[\frac{\partial \boldsymbol{u}}{\partial t} + (\boldsymbol{u}\cdot\nabla)\boldsymbol{u}\right] = -\nabla U - m\nu\boldsymbol{u}, \tag{5.1b}$$

where $U(\boldsymbol{r},t) = V(r) + q\phi(\boldsymbol{r},t)$ denotes the sum of the confinement potential $V(r)$ and the electrostatic (mean-field) potential $\phi(\boldsymbol{r},t)$ created by the density $n(\boldsymbol{r},t)$. In addition to Eq. (3.12), a damping term with friction coefficient ν [cf. the Langevin equation (3.16)] has been added to the momentum equation to account for neutral gas friction in a dusty plasma. The fluid equations are coupled to the screened Poisson equation,

$$(\Delta - \kappa^2)\phi = -4\pi q n, \tag{5.2}$$

for the electrostatic potential ϕ. The combined Eqs. (5.1) and (5.2) yield a self-consistent description of a confined Yukawa plasma in the cold-fluid approximation.

A complete solution of the (non-linear) fluid equations is not necessary. Rather, a commonly used linearization according to the ansatz $n(\boldsymbol{r},t) \simeq n_0(r) + n_1(\boldsymbol{r},t)$, $\boldsymbol{u}(\boldsymbol{r},t) \simeq \boldsymbol{u}_1(\boldsymbol{r},t)$, $\phi(\boldsymbol{r},t) \simeq \phi_0(r) + \phi_1(\boldsymbol{r},t)$ yields the desired information about the ground state and the linear response of the system, see, e.g., Ref. [115]. In this procedure, products of first-order terms are neglected. The drawback is that the approach is restricted to weak excitations and small perturbations from the equilibrium state.

Using the above ansatz in Eqs. (5.1) and (5.2), one obtains the zeroth-order equations

$$q\nabla\phi_0 = -\nabla V, \tag{5.3a}$$

$$\left(\Delta - \kappa^2\right)\phi_0 = -4\pi q n_0, \tag{5.3b}$$

where Eq. (5.3a) is the force balance equation. The ground state density $n_0(r)$ must be determined such that the mean-field potential $\phi_0(r)$—determined by Eq. (5.3b)—compensates the confining force [76].[2] The continuity equation is trivially satisfied to zeroth order and yields no contribution.

Comparing terms of first order leads to

$$\frac{\partial n_1}{\partial t} + \nabla \cdot (n_0\boldsymbol{u}_1) = 0, \tag{5.4a}$$

$$m\frac{\partial \boldsymbol{u}_1}{\partial t} + m\nu\boldsymbol{u}_1 = -q\nabla\phi_1, \tag{5.4b}$$

$$\left(\Delta - \kappa^2\right)\phi_1 = -4\pi q n_1, \tag{5.4c}$$

which determine the linear response of the plasma to a small perturbation of the equilibrium quantities. Equations (5.4) can be simplified further by performing a Fourier decomposition into normal modes according to $\phi_1(\boldsymbol{r},t) = \hat{\phi}_1(\boldsymbol{r},\omega)e^{-i\omega t}$ (and similar expressions

[2] The finite size factor $(N-1)/N$ of Ref. [76] is omitted.

for n_1 and $\boldsymbol{u}_1$). The equations for the Fourier components then read

$$i\omega\hat{n}_1 = \nabla\cdot(n_0\hat{\boldsymbol{u}}_1), \tag{5.5a}$$

$$m(\omega+i\nu)\hat{\boldsymbol{u}}_1 = -iq\nabla\hat{\phi}_1, \tag{5.5b}$$

$$\left(\Delta-\kappa^2\right)\hat{\phi}_1 = -4\pi q\hat{n}_1. \tag{5.5c}$$

After some algebraic manipulations, Eqs. (5.5) can be combined to the following single equation for the perturbed potential (see Refs. [115, 132] for $\kappa = 0$),

$$\nabla\cdot\left[\epsilon(r,\omega)\nabla\hat{\phi}_1\right] = \kappa^2\hat{\phi}_1, \tag{5.6}$$

which involves the dielectric function

$$\epsilon(r,\omega) = 1 - \frac{\omega_\mathrm{p}^2(r)}{\omega(\omega+i\nu)}. \tag{5.7}$$

In contrast to a homogeneous plasma, the plasma frequency for a confined system is not constant in general. Rather, it is a local function of the ground state density,

$$\omega_\mathrm{p}(r) = \sqrt{4\pi q^2 n_0(r)/m}. \tag{5.8}$$

It is evident from Eq. (5.6) that the dielectric function is the important factor that contains the essential information about the linear excitation properties of the plasma.

5.2 Ground State

The problem of finding the ground state density profile for an isotropic harmonic confinement has been solved by Henning *et al.* in Ref. [76]. In this section, these results are reviewed and used to calculate the total energy in the mean-field approximation.

5.2.1 Density Profile

Explicitly, the ground state density is given by the following stepped profile [76],

$$n_0(r) = \frac{3}{4\pi a^3}\left(1+\frac{\xi^2}{6}\frac{3+\xi}{1+\xi}-\frac{\kappa^2 r^2}{6}\right)\Theta(R-r), \tag{5.9}$$

where $\xi = \kappa R$ is the ratio of the plasma radius R and the screening length κ^{-1}. The length unit $a = \sqrt[3]{q^2/m\omega_0^2}$ corresponds to the Wigner-Seitz radius $a_\mathrm{ws} = \sqrt[3]{3/4\pi n_0}$ in the Coulomb limit (constant density) and has already been introduced in Ch. 4. For Yukawa interaction, the density profile exhibits a quadratic decay toward $r = R$ with the highest density at the center of the trap. The plasma radius $R = \xi/\kappa$ follows from [76]

$$\xi^6 + 6\xi^5 + 15\left[\xi^4+\xi^3-k_\mathrm{C}^3(\xi+1)\right] = 0, \tag{5.10}$$

with $k_\mathrm{C} = \kappa R_C$ and $R_C = aN^{1/3}$ being the radius for an unscreened Coulomb system.

Asymptotic expansions for the solution $\xi(k_C)$ of Eq. (5.10) for $k_C \ll 1$ and $k_C \gg 1$ can be found by writing the solution in a power series of k_C and $k_C^{3/5}$, respectively (see Ref. [76] for the first terms in the expansions). Choosing the coefficients such that terms with equal powers of k_C vanish, one finds

$$\xi(k_C) \simeq k_C - \frac{2}{15}k_C^3 + \frac{1}{9}k_C^4 - \frac{1}{25}k_C^5 + \ldots \tag{5.11}$$

in the Coulomb limit ($k_C \ll 1$) and

$$\xi(k_C) \simeq 15^{1/5}\,k_C^{3/5} - 1 + \frac{1}{15^{2/5}}\,k_C^{-6/5} - 15^{1/5}\,\frac{3}{25}\,k_C^{-12/5} + \frac{1}{15}\,k_C^{-3} + \ldots \tag{5.12}$$

for $k_C \gg 1$. This particular limit corresponds to a system where the plasma radius is much larger than the screening length and is encountered when $\kappa a N^{1/3} \gg 1$. A numerical evaluation of Eq. (5.10) shows that the relative error of the approximations (5.11) and (5.12) is less than 10^{-2} for $k_C < 1.26$ and $k_C > 1.26$, respectively.

For a comparison of the cold-fluid theory and the density profile (5.9) with experimental data, it is advantageous to consider the moments of the density,

$$\langle r^n \rangle = \frac{1}{N}\int r^n\, n_0(r)\, d\boldsymbol{r} = \frac{R^n}{N}\left(\frac{R}{a}\right)^3 \frac{\xi^3 + (n+6)\xi^2 + 3(n+5)(1+\xi)}{(n+5)(n+3)(1+\xi)},$$

which are directly accessible in experiments from the particle positions as a simple average. The ratio of two moments [Fig. 5.1(a)] could help determine the unknown parameters ξ and R.

5.2.2 Comparison With Related Systems

It is evident that the limit $\kappa = 0$ (i.e., $\xi = 0$) corresponds to a Coulomb system. Here, Eq. (5.9) reduces to $n_0 = 3/(4\pi a^3)$ inside the plasma. This corresponds to the popular textbook example of a uniformly charged sphere, which has a parabolic electrostatic potential for $r < R$ [82, 107], and often serves as a simple model for confined ions.

In the limit $k_C \gg 1$ (i.e., $\xi \gg 1$), the density (5.9) was shown to closely resemble the profile obtained for the same Yukawa system in a *local* mean-field approximation (LDA) [77],

$$n_0^{\mathrm{LDA}}(r) = \frac{\kappa^2}{4\pi q^2}\,[V(R_{\mathrm{LDA}}) - V(r)]\,\Theta(R_{\mathrm{LDA}} - r), \qquad R_{\mathrm{LDA}} = N^{1/5}\left(\frac{15\,q^2}{m\omega_0^2\kappa^2}\right)^{1/5}, \tag{5.13}$$

where $V(r) = m\omega_0^2 r^2/2$ is the harmonic confinement.[3]

In this approach, the energy density was first calculated for a system with *uniform* density, which was then replaced by the *inhomogeneous* density in the trap [77]. This corresponds to substituting a local delta potential $v_{\mathrm{LDA}}(\boldsymbol{r}) = 4\pi q^2\delta(\boldsymbol{r})/\kappa^2$ for the Yukawa potential $v(r) = q^2 e^{-\kappa r}/r$ in the first place (see Eq. (3) in Ref. [77]). The prefactor of the delta function can be identified as the $\boldsymbol{k} = 0$ component of the Fourier transform of the interaction potential [136]. The associated mean-field interaction term (3.8) to be used in the fluid

[3] Again, the factor $N/(N-1)$ of Ref. [77] has been neglected.

equations, $q\phi_{\mathrm{LDA}}(\boldsymbol{r}) = 4\pi q^2 n(\boldsymbol{r})/\kappa^2$, locally depends on the density. This is equivalent to neglecting the Laplacian in Eq. (5.2) [82] and assumes that potential variations occur on length scales $l \gg \kappa^{-1}$. A reduced integration volume due to the short-range character of the potential explained the good agreement of the two approximations for $k_{\mathrm{C}} \gg 1$ (i.e., $\xi \gg 1$). The important difference between them is the absence of the discontinuity at the plasma radius in the LDA result [77], see also Ref. [82].

The mean-field LDA density profile is mathematically equivalent to the Thomas-Fermi solution for a harmonically trapped Bose-condensed gas with zero kinetic energy [136, 137], which can be written as

$$n_0^{\mathrm{TF}}(r) = \frac{m}{4\pi a_{\mathrm{s}}\hbar^2}\left[V(R_{\mathrm{TF}}) - V(r)\right]\Theta(R_{\mathrm{TF}} - r), \qquad R_{\mathrm{TF}} = N^{1/5}\left(\frac{15\hbar^2 a_{\mathrm{s}}}{m^2\omega_0^2}\right)^{1/5}.$$

In these systems, the interaction can effectively be described by a Dirac delta potential as well, where $v_{\mathrm{B}}(\boldsymbol{r}) = 4\pi\hbar^2 a_{\mathrm{s}}\delta(\boldsymbol{r})/m$ [138]. The density and the interaction potential become identical to the corresponding expressions for Yukawa systems if the s-wave scattering length a_{s} is replaced according to $a_{\mathrm{s}} \to mq^2/(\hbar\kappa)^2$.

Further, the *linearized* equation of motion for the perturbed particle density used by Stringari for the derivation of the normal modes [138] can be obtained in an equivalent form from Eqs. (5.5) within the mean-field LDA, yielding (for zero damping)

$$\omega^2 \hat{n}_1 = -\left(\frac{\omega_0^2}{2}\right)\nabla\cdot\left[\left(R_{\mathrm{LDA}}^2 - r^2\right)\nabla\hat{n}_1\right].$$

Even though the two systems describe very different physical situations, their mathematical equivalence and the close similarity of the LDA density (5.13) with the mean-field result (5.9) for $k_{\mathrm{C}} \gg 1$ will allow for a comparison with the results obtained in the context of confined Bose gases as well—in addition to the obvious Coulomb limit. Analogies of the Yukawa potential with the Coulomb and the Dirac delta potential are also discussed by Olivetti *et al.* [139].

5.2.3 Electrostatic Potential and Ground State Energy

The ground state energy for a confined plasma in the mean-field approximation is given by $E_{\mathrm{tot}} = E_{\mathrm{pot}} + E_{\mathrm{int}}$ [76], where

$$E_{\mathrm{pot}} = \int V(r)n_0(r)d\boldsymbol{r}, \qquad E_{\mathrm{int}} = \frac{q}{2}\int \phi_0(r)n_0(r)d\boldsymbol{r}. \tag{5.14}$$

It contains a contribution from the external confinement (E_{pot}) and the electrostatic interaction energy (E_{int}), cf. Eqs. (4.1).

The evaluation of the interaction energy requires the ground state potential $\phi_0(r)$, which is determined by the screened Poisson equation (5.3b). Since the Yukawa potential is the associated Green's function with the boundary condition $\phi_0(r) \to 0$ for $r \to \infty$ [76, 140], the

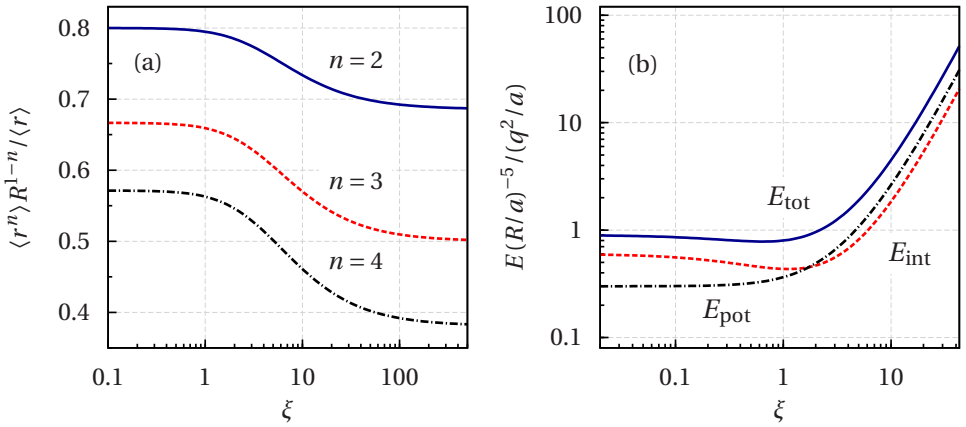

Figure 5.1: Dependence of (a) ratio of nth to first density moment, and (b) ground state energy contributions on the plasma parameter ξ. From Ref. [131]. Copyright (2010) by the American Physical Society.

solution is given by

$$\begin{aligned}\phi_0(r) &= q\int n_0(r')\frac{e^{-\kappa|\boldsymbol{r}-\boldsymbol{r}'|}}{|\boldsymbol{r}-\boldsymbol{r}'|}\,d\boldsymbol{r}' \\ &= \frac{q}{a}\frac{(R/a)^2}{1+\xi}\begin{cases}\frac{1}{2}\left[3+\xi-(1+\xi)\left(\frac{r}{R}\right)^2\right], & r\le R,\\ R\exp(\xi-\kappa r)/r, & r>R.\end{cases}\end{aligned} \tag{5.15}$$

Details on the evaluation of the integral can be found in the Appendix. One can readily check that the potential (5.15) satisfies Eq. (5.3a) and thus ensures local force equilibrium inside the plasma [76]. Outside the plasma, $\phi_0(r) = Q_{\rm eff}\,e^{-\kappa r}/r$ has the form of a Yukawa potential with an effective charge $Q_{\rm eff} = q\,(R/a)^3\,e^{\xi}/(1+\xi)$. In the Coulomb limit, one recovers the result expected from Gauss' law, $Q_{\rm eff} = Nq$.

The potential and interaction energy then follow from Eqs. (5.14) as

$$\begin{aligned}\frac{E_{\rm pot}}{q^2/a} &= \frac{(R/a)^5}{10}\left[3+\frac{\xi^2}{7}\frac{8+\xi}{1+\xi}\right],\\ \frac{E_{\rm int}}{q^2/a} &= \frac{(R/a)^5}{210}\left[\frac{126+147\xi+72\xi^2+18\xi^3+2\xi^4}{(1+\xi)^2}\right].\end{aligned}$$

The *total* energy $E_{\rm tot} = E_{\rm pot} + E_{\rm int}$ is given by

$$\frac{E_{\rm tot}}{q^2/a} = \frac{(R/a)^5}{210}\left[\frac{189+273\xi+159\xi^2+45\xi^3+5\xi^4}{(1+\xi)^2}\right]. \tag{5.16}$$

For Coulomb interaction, the result is $E_{\rm tot}/N = (9/10)\,N^{2/3}q^2/a$ [8, 69], which is recovered from Eq. (5.16) upon taking the limit $\xi = 0$ and $R/a = N^{1/3}$. It corresponds to the mean-field term in the energy expansion of the shell model [80]. In a Yukawa system, $E_{\rm tot}$ is a function of R and ξ, i.e., it depends on N and κa separately, see Fig. 5.1(b).

In the limit $\xi \gg 1$, one finds the asymptotic solution

$$\frac{E_{\mathrm{tot}}}{q^2/a} \simeq \left(\frac{R}{a}\right)^5 \frac{\xi^2}{42} = \frac{1}{(\kappa a)^5}\frac{\xi^7}{42} \simeq \frac{15^{7/5}}{42}\frac{N^{7/5}}{(\kappa a)^{4/5}}, \tag{5.17}$$

where $\xi \simeq 15^{1/5}\, k_{\mathrm{C}}^{3/5}$ has been used in the last step [76], cf. Eq. (5.12). This expression can be compared with the total energy for a trapped Bose gas in the Thomas-Fermi approximation [137].[4] When the replacement of the screening length and the charge is performed as discussed in Sec. 5.2.2, the results are found to be identical.

The asymptotic dependence of the total energy on the particle number changes from $E_{\mathrm{tot}} \propto N^{5/3}$ in a Coulomb system to a weaker growth with $E_{\mathrm{tot}} \propto N^{7/5}$ for Yukawa interaction. Further, Fig. 5.1(b) shows that the main contribution to the total energy is due to the interaction energy in a weakly screened system and due to the potential energy in a system with strong screening. This can be explained by the exponential shielding of the Coulomb potential. The critical point where $E_{\mathrm{pot}} = E_{\mathrm{int}}$ is at $\xi \approx 1.72$.

5.3 Normal Modes

5.3.1 Homogeneous System

Before the normal modes for a finite confined Yukawa plasma are derived, it is instructive to review the associated results for a uniform macroscopic system.

Due to the uniformity of the ground state, the perturbed potential $\hat{\phi}_1(\boldsymbol{r},\omega)$ can be expressed as a superposition of plane waves, i.e., $\hat{\phi}_1(\boldsymbol{r},\omega) \sim e^{i\boldsymbol{k}\cdot\boldsymbol{r}}$. Using this ansatz in Eq. (5.6) in conjunction with a uniform dielectric function, $\epsilon(\omega) = 1-\omega_{\mathrm{p}}^2/\omega^2$, leads to the dispersion relation for the dust acoustic wave (see, e.g., Refs. [96, 97]),

$$\omega(k) = \omega_{\mathrm{p}}\sqrt{\frac{k^2}{k^2+\kappa^2}}.$$

As discussed in Sec. 3.2.3, the wave is acoustic in the long-wavelength limit ($k \ll \kappa$), and its frequency approaches ω_{p} for $k \to \infty$. The latter is the characteristic property of the long-ranged Coulomb system ($\omega \equiv \omega_{\mathrm{p}}$), while the former is found for the short-ranged delta potential ($\omega \equiv c_{\mathrm{s}}k$) [138].[5] The screening length is the length scale that determines the extent to which the Yukawa dispersion relation resembles the two limiting forms.

Modifications of the eigenfunctions and eigenfrequencies for a confined plasma are discussed in the following.

[4] See Eq. (11) in Ref. [137] and the proceeding paragraph. In the notation of Ref. [137], use $\lambda = 1$, $\omega_\perp^0 = \omega_z^0 \equiv \omega_0$, and the replacement $a_{\mathrm{s}} = mq^2/(\hbar\kappa)^2$ for the s-wave scattering length.

[5] The sound speed for the Bose gas is $c_{\mathrm{s}} = (4\pi\hbar^2 a_{\mathrm{s}} n_0/m^2)^{1/2}$ [138] and becomes equivalent to the Yukawa result $c_{\mathrm{s}} = \omega_{\mathrm{p}}/\kappa$ [96] after proper replacement of the s-wave scattering length.

5.3.2 Eigenvalue Problem

General Properties of the Eigenvalue Problem

The spatial form of the eigenmodes is determined by Eq. (5.6) and the ground state density profile $n_0(r)$ entering the dielectric function (5.7). However, this is not sufficient for a complete determination of the normal modes. Additionally, one has to specify physically relevant boundary conditions for $\hat{\phi}_1$. Since the charge distribution is localized in space, the potential must satisfy [132]

$$\lim_{|\boldsymbol{r}|\to\infty} \hat{\phi}_1(\boldsymbol{r},\omega) = 0. \tag{5.18}$$

Boundary conditions on $\hat{\phi}_1$ at the plasma radius, where the density drops to zero, will be discussed in Sec. 5.3.4.

Equation (5.6) and the boundary condition (5.18) are already sufficient to obtain some general results for the range of allowed eigenfrequencies. Following the procedure used by Dubin [141], Eq. (5.6) is multiplied by $\hat{\phi}_1^*$ and subsequently integrated over $\mathbb{R}^3$. It is thereby assumed that $\hat{\phi}_1$ is a valid solution. After a partial integration using Gauss' law and making use of Eq. (5.18), the result can be expressed as

$$\int_{\mathbb{R}^3} \left[\kappa^2 |\hat{\phi}_1|^2 + \epsilon(\boldsymbol{r},\omega)|\nabla\hat{\phi}_1|^2\right] d\boldsymbol{r} = 0. \tag{5.19}$$

Since the first term only yields positive contributions to the integral, there must be a region where $\epsilon(\boldsymbol{r},\omega) < 0$. Considering the cold-fluid form (5.7) of the dielectric function, this yields the allowed range of eigenfrequencies in the absence of damping ($\nu = 0$) as

$$0 < \omega^2 < \max_{\boldsymbol{r}\in\mathbb{R}^3}\left[\omega_\mathrm{p}^2(\boldsymbol{r})\right]. \tag{5.20}$$

Thus, the highest permissible eigenfrequency is determined by the maximum of the plasma frequency.

If friction is included, ω^2 must be replaced by $\omega(\omega + i\nu)$, and the (complex) eigenfrequency $\omega(\nu)$ is obtained from the relation $\omega(\nu)[\omega(\nu) + i\nu] = \omega^2(\nu = 0)$. This is the same relation as for a damped harmonic oscillator [9]. In the following, it is sufficient to consider the frictionless limit.

Dielectric Function for Spherical Confinement

The results obtained so far are quite general and will now be applied to the ground state density given by Eq. (5.9). The explicit result for the dielectric function can be written as a function of $x = \kappa r$ as[6]

$$\epsilon(x,\Omega) = \begin{cases} 1 - \Omega_\mathrm{p}^2(x)/\Omega^2, & x \le \xi, \\ 1, & x > \xi, \end{cases} \tag{5.21}$$

[6] The regions inside and outside the plasma now correspond to $x \le \xi$ and $x > \xi$, respectively.

where $\Omega = \omega/\omega_0$ is the normalized eigenfrequency. These dimensionless variables will be convenient for the calculations. The squared plasma frequency following from the definition of the plasma frequency [Eq. (5.8)] and the ground state density [Eq. (5.9)] is

$$\Omega_\mathrm{p}^2(x) = \frac{\omega_\mathrm{p}^2(r)}{\omega_0^2} = 3 + \frac{\xi^2}{2}\frac{3+\xi}{1+\xi} - \frac{x^2}{2}, \qquad x \le \xi.$$

Since in this particular case the maximum is at the center of the trap, the eigenfrequencies must satisfy $0 < \Omega^2 < \Omega_\mathrm{p}^2(0)$, cf. Eq. (5.20). The remainder of this section will now be devoted to finding the solutions of Eq. (5.6) with the dielectric function (5.21).

5.3.3 Eigenfunctions

Ansatz for Eigenfunctions

Due to the isotropy of the ground state, the perturbed potential can conveniently be expanded in spherical harmonics, i.e.,

$$\hat{\phi}_1(\boldsymbol{r},\omega) \sim f_\ell(r,\omega)\, Y_{\ell m}(\theta,\varphi). \tag{5.22}$$

When this ansatz is used in Eq. (5.6), an equation for the radial function $f_\ell(r,\omega)$ can be obtained by using the fact that the spherical harmonics are eigenfunctions of the angular part of the Laplacian [107, 140],

$$\Delta Y_{\ell m}(\theta,\varphi) = -\frac{\ell(\ell+1)}{r^2} Y_{\ell m}(\theta,\varphi).$$

Using the orthogonality relation of the spherical harmonics [140], one can pick out the expansion coefficient for $Y_{\ell m}$ by multiplying the resulting equation by $Y_{\ell m}^*$ and integrating over the angular coordinates. This leads to the following differential equation for $\tilde{f}_\ell(x,\Omega)$,

$$\frac{\partial}{\partial x}\left[\epsilon(x,\Omega) x^2 \tilde{f}_\ell'(x,\Omega)\right] - \left[x^2 + \ell(\ell+1)\epsilon(x,\Omega)\right]\tilde{f}_\ell(x,\Omega) = 0. \tag{5.23}$$

Here, a change of variables was made from r to a dimensionless form with the radial coordinate $x = \kappa r$, accompanied by $f_\ell(r,\omega) \to \tilde{f}_\ell(x,\Omega)$. Further, the equation was multiplied by x^2.

Equation (5.23) shows that the form of the radial function is independent of m, which justifies the ansatz (5.22). The ground state density—and consequently the dielectric function—both have a discontinuity at $r = R$ (i.e., $x = \xi$). Therefore, Eq. (5.23) must be solved separately inside and outside the plasma, and the two solutions must be matched appropriately at the boundary.

Solution Outside the Plasma

Outside the plasma, the dielectric function is simply $\epsilon \equiv 1$ [cf. Eq. (5.21)], and Eq. (5.23) reduces to the radial function of the screened Poisson equation with zero charge density,

$$x^2 \tilde{f}_\ell''(x) + 2x\tilde{f}_\ell'(x) - \left[x^2 + \ell(\ell+1)\right]\tilde{f}_\ell(x) = 0. \tag{5.24}$$

Its solutions are the *modified spherical Bessel functions* of the first and second kind, $i_\ell(x)$ and $k_\ell(x)$, respectively.[7] They are defined in terms of *modified* Bessel functions as [140]

$$i_\ell(x) = \sqrt{\frac{\pi}{2x}} I_{\ell+1/2}(x), \qquad k_\ell(x) = \sqrt{\frac{2}{\pi x}} K_{\ell+1/2}(x). \tag{5.25}$$

The general solution of Eq. (5.24) is a linear combination of the two. However, the boundary condition (5.18) rules out $i_\ell(\kappa r)$ as a valid solution since it is divergent in the limit $r \to \infty$ [140]. On the other hand, $k_\ell(\kappa r) \to 0$, and so the general solution outside the plasma is

$$f_\ell^{\text{out}}(r) = k_\ell(\kappa r). \tag{5.26}$$

For Coulomb systems, the radial function is given by the familiar solution of Laplace's equation in spherical coordinates, $f_\ell^{\text{out}}(r) \sim r^{-(\ell+1)}$ [107, 115].

Solution Inside the Plasma

Inside the plasma, the differential equation (5.23) is more complicated as one has to deal with the inhomogeneity of the dielectric function (5.21). In order to find a solution, the radial function is written—in a first step—as $\tilde{f}_\ell(x,\Omega) = x^\ell g_\ell(x,\Omega)$. Insertion of the ansatz in Eq. (5.23) yields

$$x\frac{\partial}{\partial x}\left[\epsilon(x,\Omega) g_\ell'(x,\Omega)\right] + 2(\ell+1)\epsilon(x,\Omega) g_\ell'(x,\Omega) - \left[x - \ell\epsilon'(x,\Omega)\right] g_\ell(x,\Omega) = 0. \tag{5.27}$$

Further progress can be made by another change of variables from x to $z = x^2/x_s^2$, where $x_s^2 = 2[\Omega_{\text{p}}^2(0) - \Omega^2]$. The notation for $g_\ell(x,\Omega)$ is thereby changed to $\tilde{g}_\ell(z,\Omega)$. Employing Eq. (5.21) and performing the algebra, one arrives at the hypergeometric differential equation[8]

$$z(1-z)\tilde{g}_\ell''(z,\Omega) + [\ell + 3/2 - (\ell+5/2)z]\,\tilde{g}_\ell'(z,\Omega) - \frac{\ell - \Omega^2}{2}\tilde{g}_\ell(z,\Omega) = 0, \tag{5.28}$$

where the prime indicates differentiation with respect to z.

The general solution of Eq. (5.28) around $z = 0$ (i.e., the trap center $r = 0$) is

$$\tilde{g}_\ell(z,\Omega) = A\,{}_2F_1\left(\frac{\alpha_\ell - \delta_\ell}{2}, \frac{\alpha_\ell + \delta_\ell}{2}; \alpha_\ell; z\right) + B z^{1-\alpha_\ell}\,{}_2F_1\left(\frac{\beta_\ell - \delta_\ell}{2}, \frac{\beta_\ell + \delta_\ell}{2}; \beta_\ell; z\right), \tag{5.29}$$

with arbitrary constants A and B. The various parameters of the hypergeometric function ${}_2F_1$ can be determined by comparison of Eq. (5.28) with the general form of the hypergeometric differential equation. This results in

$$\alpha_\ell = \ell + \frac{3}{2}, \qquad \beta_\ell = \frac{1}{2} - \ell, \qquad \delta_\ell = \sqrt{\ell(\ell+1) + \frac{9}{4} + 2\Omega^2}. \tag{5.30}$$

[7] Many properties of the modified (spherical) Bessel functions can be found in Refs. [140, 142] and the corresponding articles of Refs. [143, 144]

[8] For the hypergeometric differential equation and its solutions see, e.g., Refs. [140, 143, 144]. It is commonly written in the form $z(1-z)g''(z) + [c - (a+b+1)z]g'(z) - ab\,g(z) = 0$ with constant coefficients a, b, c.

When Eq. (5.29) is combined with the ansatz $\tilde{f}_\ell(x,\Omega) = x^\ell g_\ell(x,\Omega)$, one obtains the possible solutions for the radial eigenfunction in the form

$$\tilde{f}_\ell^{(1)}(x,\Omega) \sim x^\ell \, {}_2F_1\left(\frac{\alpha_\ell - \delta_\ell}{2}, \frac{\alpha_\ell + \delta_\ell}{2}; \alpha_\ell; \frac{x^2}{x_s^2}\right),$$
$$\tilde{f}_\ell^{(2)}(x,\Omega) \sim x^{-(\ell+1)} \, {}_2F_1\left(\frac{\beta_\ell - \delta_\ell}{2}, \frac{\beta_\ell + \delta_\ell}{2}; \beta_\ell; \frac{x^2}{x_s^2}\right).$$

The second solution, $\tilde{f}_\ell^{(2)}(x,\Omega)$, diverges at the origin and must therefore be disregarded for physical reasons. Finally, the solution inside the plasma is obtained as

$$f_\ell^{\mathrm{in}}(r,\omega) = r^\ell \, {}_2F_1\left(\frac{\alpha_\ell - \delta_\ell}{2}, \frac{\alpha_\ell + \delta_\ell}{2}; \alpha_\ell; \frac{\kappa^2 r^2}{x_s^2}\right). \tag{5.31}$$

Again, this can be compared with the results in the Coulomb limit [115]. Here, the dielectric function inside the plasma is constant, and the solutions are those of Laplace's equation, namely $f_\ell^{\mathrm{in}}(r) \sim r^\ell$.[9] They simply constitute the first factor in Eq. (5.31). The hypergeometric function accounts for the modifications of the solution compared to the Coulomb limit and incorporates the combined effect of screening and the inhomogeneous density profile.

5.3.4 Eigenfrequencies

Before the eigenfrequencies of the system are determined, it is necessary to comment on the properties of the hypergeometric function. The associated differential equation (5.28) has three regular singular points at $z = 0, 1, \infty$ [140]. The case $z = 1$ corresponds to $x^2 = x_s^2(\Omega) = 2[\Omega_{\mathrm{p}}^2(0) - \Omega^2]$ and is directly related to a root of the dielectric function, $\epsilon(x_s,\Omega) = 0$. At these points x_s, the eigenfrequency Ω equals the local plasma frequency, $\Omega = \Omega_{\mathrm{p}}(x_s)$, see Ref. [141]. The solutions of the hypergeometric differential equation can be singular at these points and must therefore be handled with care.

The series representation of the hypergeometric function is (e.g., Refs. [140, 143])

$$\begin{aligned} {}_2F_1(a,b;c;z) &= \sum_{k=0}^{\infty} \frac{(a)_k (b)_k}{(c)_k} \frac{z^k}{k!} \\ &= 1 + \frac{ab}{c}\frac{z}{1!} + \frac{a(a+1)\,b(b+1)}{c(c+1)}\frac{z^2}{2!} + \ldots, \end{aligned} \tag{5.32}$$

where $(a)_k = \Gamma(a+k)/\Gamma(a)$ denotes the Pochhammer symbol. It is convergent for $|z| < 1$ provided c is not a negative integer. In the following, only those frequencies of the spectrum are considered that satisfy

$$\Omega^2 < \Omega_{\mathrm{p}}^2(\xi) = 3 + \frac{\xi^2}{1+\xi}. \tag{5.33}$$

[9] There is another class of solutions that will be discussed in Sec. 5.3.5, see Refs. [115, 121]

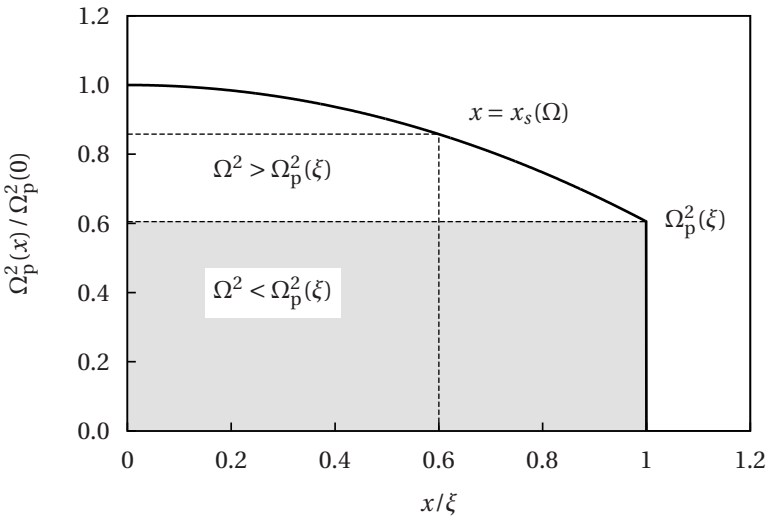

Figure 5.2: Sketch of the plasma frequency profile. The shaded region indicates the considered frequency range $\Omega^2 < \Omega_p^2(\xi)$ in which local resonances are not possible.

This guarantees that $|z| < 1$ for all x inside the plasma. For a Coulomb system, this corresponds to the interval in which the spectrum is discrete, while the range $\Omega^2 > \Omega_p^2(\xi)$ would be associated with a continuous spectrum [145] and the possible existence of hidden (damped) quasi-modes, see Ref. [141]. The problem is illustrated in Fig. 5.2.

Boundary Conditions

As has been mentioned before, the eigenfrequencies are determined from the boundary conditions at the plasma radius. They can be derived from two integrations of Eq. (5.23) [more generally, Eq. (5.6)] across the plasma surface, see Refs. [132, 141].

In the present case, the first integration yields

$$x^2\epsilon(x,\Omega)\tilde{f}_\ell'(x,\Omega) - x_{\rm in}^2\epsilon(x_{\rm in},\Omega)\tilde{f}_\ell'(x_{\rm in},\Omega) = \int_{x_{\rm in}}^{x}\left[(x')^2 + \ell(\ell+1)\epsilon(x',\Omega)\right]\tilde{f}_\ell(x',\Omega)\,dx', \quad (5.34)$$

where $x_{\rm in}$ and x are radial coordinates inside and outside the plasma, respectively. Taking the limits $x_{\rm in} \to \xi^-$ and $x \to \xi^+$, one finds the first boundary condition

$$\epsilon(x,\Omega)\frac{\partial\tilde{f}_\ell^{\rm in}(x,\Omega)}{\partial x}\bigg|_{x=\xi} = \frac{\partial\tilde{f}_\ell^{\rm out}(x,\Omega)}{\partial x}\bigg|_{x=\xi}. \quad (5.35)$$

The integral on the right-hand side of Eq. (5.34) vanishes since $\tilde{f}_\ell(x,\Omega)$ is a well-behaved function for $\Omega < \Omega_p(\xi)$.

Dividing Eq. (5.34) by $x^2\epsilon(x,\Omega)$ and integrating a second time (from $x = \tilde{x}_{\rm in}$ to $x = x_{\rm out}$)

leads to

$$\tilde{f}_\ell(x_{\rm out},\Omega) - \tilde{f}_\ell(\tilde{x}_{\rm in},\Omega) = \int_{\tilde{x}_{\rm in}}^{x_{\rm out}} \frac{dx}{x^2\epsilon(x,\Omega)} \times \left\{ x_{\rm in}^2 \epsilon(x_{\rm in},\Omega)\tilde{f}'_\ell(x_{\rm in},\Omega) + \int_{x_{\rm in}}^{x} \left[(x')^2 + \ell(\ell+1)\epsilon(x',\Omega)\right] \tilde{f}_\ell(x',\Omega)dx' \right\}.$$

Again, the integrand in this equation is well-behaved for $\Omega < \Omega_{\rm p}(\xi)$, and the right-hand side goes to zero upon taking the limits $\tilde{x}_{\rm in} \to \xi^-$ and $x_{\rm out} \to \xi^+$. This gives the second boundary condition

$$\tilde{f}_\ell^{\rm in}(x,\Omega)\big|_{x=\xi} = \tilde{f}_\ell^{\rm out}(x,\Omega)\big|_{x=\xi}. \tag{5.36}$$

Equations (5.35) and (5.36) express the continuity of the radial component of $\epsilon\nabla\hat{\phi}_1$ and the tangential components of $\nabla\hat{\phi}_1$, respectively.[10] They are analogous to those between two dielectric media [146].

Eigenvalue Equation

The general solutions for the radial functions inside and outside the plasma are of the form $af_\ell^{\rm in}(r,\omega)$ and $bf_\ell^{\rm out}(r)$, respectively [see Eqs. (5.26) and (5.31)]. The boundary conditions (5.35) and (5.36) then constitute a set of linear equations for the unknown coefficients a and b. A non-trivial solution requires the vanishing of the determinant, which yields the eigenvalue equation in the form

$$\mathscr{D}(\Omega,\xi) = \left[\ell\epsilon(\xi,\Omega) - \xi\frac{k'_\ell(\xi)}{k_\ell(\xi)}\right] {}_2F_1\left(\frac{\alpha_\ell-\delta_\ell}{2}, \frac{\alpha_\ell+\delta_\ell}{2}; \alpha_\ell; \frac{\xi^2}{x_s^2}\right) + \epsilon(\xi,\Omega)\frac{(\ell-\Omega^2)}{\alpha_\ell}\frac{\xi^2}{x_s^2} {}_2F_1\left(\frac{\alpha_\ell-\delta_\ell}{2}+1, \frac{\alpha_\ell+\delta_\ell}{2}+1; \alpha_\ell+1; \frac{\xi^2}{x_s^2}\right) = 0. \tag{5.37}$$

In general, Eq. (5.37) must be solved numerically, but it is possible to obtain analytic results in both the Coulomb limit ($\xi \to 0$) and the macroscopic limit ($\xi \to \infty$). Note that the solutions $\Omega(\xi)$ only depend on ξ and not on κa and N separately. The mathematical details for the derivation of the analytic limits are presented in the Appendix.

Coulomb Limit

In the limit $\xi \to 0$, the density profile (5.9) becomes homogeneous inside the plasma. Thus, the possible eigenmodes are those of a uniformly charged sphere for which two classes of solutions are known to exist: *surface* modes and *bulk* modes, see Refs. [115, 121]. The eigenfrequencies of the surface modes are given by $\Omega_\ell^2 = 3\ell/(2\ell+1)$. Leading-order corrections for Yukawa interaction with finite ξ are determined as

$$\Omega_\ell^2(\xi) \simeq \frac{3\ell}{2\ell+1} + \left(\frac{4\ell^3+6\ell^2-10\ell}{8\ell^3+12\ell^2-2\ell-3}\right)\xi^2 + \ldots, \qquad \xi \ll 1, \tag{5.38}$$

[10] For the spherical system considered here with $\hat{\phi}_1(\boldsymbol{r},\omega) \sim f_\ell(r,\omega)Y_{\ell m}(\theta,\varphi)$, the radial component of $\nabla\hat{\phi}_1$ only requires the derivative of $f_\ell(r,\omega)$ and the tangential components only those of $Y_{\ell m}(\theta,\varphi)$.

see the Appendix. Except for the center-of-mass mode ($\ell = 1$), which is independent of the particle interaction [147], all mode frequencies increase with the screening parameter.

The bulk modes in the Coulomb system are degenerate and oscillate at the plasma frequency, $\Omega_\mathrm{p}^2 = 3$ [115, 121]. For $\xi > 0$, the degeneracy is found to be lifted, and the mode frequencies depend on the angular mode number $\ell = 0, 1, 2$. Explicitly, one finds

$$\Omega_\ell^2(\xi) \simeq 3 + c_\ell \xi^2 + \ldots, \qquad \xi \ll 1, \tag{5.39}$$

with the coefficients $c_0 \approx 0.85031$, $c_1 \approx 0.98624$, and $c_2 \approx 0.99992$. The increasing value of the expansion coefficients shows that the eigenfrequencies approach the surface plasma frequency $\Omega_\mathrm{p}^2(\xi) \approx 3 + \xi^2 + \ldots$ upon increase of ℓ. The behavior of the eigenvalues in the vicinity of $\Omega_\mathrm{p}(\xi)$ will be discussed after the limit $\xi \to \infty$.

Macroscopic/Strong Screening Limit

It has already been pointed out that the convergence of the hypergeometric function (5.32) is not generally guaranteed at $z = 1$. However, there are certain cases for which its series representation reduces to a polynomial and thus converges regardless of the value of z. These cases are encountered when a or b is a negative integer, see Eq. (5.32). This fact can be used to find the solutions in the limit $\xi \to \infty$.

Employing the relation $\Omega^2 < \Omega_\mathrm{p}^2(\xi)$, it can be shown that $\xi^2/x_\mathrm{s}^2 \to 1$ for $\xi \to \infty$ in the eigenvalue equation (5.37). The choice $a = (\alpha_\ell - \delta_\ell)/2 = -n$ ($n \in \mathbb{N}$) reduces the hypergeometric function to a polynomial. Solving the previous relation for Ω^2 yields the solutions

$$\lim_{\xi\to\infty} \Omega_{n\ell}^2(\xi) \equiv \Omega_{n\ell,\infty}^2 = 2n^2 + (2\ell + 3)n + \ell. \tag{5.40}$$

A more detailed analysis (see the Appendix) shows that for finite ξ the lowest-order correction is given by

$$\Omega_{n\ell}^2(\xi) \simeq \Omega_{n\ell,\infty}^2 - \frac{d_{n\ell}}{\xi^2} + \ldots, \qquad \xi \gg 1, \tag{5.41}$$

where the expansion coefficients $d_{n\ell}$ read

$$\begin{aligned} d_{n\ell} = (2n + \ell + 3/2)[&(4n^3 + 12n^2 + 3n - 9)n \\ &+ 2\ell(4n^3 + 8n^2 + 2\ell n(n+1) + \ell - 1)]. \end{aligned} \tag{5.42}$$

Compared to the Coulomb limit, the solutions are now determined by an additional mode number n.

As was done for the ground state energy, this result can be compared with the corresponding expression for a trapped (Bose) gas with delta interaction. In these systems, the eigenfrequencies were derived by Stringari [138] and are found to be in full agreement with Eq. (5.40). For $(n, \ell) = (1, 0)$, the result of Sheridan [120] for the breathing mode is recovered, see also the discussion in the next section. Considering the different forms of the density profile (parabolic decay *without* step at $r = R$ for the Bose gas [137, 138], the homogeneous sphere *with* step considered by Sheridan [120], and the "mixed" profile (5.9) [76]), it is surprising that all three results coincide.

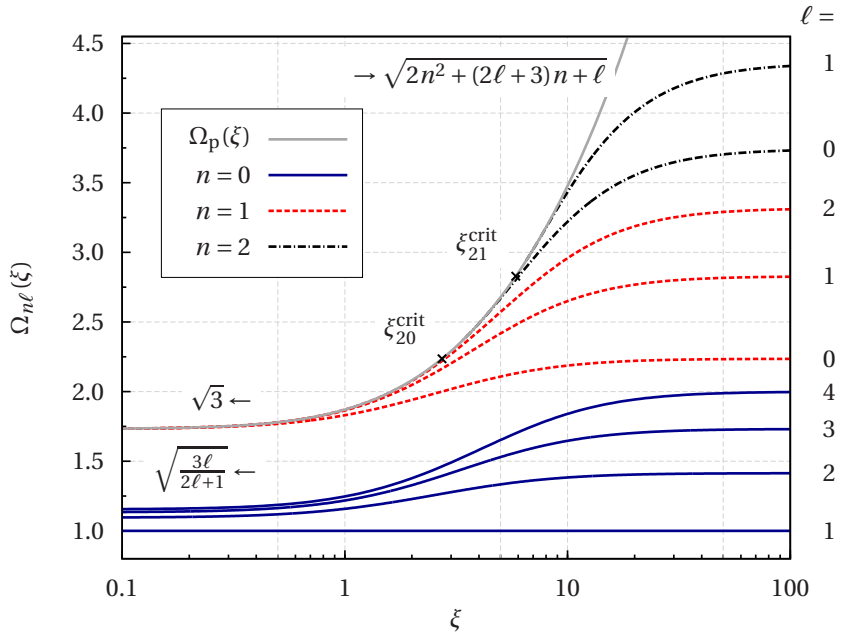

Figure 5.3: Eigenfrequencies and their dependence on ξ for various modes (n,ℓ) as indicated in the figure. The arrows show the analytic limits for $\xi = 0$ and $\xi \to \infty$. The crosses denote the parameters at which new modes appear to the right of $\xi_{n\ell}^{\mathrm{crit}}$. From Ref. [131]. Copyright (2010) by the American Physical Society.

Eigenfrequencies for Arbitrary ξ

A numerical solution of the eigenvalue equation (5.37) yields the mode spectrum shown in Fig. 5.3. The limits found in the previous section are recovered for $\xi \to 0$ and $\xi \to \infty$. Further, the numerical solution allows one to find the relation between the Coulomb modes and the modes with the new mode number n in the opposite limit.

Following the eigenmodes with $n = 0$ from $\xi = \infty$ to $\xi = 0$, it is found that they connect to the Coulomb *surface* modes in a continuous way. The same behavior is observed for $n = 1$ with $\ell = 0, 1, 2$. These modes approach the frequency of the *bulk* modes in the Coulomb system. In all other cases, the frequency approaches $\Omega_p(\xi)$ as ξ decreases, but the corresponding root in Eq. (5.37) vanishes at some critical point $\xi_{n\ell}^{\mathrm{crit}}$, i.e., these modes exist only for $\xi > \xi_{n\ell}^{\mathrm{crit}}$. This is associated with the behavior of the hypergeometric function in the vicinity of $\Omega_p(\xi)$, see the Appendix.

Similar to the determination of the eigenfrequencies in the limit $\xi \to \infty$, the critical points $\xi_{n\ell}^{\mathrm{crit}}$ can be found from the condition $a = (\alpha_\ell - \delta_\ell)/2 = -(n+1)$.[11] However, instead of solving for Ω^2, one uses $\Omega^2 = \Omega_p^2(\xi) = 3 + \xi^2/(1+\xi)$ and solves for ξ. The solutions correspond to the values of the plasma frequency at the boundary, where the hypergeometric series terminates at a finite order. From the numerical evaluation of Eq. (5.37) and the analysis presented in the Appendix, they are identified as the critical points for the

[11] The particular choice of $-(n+1)$ for the negative integer ensures that the modes are labeled consistently.

emergence of new modes in the eigenvalue equation.

Explicitly, they are given by

$$\xi_{n\ell}^{\mathrm{crit}} = \frac{1}{2}\left[\zeta_{n\ell} + \sqrt{\zeta_{n\ell}(\zeta_{n\ell}+4)}\right], \tag{5.43}$$
$$\zeta_{n\ell} = (2n-1)(n+\ell) - 4,$$

where $\ell \geq 3$ for $n = 1$. The corresponding plasma frequency is

$$\Omega_{n\ell}^2(\xi_{n\ell}^{\mathrm{crit}}) = (2n+1)(n-1) + (2n-1)\ell. \tag{5.44}$$

The mode spectrum can then be summarized as follows: The eigenfrequencies are determined by the mode numbers (n,ℓ) and the plasma parameter ξ. For $n = 0$ with arbitrary ℓ and $n = 1$ with $\ell = 0,1,2$, the modes exist for all values of ξ, while the remaining modes exist only for $\xi > \xi_{n\ell}^{\mathrm{crit}}$. A special case occurs for $(n,\ell) = (1,3)$ with $\xi_{13}^{\mathrm{crit}} = 0$. The main difference compared to a Coulomb system is the appearance of the new mode number n and the degeneracy lifting of the bulk modes.

5.3.5 Explicit Results for the Eigenmodes

The eigenmodes inside the plasma explicitly depend on the eigenfrequency Ω [Eq. (5.31)]. With the results from the previous section, it is now possible to further study the form of the eigenfunctions.

Coulomb Limit

The eigenfunctions for the oscillations of a uniformly charged sphere are well-known and will be briefly reviewed here [115, 121]. As can be seen from Eq. (5.6) with a constant dielectric function inside the plasma, the problem reduces to

$$\epsilon(\omega)\Delta\hat{\phi}_1^{\mathrm{in}}(\boldsymbol{r},\omega) = 0, \qquad \Delta\hat{\phi}_1^{\mathrm{out}}(\boldsymbol{r}) = 0. \tag{5.45}$$

While $\hat{\phi}_1^{\mathrm{out}}$ must always satisfy Laplace's equation, two possibilities exist to fulfill the equation for $\hat{\phi}_1^{\mathrm{in}}$. The surface modes are the solutions of Laplace's equation, $\Delta\hat{\phi}_1^{\mathrm{in}}(\boldsymbol{r},\omega) = 0$, whereas the bulk modes are characterized by $\epsilon(\omega) = 0$, i.e., $\omega = \omega_{\mathrm{p}}$ [115].

In the former case, the explicit results are $f_\ell^{\mathrm{in}}(r) \sim r^\ell$ and $f_\ell^{\mathrm{out}}(r) \sim r^{-(\ell+1)}$, while in the latter, the form of the eigenfunctions inside the plasma remains undetermined. This is why the bulk modes are highly degenerate. It can be shown from the boundary conditions that in this case $\hat{\phi}_1^{\mathrm{out}} = 0$ [115]. The continuity of the radial eigenfunction across the plasma boundary then implies $f^{\mathrm{in}}(R) = 0$.

Eigenmodes for Yukawa Interaction

The different solutions of the eigenvalue equation are labeled by the mode number n. Since the eigenfrequency directly determines the form of the radial eigenfunction according to Eq. (5.31), n can be regarded as the radial mode number—analogous to the angular

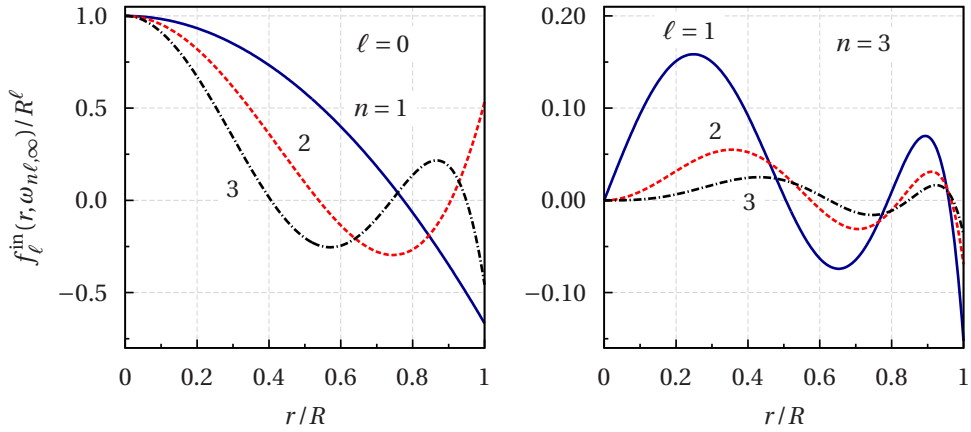

Figure 5.4: Radial eigenfunctions in the limit $\xi \to \infty$ for various modes as indicated in the figure. From Ref. [131]. Copyright (2010) by the American Physical Society.

mode numbers ℓ and m. The radial eigenfunctions then follow from the various solutions of Eq. (5.37) together with Eq. (5.31).

Instead of starting with the limit $\xi \ll 1$, it is advantageous to begin the discussion of the eigenmodes with the case $\xi \to \infty$. It has been pointed out in Sec. 5.3.4 that in this case the hypergeometric function terminates at a finite order n. Thus, the resulting eigenfunction is an nth order polynomial in the parameter $z = r^2/R^2$. The explicit result follows from Eqs. (5.31), (5.32) and (5.40) as

$$\begin{aligned} f_\ell^{\rm in}(r,\omega_{n\ell,\infty}) &= r^\ell \sum_{k=0}^{n} \frac{(-n)_k}{k!} \frac{(\alpha_\ell + n)_k}{(\alpha_\ell)_k} \left(\frac{r}{R}\right)^{2k} \\ &\propto r^\ell P_n^{(\ell+1/2,0)}\left(1 - \frac{2r^2}{R^2}\right), \end{aligned} \tag{5.46}$$

which can be identified as a particular form of Jacobi polynomials $P_n^{(\ell+1/2,0)}(x)$ [142, 144]. This is in agreement with Stringari's results for the perturbed *density* in the Bose gas [138], see Ref. [148] for an expression in terms of the hypergeometric function. In this case, the density serves as the "potential" for the perturbed velocity, i.e., $\hat{\boldsymbol{u}}_1 \propto \nabla \hat{n}_1$.

For $n = 0$, the sum in Eq. (5.46) is just a constant, and it is readily seen that the eigenmodes are equivalent to the (incompressible) surface modes in a Coulomb system. At finite ξ, the form of the eigenfunctions is only slightly changed, in particular, there exist no radial nodes. In the case of the center-of-mass modes with $(n,\ell) = (0,1)$, $\Omega_1 = 1$ is a solution for any ξ. Consequently, the associated eigenfunctions are also independent of ξ and read $\hat{\phi}_1^{\rm in}(\boldsymbol{r},\omega_{01}) \sim r Y_{1m}(\theta,\varphi)$.

Several eigenmodes with $n > 0$ are depicted in Fig. 5.4. It shows that the number of radial nodes is determined by the mode number n. Upon increase of n, the radial structure of the eigenfunction becomes more oscillatory, and the modes have several minima and maxima. On the other hand, an increase of ℓ leads to a shift of the extrema and the excitation toward the surface.

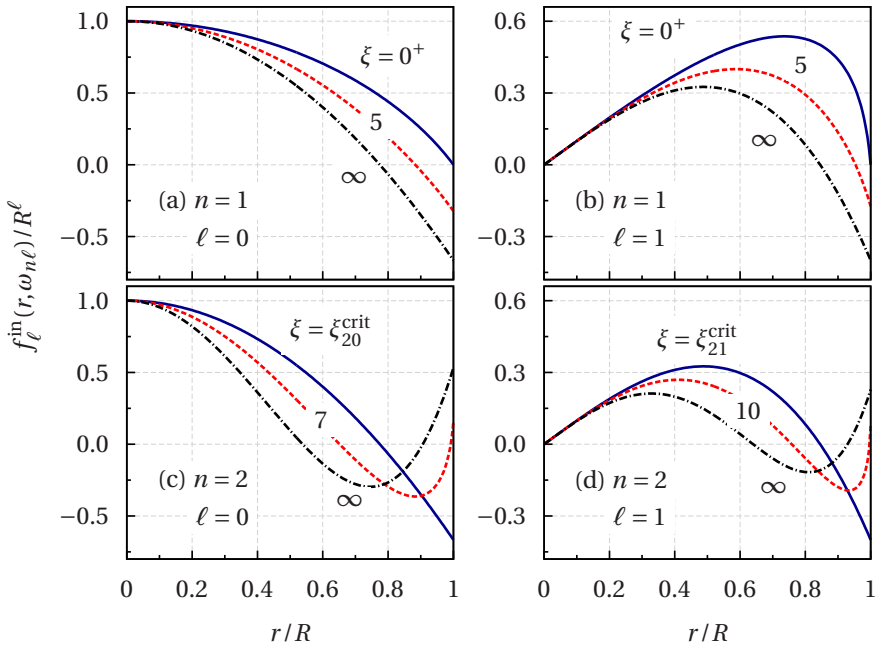

Figure 5.5: Radial eigenfunctions for various ξ's and mode numbers (n,ℓ). From Ref. [131]. Copyright (2010) by the American Physical Society.

Following the modes with $n > 0$ from $\xi = \infty$ to $\xi = 0$, one must differentiate between those with $n = 1$ and $\ell = 0,1,2$ that extend up to $\xi = 0$, and those that vanish below a critical $\xi_{n\ell}^{\mathrm{crit}}$. In the former case, the radial eigenfunctions at $\xi = 0^+$ can be written as

$$f_\ell^{\mathrm{in}}(r,\sqrt{3}\omega_0) = r^\ell \, {}_2F_1\left(\frac{\alpha_\ell - \delta_\ell}{2}, \frac{\alpha_\ell + \delta_\ell}{2}; \alpha_\ell; \frac{(r/R)^2}{3-2c_\ell}\right), \tag{5.47}$$

where δ_ℓ must be evaluated at $\Omega_{\mathrm{p}}^2 = 3$. The choice of the coefficients c_ℓ ensures that $f_\ell^{\mathrm{in}}(R,\sqrt{3}\omega_0) = 0$—as required for the bulk modes in the Coulomb limit. Consequently, they also exist in a genuine Coulomb system, where they simply belong to the large class of bulk modes. For finite ξ, the root at $r = R$ becomes a node inside the plasma region, see Figs. 5.5(a) and (b).

The other modes with $n > 0$ display a different behavior [Figs. 5.5(c) and (d)]. As ξ decreases and the critical $\xi_{n\ell}^{\mathrm{crit}}$ is approached from above, the outermost node is displaced toward the plasma boundary. The radial eigenfunction exhibits a strong variation near the plasma edge. In Figs. 5.5(c) and (d), the solution of Eq. (5.31) with the eigenfrequency at the critical point [Eq. (5.44)] is shown for comparison. Even though the eigenfunction tends toward this limit, there is an important difference: For $\xi \gtrsim \xi_{n\ell}^{\mathrm{crit}}$ the potential has a node in the close vicinity of the plasma edge that is absent in the limiting form. The first-order velocities are related to the perturbed potential by $\hat{\boldsymbol{u}}_1 \sim \nabla\hat{\phi}_1$, see Eq. (5.5b). Since the radial gradient of the aforementioned modes is very steep near the plasma edge for $\xi \gtrsim \xi_{n\ell}^{\mathrm{crit}}$, the excitation is primarily located near the surface.

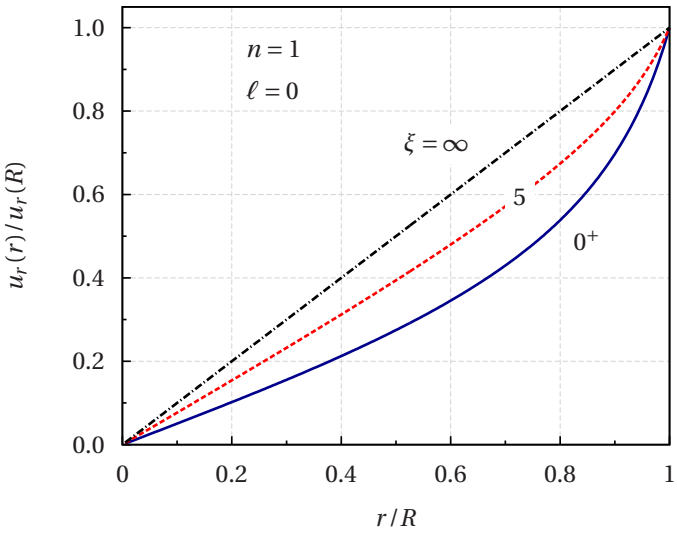

Figure 5.6: Radial fluid velocity $u_r(r) \sim \left(f_0^{\text{in}}\right)'(r,\omega_{10})$ of the lowest monopole mode for different ξ's. From Ref. [131]. Copyright (2010) by the American Physical Society.

Breathing Mode

Among the various normal modes, the breathing mode has been of particular interest recently [13, 14, 120] and therefore deserves a closer inspection. It is the lowest mode with spherical symmetry, i.e., its indices are $\ell = 0$ and $n = 1$. The very general analysis performed in Ref. [13] shows that a universal breathing mode with uniform particle displacements $\propto \boldsymbol{r}_i^s$ exists only for power-law interparticle forces and harmonic confinement potentials. Here, the $\{\boldsymbol{r}_i^s\}$ denote the equilibrium positions of the particles in a stationary state s. For a Coulomb system in a harmonic trap, these conditions are fulfilled, and the breathing frequency is given by $\Omega_{\text{br}} = \sqrt{3}$. On the other hand, the Yukawa potential does not satisfy the criteria and therefore no universal breathing mode exists [13]. Nevertheless, the lowest monopole mode in the cold-fluid theory is very similar to a uniform breathing mode.

In the limit $\xi \to \infty$, the eigenfunction for $(n,\ell) = (1,0)$ has a constant and a quadratic term, leading to $\hat{\boldsymbol{u}}_1 \sim r\hat{e}_r$, where $\hat{e}_r$ is the unit vector in the radial direction [Eq. (5.5b)]. This shows that the lowest monopole mode corresponds to a uniform breathing mode in the macroscopic limit. However, for finite ξ the uniformity condition is violated, see Fig. 5.6. In the limit $\xi \to 0$, one would expect that it is restored. However, this is not true, and the mode form becomes even more non-uniform. On the other hand, this observation is not alarming either since the mode is a valid solution of the eigenmode equations. The correct breathing mode in the Coulomb limit is given by $\hat{\phi}_1^{\text{in}}(r) \sim (r^2 - R^2)$ [121], which has both the quadratic r-dependence and satisfies the boundary condition $\hat{\phi}_1^{\text{in}}(R) = 0$.

The breathing mode for a harmonically confined Yukawa plasma has been investigated by Sheridan [120] by assuming both the density and the particle displacements to be uni-

form. Comparing the eigenfrequencies with those obtained here, it is found that the two expressions agree to within 0.5% as a function of the dimensionless plasma radius $\xi = \kappa R$. One must note, however, that the parameter ξ introduced by Sheridan involves the radius for a *homogeneous* sphere.

5.4 Summary

Based on previous results for the ground state density profile [76], analytic expressions have been presented for the total energy and the density moments of a confined Yukawa plasma. The density moments could be useful for a determination of the plasma parameter $\xi = \kappa R$ and the radius R from experimental data. Furthermore, the linearized cold-fluid equations have been solved to extend the static results to a time-dependent theory, which represents the main result of this chapter.

While waves in a uniform plasma are specified by a wave vector $\boldsymbol{k}$, the cold-fluid eigenmodes of a harmonically confined Yukawa plasma are characterized by a radial mode number n and two angular mode numbers (ℓ, m). Their frequencies depend on the single parameter ξ (or equivalently, the product $k_\mathrm{C} = \kappa a N^{1/3}$), increase monotonically with ξ, and saturate in the limit $\xi \to \infty$. It has been shown that the degeneracy of the Coulomb bulk modes is lifted in a Yukawa system and that several new modes appear upon increase of ξ. In the limit $\xi \to \infty$, the results for a trapped (Bose) gas with an effective local delta potential [138] have been recovered.

In agreement with previous results based on the harmonic approximation [13], the fluid theory confirms that a uniform breathing mode does not exist in harmonically confined Yukawa plasmas. Surprisingly, the largest deviations from the uniformity condition occur for $\xi \ll 1$, whereas it is restored in the limit $\xi \to \infty$.

Related Journal Publication

- H. Kählert and M. Bonitz, *Fluid modes of a spherically confined Yukawa plasma*, Phys. Rev. E **82**, 036407 (2010)

CHAPTER 6

Molecular Dynamics Simulation of Collective Excitations

The normal mode theory presented in the previous chapter is based on the cold-fluid equations, i.e., correlation and thermal effects are completely neglected. A more sophisticated analysis is required in order to fully understand the mode spectrum of strongly coupled Yukawa Balls. For a uniform (Yukawa) one-component plasma, molecular dynamics (MD) simulations provided a wealth of additional information about the collective modes, e.g., the existence of harmonics of the plasma frequency [149] or shear modes with a cut-off at finite wave vectors [12]. In addition to the mode frequencies, the wave spectra from MD simulation also yield the damping rates via the peak widths [108]. They contain all correlation and finite temperature effects and thus offer an exact description of the collective excitations.

The good agreement of the cold-fluid theory with both simulations [121] and experiments [133, 134] in the case of confined ions motivated its application to Yukawa Balls (Ch. 5). For these systems, the accuracy of the mean-field approach to the ground state was analyzed in Ref. [76]. While the agreement with exact results was good for weak and moderate screening parameters, the deviations were found to increase in systems with very short-ranged interaction. Thus, it is essential to evaluate the accuracy of the cold-fluid equations for the normal modes as well.

In the frame of this work, molecular dynamics simulations have been performed that reveal both the complete excitation spectrum and the applicability limits of the fluid theory for Yukawa systems [135]. They will be presented in this chapter. Mode spectra are analyzed for a wide range of screening and coupling parameters. They show that the agreement between theory and simulation strongly depends on the particular normal mode and the screening parameter, while temperature effects are rather weak. A qualitatively new mode is observed in the MD spectra at strong coupling. In order to explore the possibility of observing the normal modes in Yukawa Ball experiments, Langevin dynamics simulations with a finite damping rate are presented. Complementary to the finite temperature MD simulations, the theory is compared with the exact eigenmodes of a crystal-

lized plasma. A detailed analysis of the breathing mode reveals its complex temperature dependence and further elucidates the shortcomings of the fluid theory.

The chapter is organized as follows.[1] The details of the simulation method are given in Sec. 6.1. This is followed by a discussion of the MD mode spectra in Sec. 6.2 and the comparison with crystal eigenmodes in Sec. 6.3. The chapter concludes with a summary of the excitation spectrum in Sec. 6.4.

6.1 Simulation Method

6.1.1 Preparation of the System

The MD simulations are based on the Hamiltonian (3.5) for particles in an isotropic, harmonic confinement interacting via the Yukawa potential. This corresponds to an exact description of the same physical system as the approximate fluid treatment in the previous chapter. The Hamiltonian is the same as in Ch. 4, but the simulation method is substantially different.

The screening and coupling dependence of the normal modes is investigated with equilibrium microcanonical simulations using the velocity Verlet algorithm (3.15). For a chosen $\Gamma = q^2/(a\,k_\mathrm{B}T)$, the kinetic energy in the simulation must satisfy $\langle E_\mathrm{kin}\rangle = 3Nk_\mathrm{B}T/2$, where the brackets denote a time average. This is achieved by rescaling the velocities in the equilibration phase. Typically, the mean kinetic energy during the actual simulation is slightly different from the desired value. However, the deviations are rather small and have negligible influence on the mode spectra. In order to create well-defined conditions, any residual linear and angular momentum of the whole plasma are removed. Since the external confinement is isotropic, the total *angular* momentum of the cluster is a conserved quantity [107]. The total *linear* momentum is associated with the center-of-mass (COM) motion and is only of minor interest here, because the COM mode is an exact eigenmode in a harmonic trap [147].

For the simulations with a finite damping rate, the SLO scheme (3.18) is used for the integration of the Langevin equation (3.16). In this case, equilibration of the cluster at the Langevin temperature is established by the action of the random and frictional forces.

6.1.2 Mode Detection

For a spheroidal Coulomb plasma, the fluid eigenmodes were detected in MD simulations by calculating multipole moments of the density [121]. With some modifications to account for the different particle interaction, the same technique can be applied here as well.

The starting point is the general solution of the screened Poisson equation for an arbitrary density $n(\boldsymbol{r},t)$ [76],

$$\phi(\boldsymbol{r},t) = q\int n(\boldsymbol{r}',t)\,\frac{e^{-\kappa|\boldsymbol{r}-\boldsymbol{r}'|}}{|\boldsymbol{r}-\boldsymbol{r}'|}\,d\boldsymbol{r}', \tag{6.1}$$

[1] This chapter is based on a revised version of Ref. [135].

where the Yukawa potential is the associated Green's function with the boundary condition $\phi(\boldsymbol{r},t) \to 0$ for $|\boldsymbol{r}| \to \infty$ [140].

In the next step, the Green's function is replaced by its corresponding expansion in modified spherical Bessel functions [see Eq. (5.25)] and spherical harmonics [140],

$$\frac{e^{-\kappa|\boldsymbol{r}-\boldsymbol{r}'|}}{|\boldsymbol{r}-\boldsymbol{r}'|} = 4\pi\kappa \sum_{\ell,m} i_\ell(\kappa r_<)\, k_\ell(\kappa r_>)\, Y^*_{\ell m}(\theta',\varphi')\, Y_{\ell m}(\theta,\varphi).$$

They are the radial solutions of the associated *homogeneous* equation, see Sec. 5.3.3. The arguments $r_< = \min(|\boldsymbol{r}|,|\boldsymbol{r}'|)$ and $r_> = \max(|\boldsymbol{r}|,|\boldsymbol{r}'|)$ are familiar from the equivalent expansion of the Coulomb potential.

Following Dubin and Schiffer [121], it is now possible to calculate multipole moments of the density. Using the expansion of the Yukawa potential in Eq. (6.1), the spatial dependence of the potential can be separated from the density integration, and one can define the time-dependent multipole moments as

$$q_{\ell m}(t) = q\sqrt{\frac{4\pi}{2\ell+1}} \int n(\boldsymbol{r}',t)\, \hat{\imath}_\ell(\kappa,r')\, Y^*_{\ell m}(\theta',\varphi')\, d\boldsymbol{r}'. \tag{6.2}$$

The Bessel functions are used in the following form,

$$\hat{\imath}_\ell(\kappa,r) = \frac{(2\ell+1)!!}{\kappa^\ell}\, i_\ell(\kappa r), \qquad \hat{k}_\ell(\kappa,r) = \frac{\kappa^{\ell+1}}{(2\ell-1)!!}\, k_\ell(\kappa r),$$

which ensures that the corresponding expressions for the Coulomb case [107], where the Bessel functions now reduce to $\hat{\imath}_\ell(\kappa,r) \to r^\ell$ and $\hat{k}_\ell(\kappa,r) \to r^{-(\ell+1)}$ [140], are recovered in the limit $\kappa \to 0$.

In using $r_<$ as integration variable, it is assumed that the observation point $\boldsymbol{r}$ for the potential is outside the smallest sphere where the density is non-zero, i.e., $|\boldsymbol{r}| > |\boldsymbol{r}'|$ for all $\boldsymbol{r}'$ with $n(\boldsymbol{r}',t) \neq 0$. The result for the potential (6.1) can then be rewritten as

$$\phi(\boldsymbol{r},t) = \sum_{\ell,m} \sqrt{\frac{4\pi}{2\ell+1}}\, q_{\ell m}(t)\, \hat{k}_\ell(\kappa,r)\, Y_{\ell m}(\theta,\varphi), \tag{6.3}$$

where the full time-dependence is now contained in the multipole moments (6.2).[2] A comparison of Eq. (6.3) with the form of the perturbed potential outside the plasma in the fluid approach [Eqs. (5.22) and (5.26)] shows that the functional dependence is completely equivalent. Thus, the multipole moments (6.2) contain all possible oscillations of the potential for given ℓ and m [121].

In the simulation, the density is a sum of point particles with (spherical) coordinates $\{r_i(t),\theta_i(t),\varphi_i(t)\}$, and Eq. (6.2) reduces to

$$q_{\ell m}(t) = q\sqrt{\frac{4\pi}{2\ell+1}} \sum_{i=1}^{N} \hat{\imath}_\ell(\kappa,r_i(t))\, Y^*_{\ell m}(\theta_i(t),\varphi_i(t)). \tag{6.4}$$

[2] A general study of Yukawa electrostatics in the context of electrolyte solutions can be found in Ref. [150]. In particular, the authors derive the true asymptotic expansion of the potential in powers of $\exp(-\kappa r)/r^n$, where $n \in \mathbb{N}$. In contrast to the Coulomb limit, they find that all multipole moments contribute to the lowest order term ($n = 1$).

In order to identify the collective modes in the time series of the multipole moments, the associated power spectral density is calculated (see, e.g., Ref. [151]),

$$\mathcal{Q}_{\ell m}(\omega) = \lim_{T\to\infty} \frac{|\mathcal{F}(q_{\ell m}(t)/N, T, \omega)|^2}{T}, \tag{6.5}$$

where $\mathcal{F}(f(t), T, \omega)$ denotes the Fourier transform of $f(t)$ over a finite time interval T.[3] Maxima of $\mathcal{Q}_{\ell m}(\omega)$ indicate frequencies at which the system supports collective modes.

At finite temperature, the normal modes are thermally excited and manifest themselves as fluctuations around equilibrium quantities. Therefore, an external driving mechanism or an initial perturbation of the system [121] is not necessarily required.

6.2 Simulation Results

As discussed in Sec. 4.1, the properties of the N-particle system depend on the coupling parameter $\Gamma = q^2/(a\, k_\mathrm{B} T)$ and the screening parameter κa. It should be noted again that their *combination* determines the effective coupling strength of the system [123, 124], cf. the discussion in Sec. 4.2.3. In the following, the screening dependence is investigated at constant Γ even if this leads to systems with different effective coupling. Compared to a uniform system, an analysis of these effects in a harmonic trap is complicated by the simultaneous change of the mean density profile with the screening parameter [76]. The temperature dependence is investigated separately by performing simulations at constant κa with variable Γ. A detailed investigation of the effective coupling strength or the melting process in large-sized Yukawa Balls as performed by Schiffer for Coulomb systems [70] is beyond the scope of this work; for small systems, see Refs. [82, 86].

6.2.1 Screening Dependence

A detailed study of the Coulomb modes has been carried out by Dubin and Schiffer [121]. Here, the main objective is to investigate the change of the mode spectra with the screening parameter, which is shown in Fig. 6.1 for a fixed coupling parameter $\Gamma = 150$ and two different particle numbers. Near the Coulomb limit ($\kappa a \ll 1$), the mode spectra exhibit maxima in the vicinity of the surface mode frequencies $\Omega = \omega/\omega_0 = \sqrt{3\ell/(2\ell+1)}$ [115]. Since the center-of-mass motion has been removed in the equilibration phase, there is no peak for $\ell = 1$. In the simulations with a finite friction coefficient, a well pronounced maximum is observed at the expected position. For $\kappa = 0$, the monopole moment $\mathcal{Q}_{00}$ is simply the total charge of the cluster and therefore a constant, i.e., it has only a static Fourier component. In addition to the surface modes, the multipole spectra have maxima close to the Coulomb plasma frequency, $\Omega = \sqrt{3}$ [115].

The fluid theory discussed in the previous chapter predicts an increase of the mode frequencies and the appearance of new modes upon increase of κa. In general, the MD mode spectra confirm these results. Nevertheless, important differences are observed as well, which will be discussed in the following.

[3] The spectra are obtained using a Hann window function and are moderately smoothed. Numerical routines for Fourier transforms were kindly provided by David Hochstuhl.

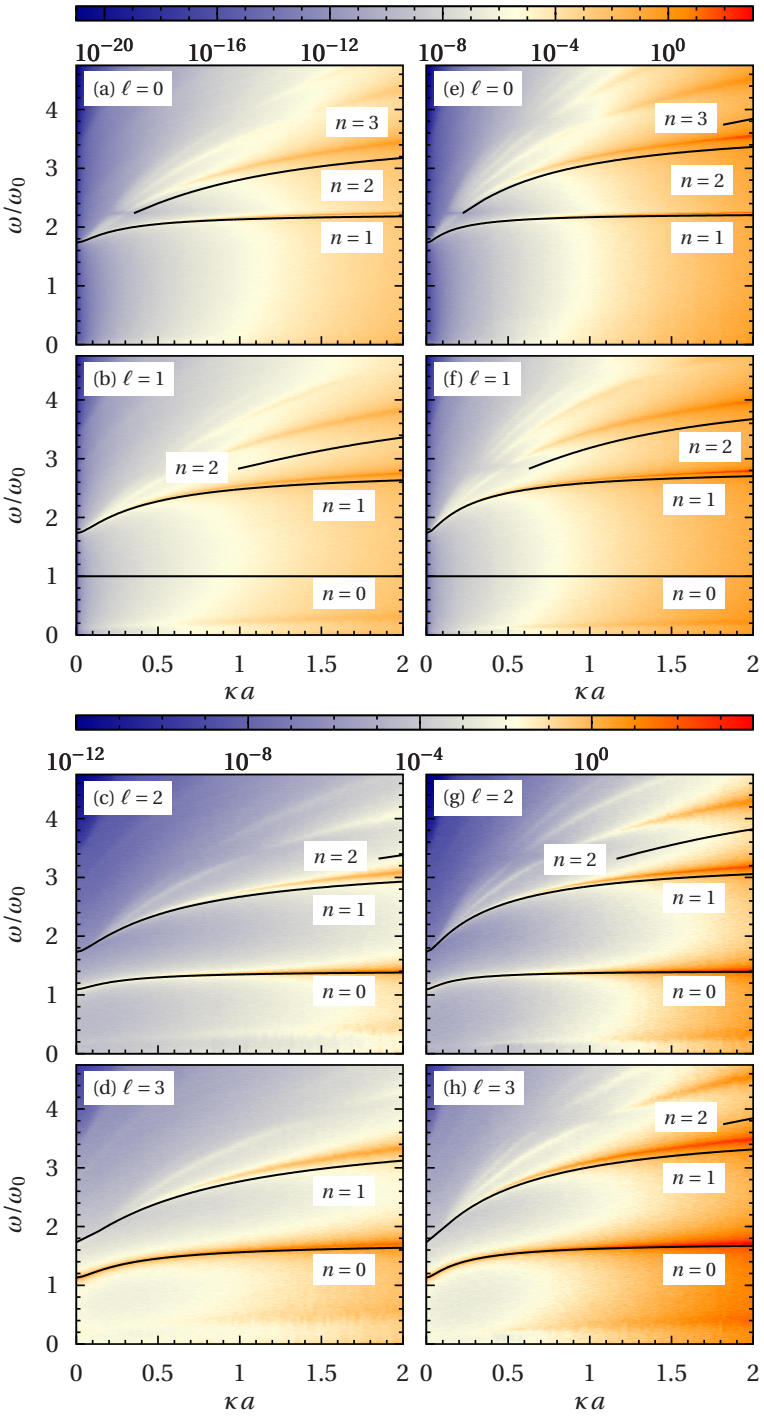

Figure 6.1: Screening dependence of the $m = 0$ multipole spectra $\mathcal{Q}_{\ell 0}(\omega)$ (arb. units) for $N = 1000$ (left column) and $N = 4000$ particles (right column) at $\Gamma = 150$ without friction. The solid lines show the results of the cold-fluid theory. From Ref. [135]. Copyright (2011) by the American Physical Society.

Monopole Modes

The first monopole ($\ell = 0$) mode is the breathing mode with $n = 1$, cf. Sec. 5.3.5. For this particular excitation, the simulations are in very good agreement with the results of the cold-fluid theory, see Figs. 6.1(a) and (e). The small deviations between the two methods increase with the screening parameter. A second mode is evident in the simulation results with a frequency above the breathing mode. Comparison with the theory shows that this corresponds to the $n = 2$ mode. The cold-fluid theory predicts its existence only beyond $\xi_{20}^{\mathrm{crit}} \approx 2.73$, see Eq. (5.43), which corresponds to $\kappa a \approx 0.35$ and $\kappa a \approx 0.22$, for $N = 1000$ and $N = 4000$, respectively. While this is in good agreement with the simulations, the frequencies are shifted upward by a small amount. The deviations are less pronounced for the larger cluster with 4000 particles, though.

For the few higher order modes observed in the MD spectra, the disagreement with the cold-fluid theory becomes obvious since (i) they do not yet exist in the theory at the simulated screening parameters (see $n = 3$ for $N = 1000$), and (ii) the frequency upshift is rather large ($n = 3$ for $N = 4000$).

Dipole Modes

In the case of the dipole modes ($\ell = 1$), the first mode has the radial index $n = 0$ and corresponds to the center-of-mass motion. In a harmonic trap, the center-of-mass coordinate $\boldsymbol{R} = N^{-1} \sum_{i=1}^{N} \boldsymbol{r}_i$ separately fulfills the equation of motion of a harmonic oscillator with frequency $\Omega_1 = 1$ [74] and is an exact mode. This also implies that it is undamped and independent of Γ and κa (i.e., the particle interaction [147]). For these reasons and since the cold-fluid correctly predicts the frequency, it is only of minor interest here.

For the high-order modes ($n \geq 1$), the observations made for the monopole modes are also valid here. The agreement between theory and simulation is very good for $n = 1$ at low screening, but the deviations increase for larger κa. The $n = 2$ mode exists in the theory only for $\xi > \xi_{21}^{\mathrm{crit}}$, which agrees well with the MD simulation. Again, there is a small upshift of the MD frequencies with respect to those of the cold-fluid theory. In general, the deviations are smaller for the larger cluster with $N = 4000$. The agreement considerably degrades for $n \geq 3$, and the cold-fluid theory no longer captures the correct starting points.

The main difference compared to the monopole spectra is the appearance of a low frequency mode, which constitutes a new qualitative feature. Its frequency is only weakly dependent on the screening parameter and lower for $N = 4000$ than for $N = 1000$. No such excitation has been predicted by the fluid theory.

Quadrupole and Octupole Modes

The observations for the quadrupole and octupole modes with $n \geq 1$ are not qualitatively different from those for the monopole and dipole modes. There is good agreement for the $n = 1$ mode and a rather substantial frequency upshift for $n = 2$. On examining the starting points for the higher order modes ($n \geq 2$), it is found that the accuracy of the fluid theory degrades again. Only for $N = 4000$ and $\ell = 2$ the agreement is still satisfactory, see

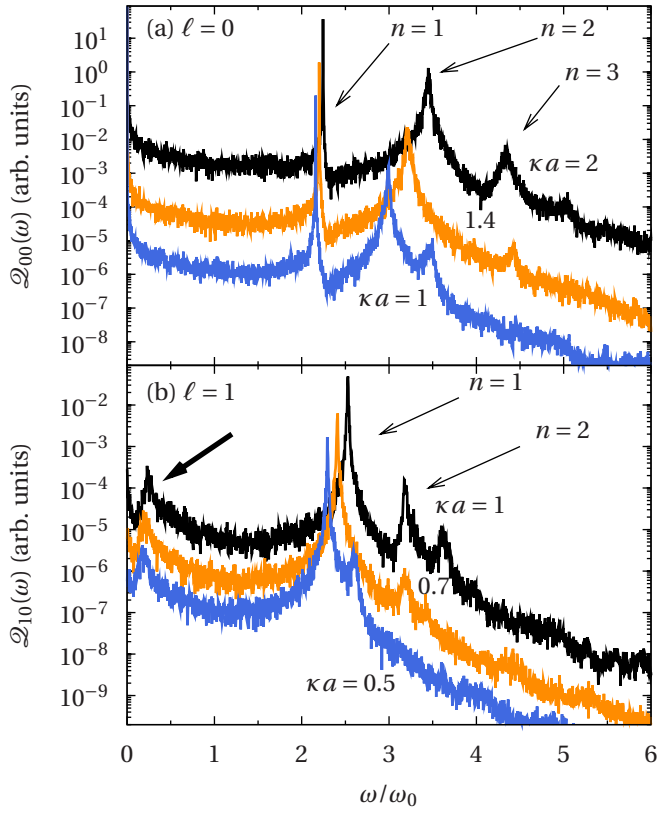

Figure 6.2: (a) Monopole and (b) dipole spectra for various screening parameters with $N = 1000$ particles at $\Gamma = 150$. The thick arrow in (b) indicates the low frequency peak in the dipole spectrum. From Ref. [135]. Copyright (2011) by the American Physical Society.

Fig. 6.1(g). The $\ell = 2$ and $\ell = 3$ spectra exhibit the same kind of low frequency excitations as the dipole spectrum, which the cold-fluid theory fails to predict.

In addition, the quadrupole and octupole spectra show the first non-trivial eigenmodes with the radial index $n = 0$. For these modes, the accuracy of the fluid theory is very good. The general agreement is comparable to that of the $n = 1$ modes, i.e., excellent at low screening and slightly worse at larger κa.

Reentrant Behavior of Normal Modes

Figure 6.2 allows for a more detailed inspection of the multipole spectra. In particular, it shows that the behavior of the modes with $n \geq 2$ is partially different from the predictions of the previous chapter, which has not been discussed so far. The simulations clearly reveal that the excitation peaks do not completely vanish at a particular value of κa but reappear at lower screening, see also Fig. 6.1.

Consider the case $n = 3$ for the monopole modes [Fig. 6.2(a)]. The spectrum shows a clear maximum at $\kappa a = 2$. Even though it has completely disappeared from the spectrum at $\kappa a = 1.4$, it reappears at $\kappa a = 1$. A similar observation is made for the $n = 2$ dipole mode [Fig. 6.2(b)]. The second maximum in the $\kappa a = 1$ spectrum does not exist at the expected position in the $\kappa a = 0.7$ spectrum but reappears at a lower screening value $\kappa a = 0.5$. These excitations are not contained in the eigenfrequency spectrum derived in Ch. 5. However,

they could be due to the part of the cold-fluid spectrum with frequencies in the interval $\Omega_\mathrm{p}(\xi) < \Omega < \Omega_\mathrm{p}(0)$, see Fig. 5.2.

Discussion

The comparison between the exact MD simulations and the cold-fluid theory has revealed good agreement for the low-order modes and weak to moderate screening parameters. This behavior can partially be understood by resorting to the results for a macroscopic system (see the discussions in Sec. 3.2.3 and Ref. [121]). While the cold-fluid result for the dispersion relation qualitatively describes the (acoustic) long-wavelength regime, it completely fails to reproduce the results for intermediate and short-wavelength oscillations, e.g., the observed negative dispersion or the oscillatory behavior at strong coupling [11, 12, 99]. This is an inherent inability of the mean-field continuum theory. Since it does not contain any information about the (short-range) correlations in the system, it is incapable of resolving oscillations on a length scale of a few inter-particle distances.

This explains why the agreement between the cold-fluid theory and the MD simulations is only good for the low-order modes. Figures 5.4 and 5.5 in Ch. 5 show that the eigenmodes of the cold-fluid theory become more oscillatory when the radial mode index n increases. The same applies to the angular eigenfunctions. Thus, the excitations occur on increasingly smaller length scales, which corresponds to larger wave vectors in a homogeneous system. Provided the cold-fluid form of the potential eigenfunctions is approximately valid in the simulation, the improved agreement for larger systems can be explained by the increased cluster size R, which stretches and forms an upper limit for the length scale on which the oscillations occur.

More insight can be gained by resorting to previous comparisons of the density profile with simulations. It was shown by Henning *et al.* [76] that the mean-field density profile increasingly deviates from the *average* density obtained from exact MD simulations at large screening parameters. The inclusion of correlation effects via the local-density approximation (LDA) removed the discrepancies [77]. Very similar behavior is observed for the low-order modes ($n = 0, 1$) here: While the theory accurately describes the MD frequencies at low screening, the deviations increase with κa. Since the present normal mode theory is directly based on the density profile *without* correlations, this can (at least partially) be attributed to an inaccurate density. For Coulomb systems it was shown that *average* correlation properties are sufficient to obtain the frequency corrections for the low-order modes—without having to resolve the particular details of the density profile [115, 121].

Even the improved LDA result only describes the average trap density. In order to reproduce the shell structure of Yukawa Balls, short-range correlations must be taken into account [82], e.g., via the hypernetted-chain approximation [87–90]. These effects should become particularly important for the high-order fluid modes which are associated with small-scale excitations. In the quasi-localized charge approximation [99], this is demonstrated by the non-monotonic (oscillatory) behavior of $\omega(k)$ or the Einstein frequency (the $k \to \infty$ limit of the dispersion relation), which generally lies below the cold-fluid (mean-field) result ω_p.

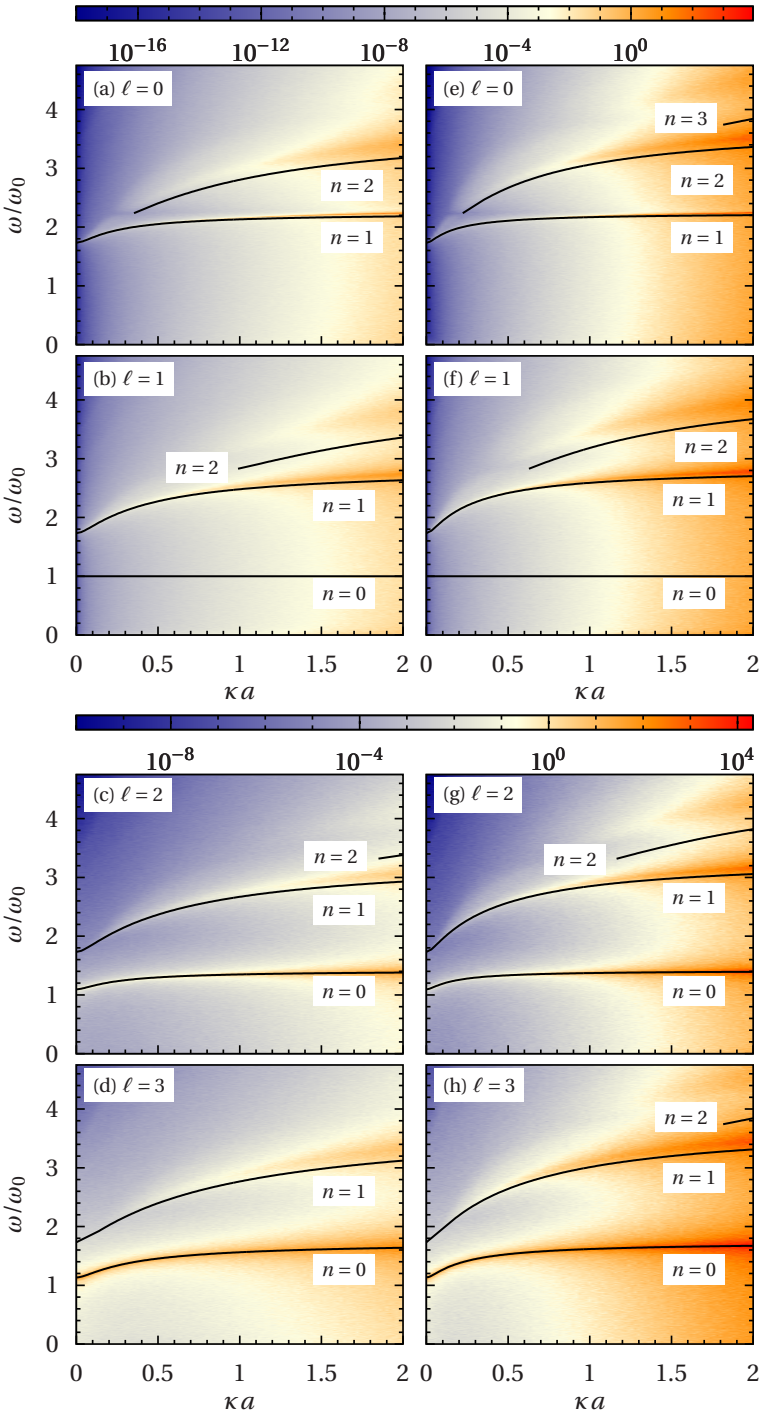

Figure 6.3: Screening dependence of the $m = 0$ multipole spectra $\mathcal{Q}_{\ell 0}(\omega)$ (arb. units) for $N = 1000$ (left column) and $N = 4000$ particles (right column) at $\Gamma = 30$ without friction. The solid lines show the results of the cold-fluid theory. From Ref. [135]. Copyright (2011) by the American Physical Society.

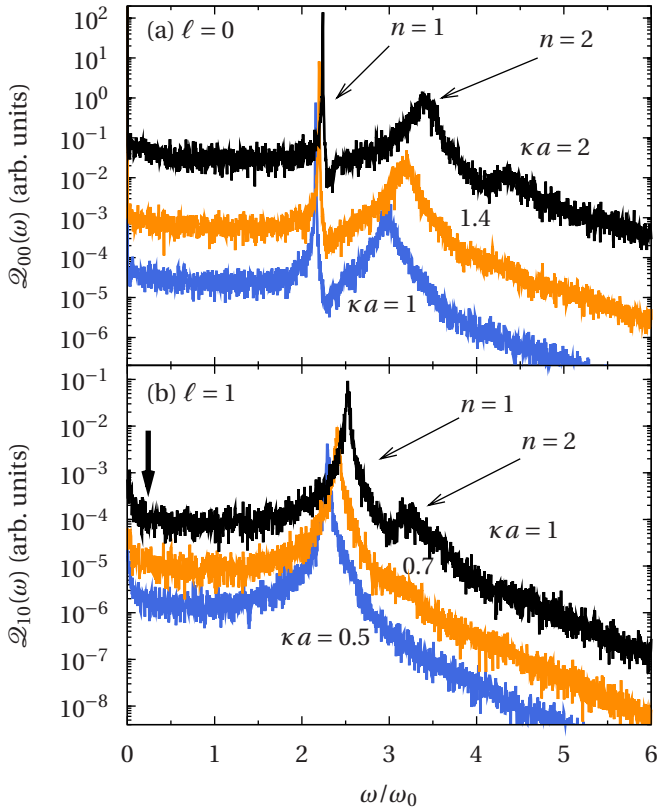

Figure 6.4: Same as Fig. 6.2 for $\Gamma = 30$. (a) Monopole and (b) dipole spectra for various screening parameters with $N = 1000$ particles. The thick arrow indicates the position of the low frequency mode for $\Gamma = 150$. From Ref. [135]. Copyright (2011) by the American Physical Society.

6.2.2 Influence of Coupling Parameter

Thermal effects on the mode spectra are controlled by the coupling parameter Γ. Figure 6.3 shows the same spectra as Fig. 6.1 but for a five times reduced coupling ($\Gamma = 30$). The main difference between these two systems is the density profile. At high Γ, the system exhibits a clear structure with well-defined radial shells, cf. Ch. 4. At intermediate Γ, however, the shell structure disappears, and the density is well described by the cold-fluid (mean-field) result, except for the boundary. At this point, the cold-fluid density [Eq. (5.9)] has a step profile [76], while the simulation result smoothly decays to zero. In addition, the density has one or several maxima near the boundary, depending on the exact coupling parameter, see Refs. [87, 88, 115]. Despite the lower Γ, the system is certainly still in the strong coupling regime.

Consider now the changes of the mode spectra. As one can see from Fig. 6.3, the mode frequencies are only weakly affected by the reduced coupling. The agreement between theory and simulation is very similar to the previous case for $\Gamma = 150$. However, qualitative changes of the spectra are observed. First, some of the high-order modes disappear and the maxima become broader—indicating a higher damping rate due to the increased temperature. Second, the low frequency modes in the $\ell = 1,2,3$ spectra disappear and, third, the effect of reappearing modes with $n \geq 2$ at lower κa is greatly reduced. In general, the maxima are less pronounced than before.

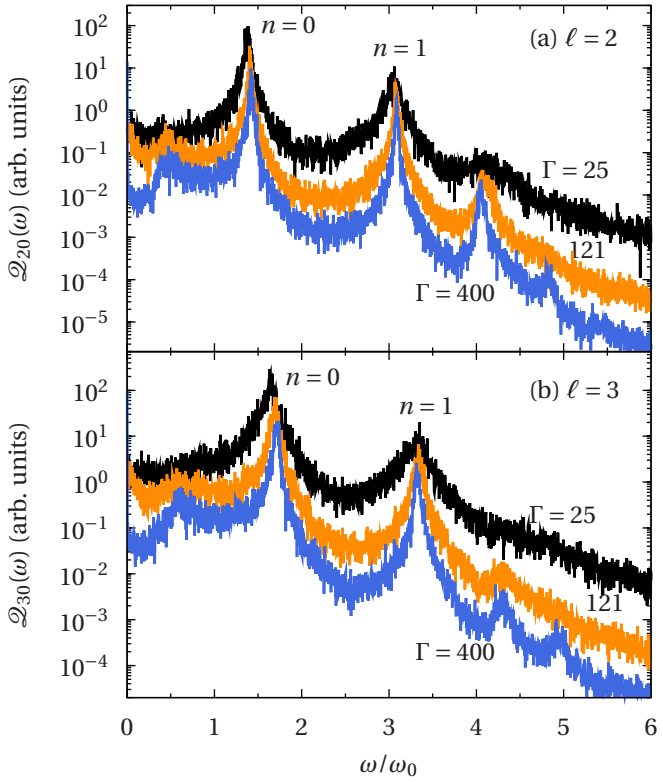

Figure 6.5: Quadrupole and octupole spectra for $N = 1000$ and $\kappa a = 2$ for three values of the coupling parameter Γ as indicated in the figure. From Ref. [135]. Copyright (2011) by the American Physical Society.

Figure 6.4 elucidates these effects in greater detail. It clearly shows that some of the high-order modes are missing and that the $n = 2$ mode is more strongly damped than for $\Gamma = 150$. Further, it does not reappear at lower screening ($\kappa a = 0.5$) in the dipole spectrum. The arrow in Fig. 6.4 shows the position of the low frequency mode in the dipole spectrum at $\Gamma = 150$ (see Fig. 6.2), which is completely absent at $\Gamma = 30$.

For a gradual change of the effects with the coupling parameter for the quadrupole and octupole modes, see Fig. 6.5. Evidently, the modes are most clearly defined at high coupling. As Γ is decreased the maxima become broader, whereas the peak positions are only marginally affected. The weak temperature dependence of the frequencies in the strongly coupled regime is especially apparent in Fig. 6.6. For the particular case of the breathing mode, a more detailed analysis is performed in Sec. 6.3.2. The high-order modes and the low frequency excitations vanish at weak coupling, while the low-order modes with $n = 1, 2$ are the most stable ones.

Discussion

The specific nature of the low frequency excitations is still unclear. However, a comparison with the (transverse) shear waves in a macroscopic OCP helps to interpret the results. These modes are known to exist only in strongly coupled systems, and their frequencies are typically below that of the longitudinal mode, at least for small wave vectors; see Refs. [12, 19]. Because they are due to correlation effects, they are not contained in a mean-

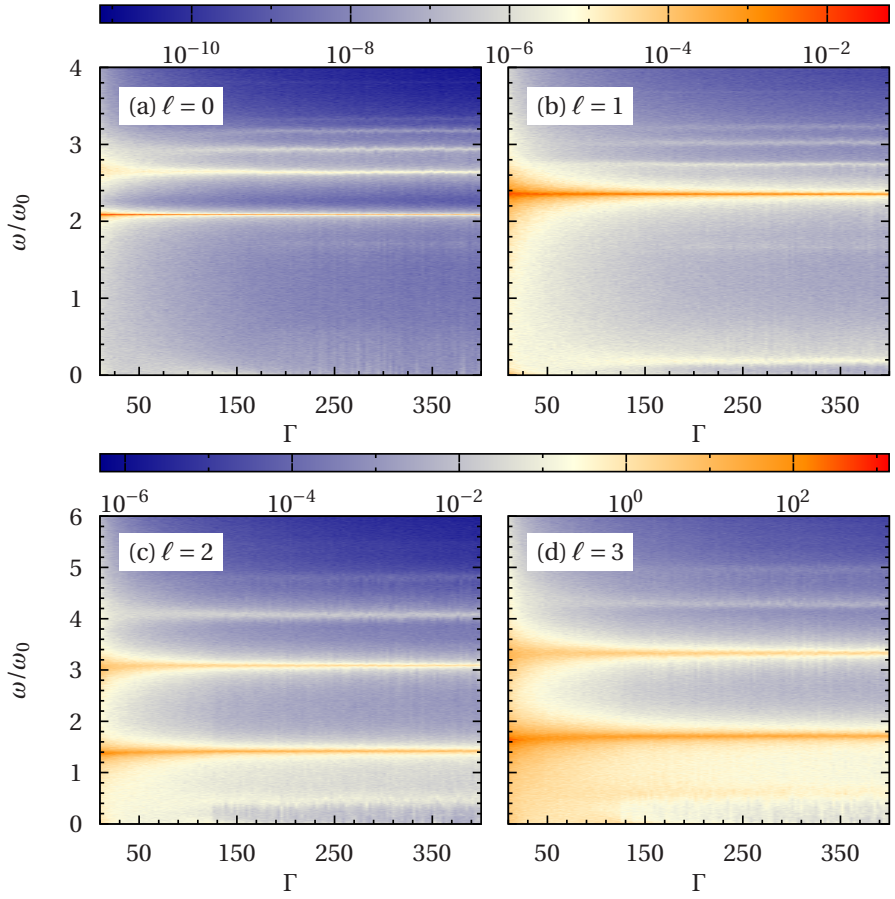

Figure 6.6: Influence of the coupling strength on the $m = 0$ multipole spectra $\mathscr{Q}_{\ell 0}$ (arb. units) for $N = 1000$ and $10 \le \Gamma \le 400$. The screening parameters are $\kappa a = 0.6$ (a),(b) and $\kappa a = 2$ (c),(d). From Ref. [135]. Copyright (2011) by the American Physical Society.

field theory but, e.g., in the QLCA [92, 99]. Similar modes occur in non-uniform confined Coulomb systems, see Refs. [115, 121].

Dubin and Schiffer [121] investigated incompressible torsional modes that arise from correlations in a crystallized Coulomb plasma. The frequency range they observed for these modes ($\omega \sim 0.06 \ldots 0.1\,\omega_0$ for $N = 1000$) is in reasonable agreement with that found for the low frequency modes here. Further, the analytic results they presented suggest a decrease of the frequencies with the cluster radius. This also applies to the present results, since the frequencies for the larger cluster with $N = 4000$ particles are found to be lower than for $N = 1000$. These observations indicate that the modes could be closely related. Screening generally increases their frequencies, see Figs. 6.1 and 6.2.

It should be noted that experimental mode spectra of a small Yukawa Ball with 31 particles [10] also contained a significant amount of low frequency modes with a high shear contribution. It would therefore be highly desirable to gain additional insight into the properties of the observed modes, which, however, requires a more sophisticated theory.

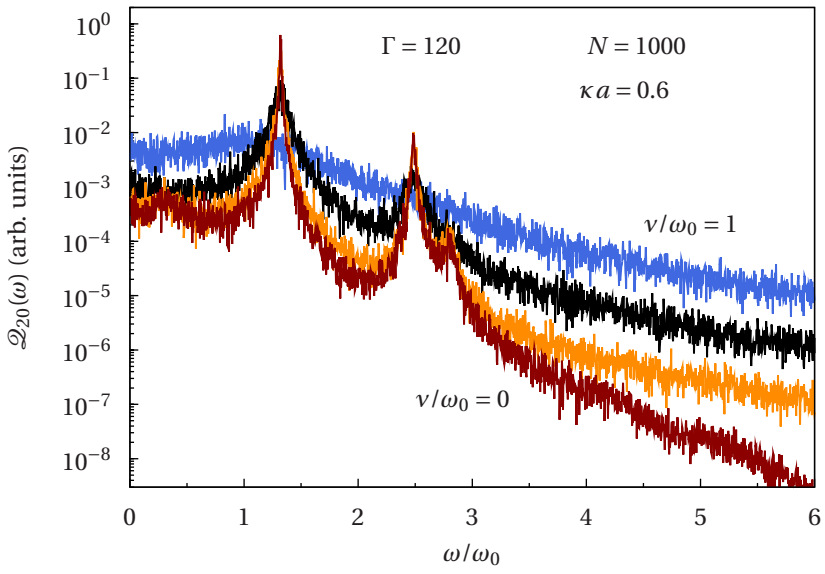

Figure 6.7: Influence of a finite damping coefficient on the quadrupole spectrum for the parameters indicated in the figure. Results are shown for $\nu/\omega_0 = 0, 0.01, 0.1, 1$. From Ref. [135]. Copyright (2011) by the American Physical Society.

6.2.3 Mode Spectra in the Presence of Dissipation

In dusty plasma experiments, the particles are subject to friction with the neutral gas. This must be taken into account for a comparison of simulations with experimental data [9]. Figure 6.7 shows simulation spectra obtained with a finite damping rate in addition to a spectrum without damping. In the zero damping limit, the spectrum has four maxima: two main peaks at $\Omega = 1.32, 2.48$ and two weaker maxima at $\Omega = 0.3, 2.8$. As the friction coefficient is increased, the width of the peaks increases. At rather weak damping ($\nu/\omega_0 = 0.01$), all four modes are still discernible. For intermediate damping ($\nu/\omega_0 = 0.1$), the low frequency peak vanishes, while the high frequency mode is still visible in the spectrum. Upon further increase of the damping coefficient ($\nu/\omega_0 = 1$) only the main peak ($n = 0$) "survives".

This shows that a low damping rate will be necessary to detect the low and high frequency excitations in experiments. Based on the observations in the previous section, the analysis would also benefit from a high coupling parameter. Thus, the experiments should ideally be performed at strong coupling conditions and low damping. Since a reduction of the gas pressure in Yukawa Ball experiments goes along with a change of the effective dust interaction potential [2, 52], it remains an open question if a parameter regime exists where (i) the damping rate is sufficiently low to detect the modes, and (ii) the theoretical model with the isotropic Yukawa potential is still applicable. Comparisons between high and low pressure experiments indicate indeed that the mode spectra depend on the details of the interaction [2].

6.3 Comparison with Crystal Eigenmodes

The approach to the collective modes presented in Ch. 5 is based on a continuum fluid model. A different method that is often employed specifically for small systems [9, 13, 74] or to study lattice vibrations [152] is based on the harmonic approximation of the potential energy. This theory provides an exact description of small amplitude excitations in a crystallized plasma. In a three-dimensional system, it yields $3N$ normal modes as opposed to the potential eigenmodes of the cold-fluid theory. In the following, the main ideas of the harmonic approximation are reviewed, and a sum rule is deduced for the squared eigenfrequencies. As a mode that has recently attracted particular attention [13, 14], the breathing mode is used to discuss the relations between the MD simulations, the cold-fluid theory, and the harmonic approximation. Furthermore, its temperature behavior is investigated.

6.3.1 Frequency Sum Rule

In the harmonic approximation, the potential energy of a stationary state s,

$$U^s = \sum_{i=1}^{N} V(\boldsymbol{r}_i^s) + \underbrace{\frac{1}{2}\sum_{i\neq j}^{N} v(|\boldsymbol{r}_{ij}^s|)}_{E_{\mathrm{int}}^s}, \tag{6.6}$$

is expanded in a Taylor series up to second order in the displacements from the equilibrium positions $\boldsymbol{r}_s^N = (\boldsymbol{r}_1^s, \ldots, \boldsymbol{r}_N^s)$ [9]. This could be either the ground or a metastable state. The (state dependent) interaction energy is denoted by E_{int}^s, while $v(r)$ is the (Yukawa) interaction potential and $V(\boldsymbol{r})$ the confinement. The resulting equation of motion for the displacements is linear and can be solved by diagonalization of the Hessian matrix $\mathscr{U}^s$. It contains the second derivatives of U with respect to the particle coordinates, i.e.,

$$\mathscr{U}^s = \left.\frac{\partial^2 U(\boldsymbol{r}^N)}{\partial r_i^\alpha \partial r_j^\beta}\right|_{\boldsymbol{r}^N=\boldsymbol{r}_s^N},$$

where $\alpha, \beta \in \{x, y, z\}$ and $i, j \in \{1, \ldots, N\}$. For a detailed discussion of the harmonic approximation, see Ref. [9].

A sum rule for particles with Coulomb interaction in a harmonic confinement $V(r) = m\omega_0^2 r^2/2$ is given by $\sum_{i=1}^{3N} m(\omega_i^s)^2 = N\omega_\mathrm{p}^2 = 3N\omega_0^2$ [121], which has the same form in a macroscopic homogeneous system. It is known as the Kohn sum rule [19, 153]. Here, $\omega_\mathrm{p}^2 = 3\omega_0^2$ is the plasma frequency associated with the mean-field density profile for $\kappa = 0$, see Eqs. (5.8) and (5.9). This is not entirely surprising because the harmonic confinement is equivalent to a homogeneous background charge [5]. For Yukawa interaction, this does not hold true any more, and the confinement equivalent to a homogeneous background depends on the screening parameter κ, as was demonstrated by Totsuji *et al.* [128, 129].

In general, the eigenvalues of a matrix are related to its trace by $\sum_{i=1}^{3N} m(\omega_i^s)^2 = \mathrm{Tr}(\mathscr{U}^s)$. This can be used to obtain a simple expression for the squared eigenfrequencies of a system with Yukawa interaction and any type of confinement. The trace of the Hessian matrix

$\mathscr{U}^s$ is given by

$$\mathrm{Tr}(\mathscr{U}^s) = \sum_{i=1}^{N} \Delta_i \left[\sum_{k=1}^{N} V(\boldsymbol{r}_k) + \frac{1}{2} \sum_{j\neq k}^{N} v(|\boldsymbol{r}_{jk}|) \right] \Bigg|_{\boldsymbol{r}^N = \boldsymbol{r}_s^N}, \tag{6.7}$$

see Eq. (6.6) for the explicit form of the potential energy.

The first (confinement) term in the above equation yields a single contribution for $i = k$. In order to simplify the second term in Eq. (6.7), the relation $(\Delta - \kappa^2) e^{-\kappa r}/r = -4\pi\delta(\boldsymbol{r})$ [76] can be employed. The delta function does not contribute to the result since $|\boldsymbol{r}_{ij}^s| \neq 0$. This leads to

$$\sum_{i=1}^{3N} m(\omega_i^s)^2 = \left(\sum_{i=1}^{N} \Delta_i V(\boldsymbol{r}_i) + \kappa^2 \sum_{i\neq j}^{N} q^2 \frac{e^{-\kappa|\boldsymbol{r}_{ij}|}}{|\boldsymbol{r}_{ij}|} \right) \Bigg|_{\boldsymbol{r}^N = \boldsymbol{r}_s^N}. \tag{6.8}$$

Up to a numerical factor, the second term in Eq. (6.8) can be identified as the interaction energy E_{int}^s. In a harmonic trap, the confinement contribution becomes a constant and hence independent of the particle positions. The result can then be expressed in a more compact form as

$$\sum_{i=1}^{3N} \left(\frac{\omega_i^s}{\omega_0} \right)^2 = 3N + 2\,(\kappa a)^2 \frac{E_{\mathrm{int}}^s}{q^2/a}. \tag{6.9}$$

The Coulomb case [121] is recovered upon taking the limit $\kappa \to 0$, see Ref. [154] for a wider class of power-law potentials. It is a remarkable special case since its frequency sum is independent of the stationary state used to evaluate the Hessian. For Yukawa interaction, E_{int}^s must be taken into account, which does depend on the particle configuration, e.g., the number of shells or the particular arrangement of the particles within a shell (fine structure) [73–75]. It should be noted that in a different trap, this would also apply to Coulomb systems due to the confinement term in Eq. (6.8), see also Ref. [154]. Even though the harmonic confinement does not correspond to a homogeneous background for $\kappa > 0$, the above expression is similar in form to the equation for the Einstein frequency of a homogeneous Yukawa system [19, 155].

The sum rule (6.9) establishes a link between the static (interaction energy) and dynamic properties (eigenfrequencies) of confined Yukawa Balls.

6.3.2 Breathing Mode

The nature of the breathing mode has already been discussed in Sec. 5.3.5. Here, the results of the cold-fluid theory are used to identify the breathing mode among the $3N$ normal modes of the harmonic approximation. The frequencies are then compared with the results of the MD simulations.

Projection Method

Since the harmonic approximation becomes exact in the zero temperature limit (small particle displacements), there must be a connection between the MD simulations at high Γ,

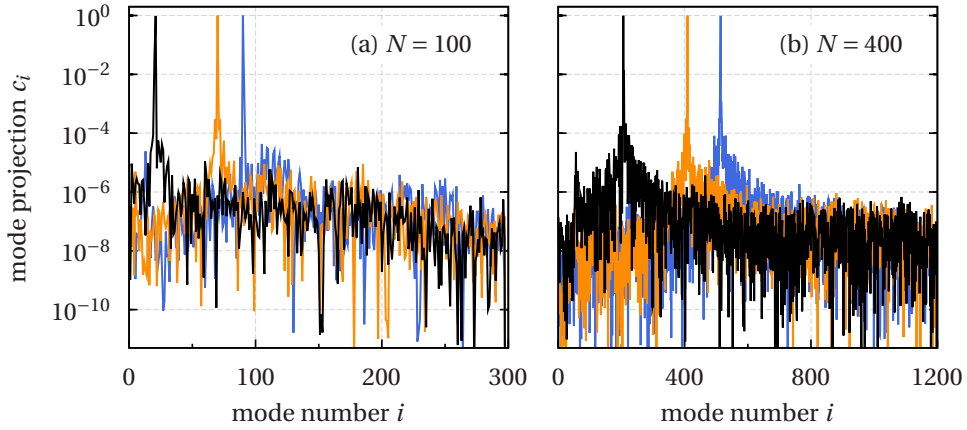

Figure 6.8: Projection of the $n = 1$ monopole mode ($\ell = m = 0$) of the cold-fluid theory on the $3N$ crystal eigenmodes. Results are shown for $\kappa a = 0.4, 1.2, 2$ (from left to right peak). The modes are ordered by their frequency (from high to low). From Ref. [135]. Copyright (2011) by the American Physical Society.

the cold-fluid approximation as a zero temperature theory, and the exact normal modes. The theoretical displacements $(\boldsymbol{w}_i^s)$ of the $(n,\ell) = (1,0)$ fluid mode for the ith particle in a crystal can be obtained from Eq. (5.5b) as $\boldsymbol{w}_i^s = \hat{\boldsymbol{u}}_1(\boldsymbol{r}_i^s) \sim (f_0^{\text{in}})'(r_i^s, \omega_{10})\hat{\boldsymbol{e}}_r$, where $\hat{\boldsymbol{e}}_r$ denotes the unit vector in the radial direction. This allows one to reconstruct the eigenvector of the fluid breathing mode for a particular state s from the derivative of the radial fluid eigenfunction $f_0^{\text{in}}(r,\omega_{10})$ at the equilibrium positions, see Eq. (5.31). The full $3N$-dimensional eigenvector then reads $\boldsymbol{w}_s^N = (\boldsymbol{w}_1^s, \ldots, \boldsymbol{w}_N^s)$, and is fully analogous to the exact (normalized) eigenvectors $\{\boldsymbol{v}_i^s\}$ from the Hessian. The breathing mode is identified as the mode with the greatest projection,

$$c_i^s = \left(\frac{\boldsymbol{w}_s^N}{|\boldsymbol{w}_s^N|} \cdot \boldsymbol{v}_i^s \right)^2 , \tag{6.10}$$

on the theoretical mode [82, 121], where $i \in \{1, \ldots, 3N\}$ and $0 \leq c_i^s \leq 1$.

Stationary states are obtained from separate MD runs, where the particles are slowly cooled until they settle into their equilibrium positions [71, 73]. Here, this procedure is repeated 200 times with random initial conditions for all parameter sets $(N, \kappa a)$, and the lowest energy state is chosen to calculate the normal modes from the Hessian.[4]

The outcome of the projection method is shown in Fig. 6.8. While the majority of modes have a negligible projection on the fluid mode, there exists a single mode with a significantly greater projection, which can be identified as the breathing mode. For Coulomb interaction, the breathing mode is the excitation with the highest frequency [121]. For $\kappa > 0$, however, the cold-fluid theory predicts that additional modes appear upon increase of the plasma parameter $\xi = \kappa R$ with $\omega > \omega_{\text{br}}$. This corresponds to an increase of either κa

[4] The numerical computation of the normal modes is based on a Mathematica notebook created by Dr. Christian Henning.

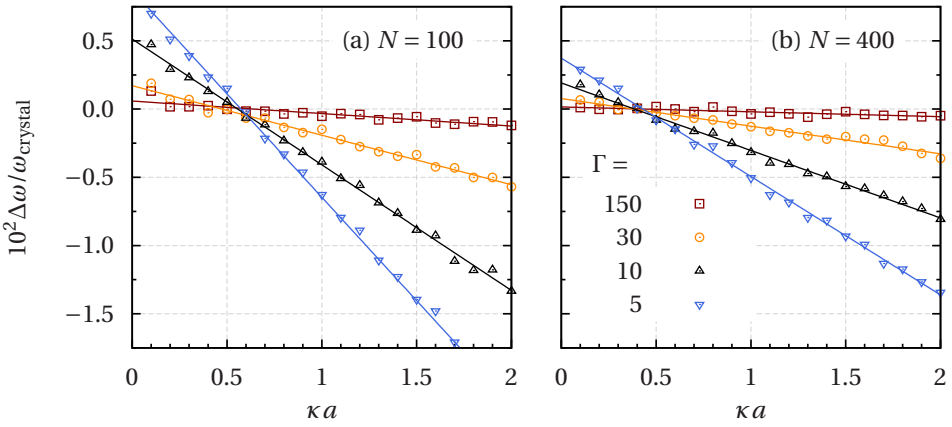

Figure 6.9: Deviation of the $n = 1$ monopole mode (MD) from the frequency of the exact eigenmode with the greatest projection on the fluid mode for (a) $N = 100$ and (b) $N = 400$ at $\Gamma = 5, 10, 30, 150$. The solid lines show a linear fit. From Ref. [135]. Copyright (2011) by the American Physical Society.

or the particle number N. Qualitatively, this trend can be observed in Fig. 6.8, where the maximum projection for $\kappa a = 0.4$ is found at high frequencies, whereas it shifts to intermediate frequencies for $\kappa a = 1.2$ and $\kappa a = 2$. The same observation was made in Ref. [74] upon increase of the particle number at fixed screening.

Coupling Dependence

In comparison with those of other modes, the breathing mode peaks in the MD spectra are very narrow and well pronounced (see Figs. 6.2 and 6.4), and therefore allow for a detailed study of their coupling dependence. The relative deviation $\Delta\omega/\omega_{\mathrm{crystal}} = (\omega_{\mathrm{MD}} - \omega_{\mathrm{crystal}})/\omega_{\mathrm{crystal}}$ of the finite temperature MD result from the zero temperature frequency of the harmonic approximation is depicted in Fig. 6.9. Even at a relatively weak coupling of $\Gamma = 5$, the largest deviations are only on the order of 2%. The agreement becomes better at higher Γ, and the results agree almost identically within the accuracy of the simulation at $\Gamma = 150$. For a fixed coupling parameter, the screening dependence is approximately linear.

The deviations clearly arise from the finite temperature in the simulation. The harmonic approximation relies on the existence of a crystallized state from which the modes are excited. These conditions are only satisfied at high Γ, when the particles are essentially located at their equilibrium positions and perform small amplitude oscillations. At weaker coupling the displacements become larger, and a second order expansion of the potential energy for a single state is no longer sufficient. Due to the large number of energetically adjacent metastable states, the system may also undergo structural transitions during an oscillation. This could be connected with a variation of the shell occupation numbers or a rearrangement of the local order within a shell and is inherently linked to the melting process [156]. Even in the very strong coupling limit, deviations from the harmonic approxi-

mation can occur because it is not clear which particular state is excited in the simulation. Therefore, the frequencies of a few stationary states have been compared. Typically, the differences are on the order $\Delta\Omega \sim 10^{-4}$ and thus significantly smaller those caused by the finite temperature.

Qualitatively, the temperature dependence changes as soon as the screening parameter exceeds a critical value. Figure 6.9 shows that at low screening (i.e., $\kappa a \lesssim 0.6$ and $\kappa a \lesssim 0.4$ for $N = 100$ and $N = 400$, respectively) the frequency decreases with Γ, which was also observed by Dubin and Schiffer for Coulomb interaction [121]. Above the critical value the behavior changes, and the breathing frequency increases. In the close vicinity of the critical screening parameter, however, it is almost independent of the temperature.

A very similar observation was made by Olivetti *et al.* [14, 139] for the breathing frequency of particles with homogeneous forces [i.e., $\boldsymbol{F}(\lambda\boldsymbol{r}, \lambda\boldsymbol{r}') = \lambda^{-k}\boldsymbol{F}(\boldsymbol{r}, \boldsymbol{r}')$] in a harmonic trap. Based on a scaling ansatz, they derived an equation that predicts an increase (decrease) of the breathing frequency with the coupling strength for short- (long-) ranged forces (in three-dimensional systems). In particular, it was noted in Ref. [139] that even though the Yukawa potential does not strictly belong to this class of potentials, it can be represented by a long-ranged Coulomb potential ($k = 2$) in weakly screened systems and a short-ranged Dirac delta potential ($k = 4$), when the Debye length far exceeds the system size. For a genuine Yukawa potential, however, there is a smooth transition between these two extreme cases, as demonstrated in Fig. 6.9, cf. also the corresponding discussion in Ch. 5. Their theory further predicts a temperature independent frequency for $k = 3$, which resembles the present results for the small intermediate screening interval.

The plasma parameter $\xi = \kappa R$ can be employed to quantify the results, since it relates the extension of the plasma to the interaction range. The value of ξ at which the temperature dependence in Fig. 6.9 changes is almost identical for the two particle numbers ($\xi \approx 2.3$ and $\xi \approx 2.4$ for $N = 100$ and $N = 400$, respectively). This indicates that ξ might play a similar role in determining the temperature dependence in Yukawa systems as the exponent k in systems with homogeneous forces.

Comparison with Cold-Fluid Theory

The previous analysis has shown that the results of the MD simulations approach those of the harmonic approximation in the strong coupling limit. Since the cold-fluid theory also completely neglects effects of a finite temperature, the harmonic approximation is ideally suited to assess its validity. First, it allows for a determination of the breathing frequency with high accuracy, and, second, the infinite coupling assumption is already "built-in". This makes it easier to identify the reasons for the observed deviations.

Figure 6.10 shows the relative deviation $\Delta\omega/\omega_{\text{crystal}} = (\omega_{\text{fluid}} - \omega_{\text{crystal}})/\omega_{\text{crystal}}$ of the cold-fluid result from the harmonic approximation. In the Coulomb limit, a universal uniform breathing mode exists in both the harmonic approximation [13] and the cold-fluid theory [121]—with identical frequencies. However, the $\xi \to 0$ limit of the Yukawa breathing mode does not describe a uniform oscillation, see Sec. 5.3.5. Even though this form of the radial eigenfunction is used to identify the breathing mode, it chooses the same mode as

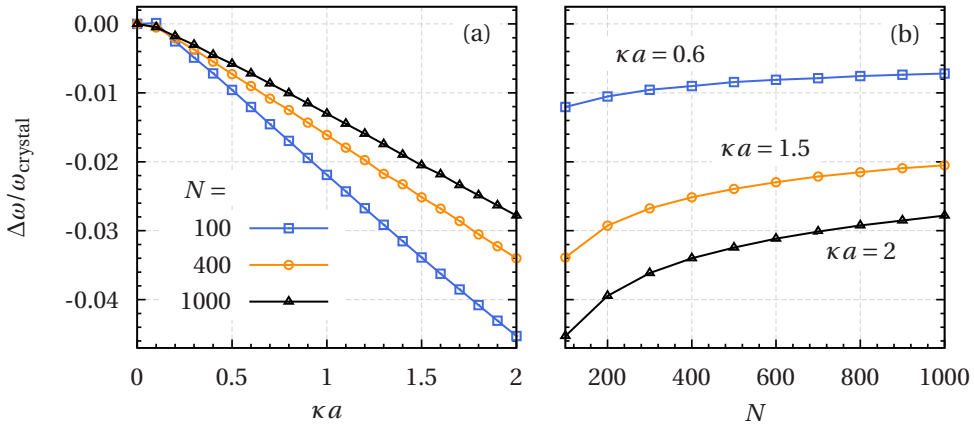

Figure 6.10: Frequency deviation of the exact eigenmode with the greatest projection on the fluid mode from the results of the cold-fluid theory as a function of (a) screening and (b) number of particles. From Ref. [135]. Copyright (2011) by the American Physical Society.

uniform displacements, i.e., $\boldsymbol{w}_i^s = \boldsymbol{r}_i^s$.[5] This behavior is also found for $\kappa > 0$ and shows that the actual deviations between the two mode forms are rather small. They vanish in the limit $\xi \to \infty$, because the cold-fluid mode becomes uniform as well. A comparison of the projections (6.10) for uniform and non-uniform displacements shows that the coefficients are consistently greater in the latter case, i.e., the Yukawa breathing mode is indeed better described by non-uniform displacements. The differences are small, though.

While the results coincide in the Coulomb limit, the fluid model underestimates the frequencies for Yukawa interaction. The deviations grow linearly with κa [Fig. 6.10(a)] and decrease with the particle number [Fig. 6.10(b)]. Since finite temperature effects can be excluded, the discrepancies must be due to the neglect of correlations in the fluid model. The analysis of Sheridan [120] shows indeed that taking a finite particle separation into account gives rise to an increase of the breathing frequency.

6.4 Summary

In this chapter, the normal modes of a confined Yukawa plasma have been investigated by three independent methods: molecular dynamics simulations, the harmonic approximation, and the cold-fluid theory presented in Ch. 5. The analysis shows that—despite its limitations—the cold-fluid theory is capable of accurately reproducing the mode spectra of a molecular dynamics simulation. However, its range of applicability must be kept in mind when comparisons are made: It is limited to low-order modes and weak to moderate screening—depending on the system size.

Specifically, the MD simulations confirm the existence of the high-order modes predicted by the cold-fluid theory. The lowest modes with $n = 0, 1$ show good agreement with

[5] There is one exception for $N = 100$ and $\kappa a = 0.1$.

the theory but increasingly deviate from its predictions at strong screening. The frequencies of the modes with $n \geq 2$ are generally shifted upward with respect to the theoretical result, and the critical screening parameters for their existence are predicted too large. In addition, the MD simulations reveal that these modes reappear at lower screening parameters. A sole feature of the simulations is the existence of a low frequency excitation in the $\ell = 1,2,3$ spectra at strong coupling conditions, which is not predicted by the simple mean-field theory.

Based on the harmonic approximation of the potential energy, a frequency sum rule has been derived that relates the mean squared eigenfrequency to the interaction energy. The analysis of the breathing mode shows that its temperature dependence is determined by the screening parameter. A decrease of the frequency with the coupling parameter at low κa turns into an increase at high screening, interrupted by a small screening interval with almost no temperature dependence. The generally weak coupling dependence of the eigenfrequencies identifies the neglect of correlation effects as the main source of error in the cold-fluid theory at high screening parameters.

This observation and the properties of the low frequency mode call for an improved theory that systematically incorporates correlation effects. However, this is beyond the scope of this work.

Related Journal Publication

- H. Kählert and M. Bonitz, *Collective excitations of a spherically confined Yukawa plasma*, Phys. Rev. E **83**, 056401 (2011)

CHAPTER 7

Conclusions

This work was concerned with two primary topics of interest: (i) the dynamic formation of the shell structure and (ii) the collective modes in a strongly coupled confined Yukawa plasma.

Shell Formation Dynamics

The correlation buildup and the order of shell formation (based on the examination of radial density profiles) were first analyzed for confinement conditions relevant to Yukawa Ball experiments. Langevin dynamics simulations of a simple cooling process revealed that shells first emerge at the plasma boundary. At the same time, the plasma performs a breathing oscillation. The time for the formation of the inner shells was shown to depend on the screening parameter. At sufficiently strong screening, the inner and outer shells were found to appear almost simultaneously.

In order to clarify the influence of the confinement potential and the mean density profile on the order of shell formation, equilibrium Monte Carlo simulations were performed. The analysis for quartic and linear potentials showed that the general trend of inward shell formation can hardly be reversed by changing the average density distribution in the trap. Simulations for a shifted harmonic potential with a blocked core then revealed that the formation of density modulations can indeed be triggered in the inner part of the plasma. While this feature is rather weak in Coulomb systems, it becomes more pronounced for Yukawa interaction. In the latter case, inward and outward shell formation occur simultaneously upon increase of the coupling parameter.

With the recent availability of sophisticated particle tracking and laser heating techniques, it should now be possible to test the simulation results in experiments.

Collective Modes

The collective excitations of strongly coupled Yukawa Balls were studied by a combination of analytic theory and numerical simulation. A continuum theory based on the cold-fluid

equations was presented that reveals a rich excitation spectrum for these plasmas. Contrary to other theories, it is not restricted to the breathing (lowest monopole) mode [14, 120], but yields all other modes (dipole, quadrupole, etc.) as well. They are characterized by two angular and a radial mode number. Their frequencies were shown to depend solely on ξ—the ratio of the plasma size and the screening length. Existing results in the literature for harmonically trapped particles with Coulomb [115, 132] and Dirac delta interaction [138] were recovered in the limits $\xi \to 0$ and $\xi \to \infty$, respectively. This shows that applications of the theory are not restricted to dusty plasmas. The fluid theory further yields an explicit result for the deviation of the lowest monopole mode from a uniform breathing mode [13].

Molecular dynamics simulations were performed to obtain the full excitation spectrum of Yukawa Balls and to test the theoretical predictions. It was found that the fluid theory properly describes the low-order eigenmodes but fails to reproduce the frequencies and existence conditions of the high-order excitations. In general, the accuracy of the theory decreases at large screening parameters. In addition to the cold-fluid modes, the MD simulations uncovered low frequency excitations in strongly coupled Yukawa Balls that could not be explained by the simple mean-field theory. The breathing mode was then chosen for a more detailed analysis and a comparison with the exact crystal eigenmodes. In particular, the temperature dependence of its frequency was found to change with a variation of the screening parameter. While it decreases as a function of the coupling parameter at low screening, it increases at larger screening parameters. In between these limits, a small interval was identified where it is practically independent of the temperature—in qualitative agreement with the theory of Olivetti *et al.* [14] for homogeneous forces.

Langevin dynamics simulations with a finite damping rate showed that the low frequency excitations and the high-order modes are most severely affected by friction. The low-order modes ($n = 0, 1$), on the other hand, are rather stable and should thus be detectable in Yukawa Ball experiments. Since these modes are properly described by the cold-fluid theory, a direct comparison should (in principle) be possible. However, one drawback of the theory is the neglect of wake effects observed in recent low pressure (i.e., low damping) Yukawa Ball experiments [52, 53], which might limit its applicability to these conditions. Nevertheless, an intermediate pressure regime might exist, where the dust-neutral friction is sufficiently low, and ion wake effects are negligible at the same time.

Another shortcoming of the cold-fluid theory is the neglect of thermal and (more importantly) correlation effects. This affects the results both quantitatively and qualitatively. First, the MD simulations showed that the eigenmode frequencies deviate from the theory, which was found to be mainly due to missing correlations, while thermal effects are rather weak. Second, the mean-field approach is generally unable to describe torsional (shear) modes [121], which could be the origin of the low frequency peaks in the MD spectra at strong coupling.

The inclusion of correlation effects in the theory can be achieved by several different means. For the analysis of the breathing mode, Sheridan [120] introduced a finite particle separation, while Olivetti *et al.* [14] used an approach based on the first (formally exact) equation of the BBGKY hierarchy. Dubin [115] accounted for correlations in a Coulomb system by using finite bulk and shear moduli. A general theory that describes arbitrary

modes in non-uniform systems with different interaction potentials is still missing. The BBGKY hierarchy represents the natural starting point for the derivation of such a theory. The difficulty, however, lies in finding an appropriate representation for the correlation function. For strongly coupled systems, the quasi-localized charge approximation of Kalman and Golden [101] provides a general framework for the calculation of the dispersion relation of uniform systems with various interaction forces [92]. The application of these ideas and concepts to non-uniform systems in traps is subject of ongoing work. First results for inhomogeneous bilayers have been obtained by Lee and Kalman [157].

Appendix

This Appendix presents the mathematical details for the calculation of the ground state potential and the eigenfrequency spectrum of the cold-fluid theory discussed in Ch. 5.[1]

Calculation of Ground State Potential

The result of the angular integration in Eq. (5.15) is [76]

$$\phi_0(r) = 2\pi \frac{q}{\kappa r} \int_0^R n_0(r')\, r' \left[e^{-\kappa|r-r'|} - e^{-\kappa(r+r')} \right] dr'.$$

Since the density is composed of a constant and a quadratic term, the problem now reduces to finding the solutions of the integrals

$$\mathscr{I}_n^{\gtrless} = \int_0^R (r')^n \left[e^{-\kappa|r-r'|} - e^{-\kappa(r+r')} \right] dr',$$

for $n = 1$ and $n = 3$.

Outside the plasma region ($r > R$), the calculation is simplified as $|r - r'| = r - r'$ for the entire integration volume. This yields

$$\begin{aligned} \mathscr{I}_n^{>} &= e^{-\kappa r} \int_0^R (r')^n \left[e^{\kappa r'} - e^{-\kappa r'} \right] dr' \\ &= 2\,\frac{e^{-\kappa r}}{\kappa^4} \begin{cases} [\xi\cosh(\xi) - \sinh(\xi)]\kappa^2, & n = 1, \\ \xi(\xi^2+6)\cosh(\xi) - 3(\xi^2+2)\sinh(\xi), & n = 3. \end{cases} \end{aligned}$$

On the other hand, inside the plasma ($r < R$), certain care must be taken in order to properly evaluate $|r - r'|$. Dividing the integration interval $[0 : R]$ into the two sub-intervals $[0 : r]$ and $(r : R]$, one obtains

$$\begin{aligned} \mathscr{I}_n^{<} &= \mathscr{I}_n^{>}(\xi \to \kappa r) + \int_r^R (r')^n \left[e^{-\kappa(r'-r)} - e^{-\kappa(r+r')} \right] dr' \\ &= \mathscr{I}_n^{>}(\xi \to \kappa r) + 2\sinh(\kappa r) \int_r^R (r')^n e^{-\kappa r'}\, dr'. \end{aligned}$$

[1] This analysis is an extended version of the appendix in Ref. [131].

The explicit result for the remaining integral is rather lengthy. The ground state potential, Eq. (5.15), then follows from the previous results and the explicit form of the density profile, Eq. (5.9). An alternative path to the potential inside the plasma is provided by Eqs. (7) and (10) in Ref. [76].

Series Expansions for Eigenfrequencies

The eigenfrequency spectrum $\Omega(\xi)$ follows from the roots of $\mathscr{D}(\Omega,\xi)$, see Eq. (5.37). In the following, the limits $\xi \ll 1$ and $\xi \gg 1$ are examined in detail, and the series expansions (5.38) and (5.41) are derived. This is achieved by writing the squared eigenfrequency as an expansion in the small parameters ξ and ξ^{-1}, respectively. The unknown coefficients are chosen such that $\mathscr{D}(\Omega,\xi) = 0$ is fulfilled to lowest order.

Coulomb Limit

The ansatz $\Omega^2(\xi) \approx \bar{a} + \bar{b}\xi + \bar{c}\xi^2$ for the squared eigenfrequency leads to the following result for the dielectric function (5.21),

$$\epsilon(\xi,\Omega) \approx 1 - \frac{3}{\bar{a}} + \left(\frac{3\bar{b}}{\bar{a}^2}\right)\xi + \left(\frac{3\bar{a}\bar{c} - 3\bar{b}^2 - \bar{a}^2}{\bar{a}^3}\right)\xi^2.$$

Series expansions for the term involving the Bessel function $k_\ell(x)$ can be obtained from the corresponding expansion for $K_{\ell+1/2}(x)$ [142, 144],

$$k_\ell(x) = \sqrt{\frac{2}{\pi x}} K_{\ell+1/2}(x) \propto \frac{1}{x^{\ell+1}}\left[1 + \frac{x^2}{2-4\ell} + \ldots\right], \qquad x \ll 1,\ \ell > 0.$$

This leads to $-\xi\, k_\ell'(\xi)/k_\ell(\xi) \approx (\ell+1) + \xi^2/(2\ell-1)$ for $\ell > 0$. In the particular case $\ell = 0$, the exact result is $-\xi\, k_0'(\xi)/k_0(\xi) = 1 + \xi$.

For an approximation of the hypergeometric function one can employ Eq. (5.32). Together with $x_s^2 \approx 6 - 2\bar{a}$, one obtains (for $\bar{a} \neq 3$),

$${}_2F_1\left(\frac{\alpha_\ell - \delta_\ell}{2}, \frac{\alpha_\ell + \delta_\ell}{2}; \alpha_\ell; \frac{\xi^2}{x_s^2}\right) \approx 1 + \left(\frac{\bar{a} - \ell}{\bar{a} - 3}\right)\frac{\xi^2}{6 + 4\ell}.$$

The second hypergeometric function in Eq. (5.37) with shifted parameters can be approximated by unity. The expansion coefficients $\bar{a}, \bar{b}$, and $\bar{c}$ for the surface modes given in Eq. (5.38) then follow by equating the ξ^0, ξ^1, and ξ^2 terms in Eq. (5.37) to zero.

For the bulk modes, the approach is slightly different. Here, $\bar{a} = 3$ and the above expansion for the hypergeometric functions cannot be used. A linear term in the expansion of the squared eigenfrequency fails because it would leave a constant term in Eq. (5.37). Employing a quadratic expansion, $\Omega^2(\xi) \approx 3 + \bar{c}\,\xi^2$, one obtains $\xi^2/x_s^2 \approx 1/(3 - 2\bar{c})$. In this case, the lowest-order term in Eq. (5.37) vanishes provided

$${}_2F_1\left(\frac{\alpha_\ell - \delta_\ell}{2}, \frac{\alpha_\ell + \delta_\ell}{2}; \alpha_\ell; \frac{1}{3 - 2\bar{c}}\right)\bigg|_{\Omega^2=3} = 0.$$

For $\ell = 0,1,2$, a numerical solution of this equation yields the coefficients given below Eq. (5.39). They satisfy $\bar{c} < 1$ and are thus below the plasma frequency at the boundary, which has the expansion $\Omega_{\rm p}^2(\xi) \approx 3 + \xi^2$.

Macroscopic/Strong Screening Limit

For $\xi \gg 1$, the small expansion parameter is $y = \xi^{-1}$. Following the same procedure as in the previous section with $\Omega^2(y^{-1}) \approx \bar{a} + \bar{b}y + \bar{c}y^2$, the dielectric function becomes

$$\epsilon(y^{-1}, \Omega) \approx -\frac{1}{\bar{a}y} + \frac{\bar{a}(\bar{a}-2)+\bar{b}}{\bar{a}^2},$$

and $y^{-2}/x_s^2 \approx 1 - 2y$. The Bessel function can be written as $k_\ell(x) = x^{-(\ell+1)}e^{-x}p_\ell(x)$, where $p_\ell(x)$ is a polynomial of order ℓ [142, 143]. For the associated term in Eq. (5.37), this implies

$$\frac{k_\ell'(x)}{k_\ell(x)} = \frac{d}{dx}\ln k_\ell(x) = \frac{p_\ell'(x)}{p_\ell(x)} - \frac{\ell+1}{x} - 1.$$

The leading-order contribution from the first term is $p_\ell'(x)/p_\ell(x) \approx \ell/x$ for $x \gg 1$. Consequently, the result is $-k_\ell(y^{-1})/k_\ell(y^{-1}) \approx 1 + y$.

The expansion for the hypergeometric function in the vicinity of $\xi^2/x_s^2 \lesssim 1$ is found from [142, 144]

$$\begin{aligned} {}_2F_1(a,b;a+b-m;z) = {} & \frac{(m-1)!\Gamma(a+b-m)}{\Gamma(a)\Gamma(b)}(1-z)^{-m} \\ & \times \sum_{k=0}^{m-1}\frac{(a-m)_k(b-m)_k(1-z)^k}{k!(1-m)_k} + \frac{(-1)^m\Gamma(a+b-m)}{\Gamma(a-m)\Gamma(b-m)} \\ & \times \sum_{k=0}^{\infty}\frac{(a)_k(b)_k}{k!(k+m)!}\big[-\ln(1-z)+\psi(k+1) \\ & +\psi(k+m+1)-\psi(a+k)-\psi(b+k)\big](1-z)^k, \end{aligned} \tag{A.1}$$

which can be used for $|z-1| < 1$ and $m \in \mathbb{N}^+$. $\psi(x)$ denotes the Digamma function. For $m = 0$, the finite sum must be omitted.

The series expansion (A.1) can now be applied to the two hypergeometric functions (HGF) in Eq. (5.37). In general, the parameters of the first HGF are $a = (\alpha_\ell - \delta_\ell)/2$, $b = (\alpha_\ell + \delta_\ell)/2$, and $c = \alpha_\ell$, see Eq. (5.30). In the second HGF, the parameters are shifted by an amount +1. In the following, they are abbreviated as ${}_2F_1[+0]$ and ${}_2F_1[+1]$, respectively.

With $\bar{a} = \Omega_{n\ell,\infty}^2$ [see Eq. (5.40)], the parameters of ${}_2F_1[+0]$ can be written as $a \approx -n - q(y)$ and $b \approx n + \alpha_\ell + q(y)$, where $q(y) \ll 1$. The main contribution to the second sum of the expansion is due to $\psi(a+k) \approx \psi(-n+k-q) \approx q^{-1}$ (for $k \le n$), which yields a constant term when combined with the prefactor $\Gamma^{-1}(a) \approx \Gamma^{-1}(-n-q) \approx (-1)^{n+1}n!\,q$ [144]. To lowest order in y, the HGF then reads

$${}_2F_1(-n-q, n+\alpha_\ell+q; \alpha_\ell; 1-2y) \approx \frac{(-1)^n}{(\alpha_\ell)_n}n!.$$

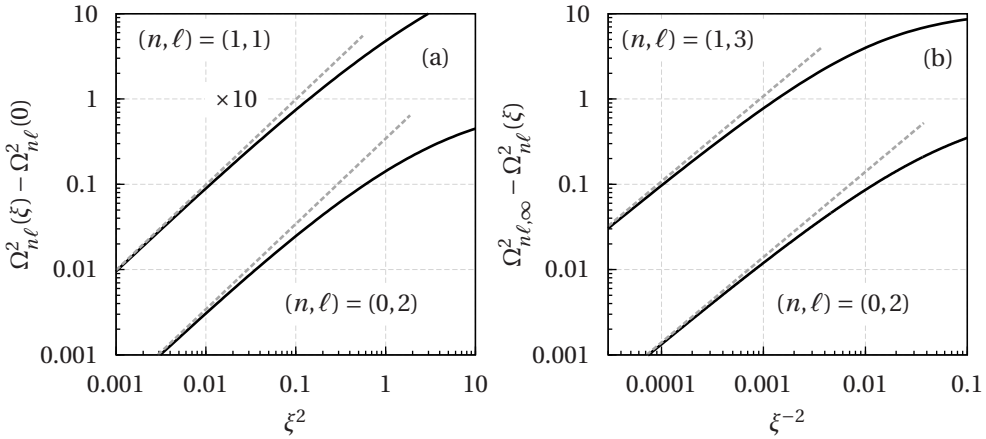

Figure A.1: Comparison of the numerical solution of Eq. (5.37) (solid lines) with the approximations (5.38), (5.39) and (5.41) (dashed lines) for (a) $\xi \ll 1$ and (b) $\xi \gg 1$. For a better presentation, the data in (a) for $(n,\ell) = (1,1)$ have been multiplied by a factor 10.

The expansion for ${}_2F_1[+1]$ can be obtained in a similar fashion from Eq. (A.1) with $m = 1$ and $q(y) \approx \bar{b}y/\chi$. This yields ($\chi = 4n + 2\alpha_\ell$)

$$ {}_2F_1(-n+1-q, n+1+\alpha_\ell+q; \alpha_\ell+1; 1-2y) \approx \alpha_\ell \frac{(-1)^n}{(\alpha_\ell)_n} n! \left[\frac{\bar{b}}{2\chi n(n+\alpha_\ell)} - 1\right]. $$

The $\mathcal{O}(y^{-1})$ term in Eq. (5.37) disappears provided $\bar{b} = 0$. For $n = 0$, the previous equation is not valid. Instead, ${}_2F_1[+1] \approx (2y)^{-1}$ must be used, and the leading-order term in Eq. (5.37) is $\mathcal{O}(y^{-2})$. It vanishes due to its prefactor $\sim (\ell - \bar{a})$, since $\bar{a} = \ell$ for $n = 0$. The $\mathcal{O}(y^{-1})$ term vanishes for $\bar{b} = 0$.

Since the coefficients for the $\mathcal{O}(y)$ terms of the squared eigenfrequency are equal to zero, the HGF must be evaluated up to first order in y to find the lowest-order correction to $\Omega^2(y)$ for $n = 1, 2, \ldots$. The small correction to the parameters of the HGF now reads $q(y) \approx \bar{c}y^2/\chi$, and one obtains

$$ {}_2F_1[+0] \approx \frac{(-1)^n}{(\alpha_\ell)_n} n! \left[1 - 2n(n+\alpha_\ell)y\right], $$
$$ {}_2F_1[+1] \approx \alpha_\ell \frac{(-1)^n}{(\alpha_\ell)_n} n! \left\{-1 + \left[(n-1)(n+\alpha_\ell+1) + \frac{\bar{c}}{2\chi n(n+\alpha_\ell)}\right] y\right\}. $$

Choosing the coefficient $\bar{c}$ such that terms $\mathcal{O}(y^0)$ in Eq. (5.37) vanish, Eqs. (5.41) and (5.42) follow for $n > 0$. If $n = 0$, the same procedure leads to $\bar{c} = -2\ell(\ell-1)(\ell+3/2)$, i.e., Eq. (5.42) also holds for $n = 0$ (here, $\ell \neq 0$).

For a comparison of the analytic solutions for the squared eigenfrequencies with a numerical evaluation of Eq. (5.37), see Fig. A.1.

Eigenfrequencies Near the Surface Plasma Frequency

In the following, the appearance of new modes for $\xi > \xi_{n\ell}^{\mathrm{crit}}$ will be exemplified by a numerical evaluation of the eigenvalue equation (5.37) combined with an analytic investigation of the limit $\Omega \to \Omega_{\mathrm{p}}(\xi)$. For this purpose, let $\xi \neq \xi_{n\ell}^{\mathrm{crit}}$ and thus $\Omega_{\mathrm{p}}(\xi) \neq \Omega_{n\ell}(\xi_{n\ell}^{\mathrm{crit}})$. The limits of the different terms in Eq. (5.37) will now be considered separately.

Writing the eigenfrequency as $\Omega^2 \approx \Omega_{\mathrm{p}}^2(\xi) - \Delta$, where $0 < \Delta \ll \Omega_{\mathrm{p}}^2(\xi)$, the dielectric function becomes $\epsilon(\xi,\Omega) \approx -\Delta/\Omega_{\mathrm{p}}^2(\xi)$. For the hypergeometric function with shifted parameters, one can use ${}_2F_1(c-a,c-b;c;z) = (1-z)^{a+b-c}\,{}_2F_1(a,b;c;z)$ [142, 144] with $c = a+b+1$ to obtain

$$ {}_2F_1(a+1,b+1,a+b+1,z) = \frac{1}{1-z}\,{}_2F_1(a,b,a+b+1,z). $$

While $(1-z)^{-1}$ diverges as $z \to 1$, the hypergeometric function on the right-hand side remains finite. Using $(1-z)^{-1} \approx \xi^2/(2\Delta)$ and the identity [142, 144]

$$ {}_2F_1(a,b,a+b+1,1) = \frac{\Gamma(a+b+1)\Gamma(1)}{\Gamma(a+1)\Gamma(b+1)}, $$

it follows that the third term in Eq. (5.37) has the limit

$$ \begin{aligned} &\lim_{\Delta\to 0} \epsilon(\xi,\Omega)\frac{\ell-\Omega^2}{\alpha_\ell}\frac{\xi^2}{x_s^2}\,{}_2F_1\left(\frac{\alpha_\ell-\delta_\ell}{2}+1,\frac{\alpha_\ell+\delta_\ell}{2}+1;\alpha_\ell+1;\frac{\xi^2}{x_s^2}\right) \\ &\quad = \frac{\xi^2}{2\alpha_\ell}\left[1-\frac{\ell}{\Omega_{\mathrm{p}}^2(\xi)}\right]\frac{\Gamma(\alpha_\ell+1)}{\Gamma\left(\frac{\alpha_\ell-\delta_\ell}{2}+1\right)\Gamma\left(\frac{\alpha_\ell+\delta_\ell}{2}+1\right)}. \end{aligned} \tag{A.2} $$

Here, it is understood that δ_ℓ must be evaluated at $\Omega^2 = \Omega_{\mathrm{p}}^2(\xi)$.

For the first and second term in Eq. (5.37), one can use the zeroth-order ($k = 0$) contribution in the expansion (A.1) (for $m = 0$) to obtain

$$ \begin{aligned} {}_2F_1\left(\frac{\alpha_\ell-\delta_\ell}{2},\frac{\alpha_\ell+\delta_\ell}{2};\alpha_\ell;\frac{\xi^2}{x_s^2}\right) \approx \frac{\Gamma(\alpha_\ell)}{\Gamma\left(\frac{\alpha_\ell-\delta_\ell}{2}\right)\Gamma\left(\frac{\alpha_\ell+\delta_\ell}{2}\right)}\Bigg[&-\ln\left(\frac{2\Delta}{\xi^2}\right) \\ &+2\psi(1)-\psi\left(\frac{\alpha_\ell-\delta_\ell}{2}\right)-\psi\left(\frac{\alpha_\ell+\delta_\ell}{2}\right)\Bigg]. \end{aligned} $$

Again, δ_ℓ must be calculated at $\Omega^2 = \Omega_{\mathrm{p}}^2(\xi)$. Combining this expression with the previous result for the dielectric function yields an approximation for $\mathscr{D}(\Omega,\xi)$ in the vicinity of $\Omega_{\mathrm{p}}(\xi)$ accurate to $\mathscr{O}(\Delta^0)$:

$$ \begin{aligned} \mathscr{D}(\Omega,\xi) \approx \frac{\xi\,\Gamma(\alpha_\ell)}{\Gamma\left(\frac{\alpha_\ell-\delta_\ell}{2}\right)\Gamma\left(\frac{\alpha_\ell+\delta_\ell}{2}\right)}\frac{k_\ell'(\xi)}{k_\ell(\xi)}\Bigg[&\ln\left(\frac{2\Delta}{\xi^2}\right)-2\psi(1)+\psi\left(\frac{\alpha_\ell-\delta_\ell}{2}\right) \\ &+\psi\left(\frac{\alpha_\ell+\delta_\ell}{2}\right)\Bigg]+\frac{\xi^2}{2\alpha_\ell}\left[1-\frac{\ell}{\Omega_{\mathrm{p}}^2(\xi)}\right]\frac{\Gamma(\alpha_\ell+1)}{\Gamma\left(\frac{\alpha_\ell-\delta_\ell}{2}+1\right)\Gamma\left(\frac{\alpha_\ell+\delta_\ell}{2}+1\right)}. \end{aligned} \tag{A.3} $$

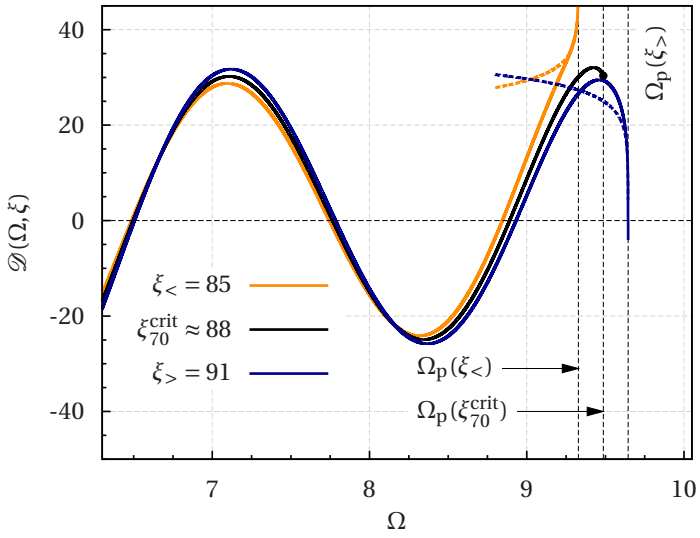

Figure A.2: Plot of the eigenvalue function $\mathscr{D}(\Omega,\xi)$ [Eq. (5.37)] for the monopole modes as a function of Ω for different ξ's close to the critical parameter $\xi_{70}^{\rm crit}$. The dashed lines show the asymptotic limit given by Eq. (A.3).

The contribution from the dielectric function is neglected since it is $\mathscr{O}(\Delta\ln[2\Delta/\xi^2])$. Equation (A.3) shows that $\mathscr{D}(\xi,\Omega)$ diverges logarithmically as $\Delta\to 0$ if $\xi\neq\xi_{n\ell}^{\rm crit}$.

Being among the prefactors for the logarithmic term in Eq. (A.3), the asymptotic limit crucially depends on the sign of the Gamma function with the argument $(\alpha_\ell-\delta_\ell)/2$. An increase of ξ from $\xi<\xi_{n\ell}^{\rm crit}$ to $\xi>\xi_{n\ell}^{\rm crit}$ shifts the plasma frequency upward such that $\Omega_{n\ell}(\xi_{n\ell}^{\rm crit})$ is within the allowed range of frequencies below the plasma frequency. This is accompanied by a sign change of the Gamma function as $\Omega_{\rm p}(\xi)$ exceeds $\Omega_{\rm p}(\xi_{n\ell}^{\rm crit})=\Omega_{n\ell}(\xi_{n\ell}^{\rm crit})$, which also reverses the sign of the asymptotic limit. The result is a zero crossing of $\mathscr{D}(\Omega,\xi)$ and the appearance of a new mode.

Figure A.2 illustrates the behavior of $\mathscr{D}(\Omega,\xi)$ in the vicinity of the surface plasma frequency. As ξ is increased from a value $\xi_<=85<\xi_{70}^{\rm crit}$ to a value above the critical parameter, $\xi_>=91>\xi_{70}^{\rm crit}$, the divergent limit changes from $+\infty$ to $-\infty$, and a new root of $\mathscr{D}(\Omega,\xi)$ emerges. This is in accordance with the behavior of Eq. (A.3), cf. the dashed lines. Since it is very difficult to determine the new roots numerically in the close vicinity of the surface plasma frequency for $\xi\gtrsim\xi_{n\ell}^{\rm crit}$, they are approximated by $\Omega_{\rm p}(\xi)$.

Bibliography

[1] O. Arp, D. Block, A. Piel, and A. Melzer, *Dust Coulomb Balls: Three-Dimensional Plasma Crystals*, Phys. Rev. Lett. **93**, 165004 (2004)

[2] A. Melzer, B. Buttenschön, T. Miksch, M. Passvogel, D. Block, O. Arp, and A. Piel, *Finite dust clusters in dusty plasmas*, Plasma Phys. Control. Fusion **52**, 124028 (2010)

[3] O. Arp, D. Block, M. Klindworth, and A. Piel, *Confinement of Coulomb balls*, Phys. Plasmas **12**, 122102 (2005)

[4] S. L. Gilbert, J. J. Bollinger, and D. J. Wineland, *Shell-Structure Phase of Magnetically Confined Strongly Coupled Plasmas*, Phys. Rev. Lett. **60**, 2022 (1988)

[5] D. H. E. Dubin and T. M. O'Neil, *Trapped nonneutral plasmas, liquids, and crystals (the thermal equilibrium states)*, Rev. Mod. Phys. **71**, 87 (1999)

[6] T. Pohl, T. Pattard, and J. M. Rost, *Coulomb Crystallization in Expanding Laser-Cooled Neutral Plasmas*, Phys. Rev. Lett. **92**, 155003 (2004)

[7] T. Killian, *Ultracold neutral plasmas*, Science **316**, 705 (2007)

[8] H. Totsuji, T. Kishimoto, C. Totsuji, and K. Tsuruta, *Competition between Two Forms of Ordering in Finite Coulomb Clusters*, Phys. Rev. Lett. **88**, 125002 (2002)

[9] C. Henning, H. Kählert, P. Ludwig, A. Melzer, and M. Bonitz, *Spectral properties of spherically confined dusty plasma crystals*, J. Phys. A: Math. Theor. **42**, 214023 (2009)

[10] Y. Ivanov and A. Melzer, *Modes of three-dimensional dust crystals in dusty plasmas*, Phys. Rev. E **79**, 036402 (2009)

[11] M. Rosenberg and G. Kalman, *Dust acoustic waves in strongly coupled dusty plasmas*, Phys. Rev. E **56**, 7166 (1997)

[12] H. Ohta and S. Hamaguchi, *Wave Dispersion Relations in Yukawa Fluids*, Phys. Rev. Lett. **84**, 6026 (2000)

[13] C. Henning, K. Fujioka, P. Ludwig, A. Piel, A. Melzer, and M. Bonitz, *Existence and Vanishing of the Breathing Mode in Strongly Correlated Finite Systems*, Phys. Rev. Lett. **101**, 045002 (2008)

[14] A. Olivetti, J. Barré, B. Marcos, F. Bouchet, and R. Kaiser, *Breathing Mode for Systems of Interacting Particles*, Phys. Rev. Lett. **103**, 224301 (2009)

[15] S. Ichimaru, *Strongly coupled plasmas: high-density classical plasmas and degenerate electron liquids*, Rev. Mod. Phys. **54**, 1017 (1982)

[16] D. R. Nicholson, *Introduction to Plasma Theory* (Wiley, New York, 1983)

[17] M. Bonitz, P. Ludwig, H. Baumgartner, C. Henning, A. Filinov, D. Block, O. Arp, A. Piel, S. Käding, Y. Ivanov, A. Melzer, H. Fehske, and V. Filinov, *Classical and quantum Coulomb crystals*, Phys. Plasmas **15**, 055704 (2008)

[18] M. Bonitz, N. Horing, and P. Ludwig, eds., *Introduction to Complex Plasmas* (Springer, Berlin, 2010)

[19] Z. Donkó, G. J. Kalman, and P. Hartmann, *Dynamical correlations and collective excitations of Yukawa liquids*, J. Phys.: Condens. Matter **20**, 413101 (2008)

[20] J. P. Hansen, I. R. McDonald, and E. L. Pollock, *Statistical mechanics of dense ionized matter. III. Dynamical properties of the classical one-component plasma*, Phys. Rev. A **11**, 1025 (1975)

[21] K. I. Golden, G. Kalman, and P. Wyns, *Dielectric tensor and shear-mode dispersion for strongly coupled Coulomb liquids: Three-dimensional one-component plasmas*, Phys. Rev. A **46**, 3454 (1992)

[22] Z. Donkó and B. Nyíri, *Molecular dynamics calculation of the thermal conductivity and shear viscosity of the classical one-component plasma*, Phys. Plasmas **7**, 45 (2000)

[23] K. Y. Sanbonmatsu and M. S. Murillo, *Shear Viscosity of Strongly Coupled Yukawa Systems on Finite Length Scales*, Phys. Rev. Lett. **86**, 1215 (2001)

[24] L.-J. Hou, A. Piel, and P. K. Shukla, *Self-Diffusion in 2D Dusty-Plasma Liquids: Numerical-Simulation Results*, Phys. Rev. Lett. **102**, 085002 (2009)

[25] T. Ott and M. Bonitz, *Is Diffusion Anomalous in Two-Dimensional Yukawa Liquids?*, Phys. Rev. Lett. **103**, 195001 (2009)

[26] S. Hamaguchi, R. T. Farouki, and D. H. E. Dubin, *Triple point of Yukawa systems*, Phys. Rev. E **56**, 4671 (1997)

[27] W. M. Itano, J. J. Bollinger, J. N. Tan, B. Jelenković, X.-P. Huang, and D. J. Wineland, *Bragg Diffraction from Crystallized Ion Plasmas*, Science **279**, 686 (1998)

[28] D. O. Gericke, K. Wünsch, A. Grinenko, and J. Vorberger, *Structural properties of warm dense matter*, J. Phys.: Conf. Ser. **220**, 012001 (2010)

[29] P. Ludwig, M. Bonitz, H. Kählert, and J. W. Dufty, *Dynamics of strongly correlated ions in a partially ionized quantum plasma*, J. Phys.: Conf. Ser. **220**, 012003 (2010)

[30] H. M. van Horn, *Dense Astrophysical Plasmas*, Science **252**, 384 (1991)

[31] S. H. Glenzer and R. Redmer, *X-ray Thomson scattering in high energy density plasmas*, Rev. Mod. Phys. **81**, 1625 (2009)

[32] K. Okada, M. Wada, T. Takayanagi, S. Ohtani, and H. A. Schuessler, *Characterization of ion Coulomb crystals in a linear Paul trap*, Phys. Rev. A **81**, 013420 (2010)

[33] T. C. Killian, S. Kulin, S. D. Bergeson, L. A. Orozco, C. Orzel, and S. L. Rolston, *Creation of an Ultracold Neutral Plasma*, Phys. Rev. Lett. **83**, 4776 (1999)

[34] Y. C. Chen, C. E. Simien, S. Laha, P. Gupta, Y. N. Martinez, P. G. Mickelson, S. B. Nagel, and T. C. Killian, *Electron Screening and Kinetic-Energy Oscillations in a Strongly Coupled Plasma*, Phys. Rev. Lett. **93**, 265003 (2004)

[35] J. Castro, P. McQuillen, and T. C. Killian, *Ion Acoustic Waves in Ultracold Neutral Plasmas*, Phys. Rev. Lett. **105**, 065004 (2010)

[36] M. Bonitz, C. Henning, and D. Block, *Complex plasmas: a laboratory for strong correlations*, Rep. Prog. Phys. **73**, 066501 (2010)

[37] J. Abrahamson and J. Dinniss, *Ball lightning caused by oxidation of nanoparticle networks from normal lightning strikes on soil*, Nature **403**, 519 (2000)

[38] G. S. Paiva, A. C. Pavão, E. Alpes de Vasconcelos, O. Mendes, and E. Felisberto da Silva, *Production of Ball-Lightning-Like Luminous Balls by Electrical Discharges in Silicon*, Phys. Rev. Lett. **98**, 048501 (2007)

[39] P. K. Shukla and B. Eliasson, *Colloquium: Fundamentals of dust-plasma interactions*, Rev. Mod. Phys. **81**, 25 (2009)

[40] O. Arp, *Coulomb balls—Structure and confinement of spherical dust crystals in a plasma*, Dissertation, Christian-Albrechts-Universität zu Kiel (2006)

[41] G. E. Morfill and A. V. Ivlev, *Complex plasmas: An interdisciplinary research field*, Rev. Mod. Phys. **81**, 1353 (2009)

[42] G. E. Morfill, A. V. Ivlev, P. Brandt, and H. Löwen, *Interdisciplinary research with complex plasmas*, AIP Conf. Proc. **1242**, 67 (2010)

[43] D. Block, *Experiments on Structural Formation in Plasmas*, Habilitation thesis, Christian-Albrechts-Universität zu Kiel (2007)

[44] C. Schmidt, O. Arp, and A. Piel, *Spatially extended void-free dusty plasmas in a laboratory radio-frequency discharge*, Phys. Plasmas **18**, 013704 (2011)

[45] O. Arp, D. Block, M. Bonitz, H. Fehske, V. Golubnychiy, S. Kosse, P. Ludwig, A. Melzer, and A. Piel, *3D Coulomb balls: experiment and simulation*, J. Phys.: Conf. Ser. **11**, 234 (2005)

[46] M. Bonitz, D. Block, O. Arp, V. Golubnychiy, H. Baumgartner, P. Ludwig, A. Piel, and A. Filinov, *Structural Properties of Screened Coulomb Balls*, Phys. Rev. Lett. **96**, 075001 (2006)

[47] D. Block, S. Käding, A. Melzer, A. Piel, H. Baumgartner, and M. Bonitz, *Experiments on metastable states of three-dimensional trapped particle clusters*, Phys. Plasmas **15**, 040701 (2008)

[48] S. Käding, D. Block, A. Melzer, A. Piel, H. Kählert, P. Ludwig, and M. Bonitz, *Shell transitions between metastable states of Yukawa balls*, Phys. Plasmas **15**, 073710 (2008)

[49] S. Käding and A. Melzer, *Three-dimensional stereoscopy of Yukawa (Coulomb) balls in dusty plasmas*, Phys. Plasmas **13**, 090701 (2006)

[50] M. Kroll, S. Harms, D. Block, and A. Piel, *Digital in-line holography of dusty plasmas*, Phys. Plasmas **15**, 063703 (2008)

[51] M. Kroll, L. Mühlfeld, and D. Block, *Stereoscopic Digital Holography*, IEEE Trans. Plasma Sci. **38**, 897 (2010)

[52] M. Kroll, J. Schablinski, D. Block, and A. Piel, *On the influence of wakefields on three-dimensional particle arrangements*, Phys. Plasmas **17**, 013702 (2010)

[53] C. Killer, A. Schella, T. Miksch, and A. Melzer, *Vertically elongated three-dimensional Yukawa clusters in dusty plasmas*, Phys. Rev. B **84**, 054104 (2011)

[54] M. Lampe, G. Joyce, and G. Ganguli, *Structure and Dynamics of Dust in Streaming Plasma: Dust molecules, Strings, and Crystals*, IEEE Trans. Plasma Sci. **33**, 57 (2005)

[55] A. F. Alexandrov, L. S. Bogdankevich, and A. A. Rukhadze, *Principles of Plasma Electrodynamics* (Springer, Berlin, 1984)

[56] M. Nambu, S. V. Vladimirov, and P. K. Shukla, *Attractive forces between charged particulates in plasmas*, Phys. Lett. A **203**, 40 (1995)

[57] O. Ishihara and S. V. Vladimirov, *Wake potential of a dust grain in a plasma with ion flow*, Phys. Plasmas **4**, 69 (1997)

[58] A. V. Ivlev, S. A. Khrapak, S. K. Zhdanov, G. E. Morfill, and G. Joyce, *Force on a Charged Test Particle in a Collisional Flowing Plasma*, Phys. Rev. Lett. **92**, 205007 (2004)

[59] F. Jenko, G. Joyce, and H. M. Thomas, *Dressed particle simulation of dusty plasmas*, Phys. Plasmas **12**, 022309 (2005)

[60] G. Joyce, M. Lampe, and G. Ganguli, *Instability-Triggered Phase Transition to a Dusty-Plasma Condensate*, Phys. Rev. Lett. **88**, 095006 (2002)

[61] K. Matyash, R. Schneider, R. Ikkurthi, L. Lewerentz, and A. Melzer, *P^3M simulations of dusty plasmas*, Plasma Phys. Control. Fusion **52**, 124016 (2010)

[62] J. B. Pieper, J. Goree, and R. A. Quinn, *Three-dimensional structure in a crystallized dusty plasma*, Phys. Rev. E **54**, 5636 (1996)

[63] M. Lampe, G. Joyce, G. Ganguli, and V. Gavrishchaka, *Interactions between dust grains in a dusty plasma*, Phys. Plasmas **7**, 3851 (2000)

[64] V. A. Schweigert, I. V. Schweigert, A. Melzer, A. Homann, and A. Piel, *Alignment and instability of dust crystals in plasmas*, Phys. Rev. E **54**, 4155 (1996)

[65] A. Melzer, V. A. Schweigert, I. V. Schweigert, A. Homann, S. Peters, and A. Piel, *Structure and stability of the plasma crystal*, Phys. Rev. E **54**, R46 (1996)

[66] P. K. Shukla and M. Salimullah, *The potential around a test charge in magnetized dusty plasmas*, Phys. Plasmas **3**, 3858 (1996)

[67] P. Shukla, M. Nambu, and M. Salimullah, *Effect of ion polarization drift on shielding and dynamical potentials in magnetized plasmas*, Phys. Lett. A **291**, 413 (2001)

[68] M. Salimullah, P. K. Shukla, M. Nambu, H. Nitta, O. Ishihara, and A. M. Rizwan, *Modification of the shielding and wake potentials in a streaming dusty magnetoplasma*, Phys. Plasmas **10**, 3047 (2003)

[69] R. W. Hasse and V. V. Avilov, *Structure and Madelung energy of spherical Coulomb crystals*, Phys. Rev. A **44**, 4506 (1991)

[70] J. P. Schiffer, *Melting of Crystalline Confined Plasmas*, Phys. Rev. Lett. **88**, 205003 (2002)

[71] H. Kählert, P. Ludwig, H. Baumgartner, M. Bonitz, D. Block, S. Käding, A. Melzer, and A. Piel, *Probability of metastable configurations in spherical three-dimensional Yukawa crystals*, Phys. Rev. E **78**, 036408 (2008)

[72] K. Tsuruta and S. Ichimaru, *Binding energy, microstructure, and shell model of Coulomb clusters*, Phys. Rev. A **48**, 1339 (1993)

[73] P. Ludwig, S. Kosse, and M. Bonitz, *Structure of spherical three-dimensional Coulomb crystals*, Phys. Rev. E **71**, 046403 (2005)

[74] S. W. S. Apolinario, B. Partoens, and F. M. Peeters, *Structural and dynamical aspects of small three-dimensional spherical Coulomb clusters*, New J. Phys. **9**, 283 (2007)

[75] H. Baumgartner, D. Asmus, V. Golubnychiy, P. Ludwig, H. Kählert, and M. Bonitz, *Ground states of finite spherical Yukawa crystals*, New J. Phys. **10**, 093019 (2008)

[76] C. Henning, H. Baumgartner, A. Piel, P. Ludwig, V. Golubnichiy, M. Bonitz, and D. Block, *Ground state of a confined Yukawa plasma*, Phys. Rev. E **74**, 056403 (2006)

[77] C. Henning, P. Ludwig, A. Filinov, A. Piel, and M. Bonitz, *Ground state of a confined Yukawa plasma including correlation effects*, Phys. Rev. E **76**, 036404 (2007)

[78] J. Cioslowski and E. Grzebielucha, *Screening-controlled morphologies of Yukawa crystals*, J. Chem. Phys. **132**, 024708 (2010)

[79] W. D. Kraeft and M. Bonitz, *Thermodynamics of a correlated confined plasma II. Mesoscopic system*, J. Phys.: Conf. Ser. **35**, 94 (2006)

[80] J. Cioslowski and E. Grzebielucha, *Parameter-free shell model of spherical Coulomb crystals*, Phys. Rev. E **78**, 026416 (2008)

[81] H. Baumgartner, H. Kählert, V. Golubnychiy, C. Henning, S. Käding, A. Melzer, and M. Bonitz, *Shell Structure of Yukawa Balls*, Contrib. Plasma Phys. **47**, 281 (2007)

[82] C. Henning, *Ground State and Excitation Properties of Yukawa Balls*, Dissertation, Christian-Albrechts-Universität zu Kiel (2009)

[83] J. Cioslowski and E. Grzebielucha, *Shell model of assemblies of equicharged particles subject to radial confining potentials*, J. Chem. Phys. **134**, 124305 (2011)

[84] S. W. S. Apolinario and F. M. Peeters, *Melting transitions in isotropically confined three-dimensional small Coulomb clusters*, Phys. Rev. E **76**, 031107 (2007)

[85] H. Baumgartner, *Structure and dynamics of Yukawa balls*, Dissertation, Christian-Albrechts-Universität zu Kiel (2009)

[86] H. Thomsen, *Excitation and Melting of Yukawa Balls*, Diploma thesis, Christian-Albrechts-Universität zu Kiel (2011)

[87] J. Wrighton, J. W. Dufty, H. Kählert, and M. Bonitz, *Theoretical description of Coulomb balls: Fluid phase*, Phys. Rev. E **80**, 066405 (2009)

[88] J. Wrighton, J. W. Dufty, M. Bonitz, and H. Kählert, *Shell Structure of Confined Charges at Strong Coupling*, Contrib. Plasma Phys. **50**, 26 (2010)

[89] H. Bruhn, *Thermodynamische Eigenschaften stark gekoppelter sphärischer Yukawa-systeme*, Diploma thesis, Christian-Albrechts-Universität zu Kiel (2011)

[90] H. Bruhn, H. Kählert, T. Ott, M. Bonitz, J. Wrighton, and J. W. Dufty, *Theoretical description of spherically confined, strongly correlated Yukawa plasmas*, Phys. Rev. E **84**, 046407 (2011)

[91] J. P. Hansen and I. R. McDonald, *Theory of Simple Liquids* (Elsevier Academic Press, London, 2006), 3rd ed.

[92] K. I. Golden and G. J. Kalman, *Quasilocalized charge approximation in strongly coupled plasma physics*, Phys. Plasmas **7**, 14 (2000)

[93] Z. Donkó, P. Hartmann, and G. J. Kalman, *Molecular dynamics simulations of strongly coupled plasmas: Localization and microscopic dynamics*, Phys. Plasmas **10**, 1563 (2003)

[94] K. S. Singwi, M. P. Tosi, R. H. Land, and A. Sjölander, *Electron Correlations at Metallic Densities*, Phys. Rev. **176**, 589 (1968)

[95] M. S. Murillo, *Static local field correction description of acoustic waves in strongly coupling dusty plasmas*, Phys. Plasmas **5**, 3116 (1998)

[96] A. Piel, *Plasma Physics: An Introduction to Laboratory, Space, and Fusion Plasmas* (Springer, Berlin, 2010), 1st ed.

[97] A. Piel and A. Melzer, *Dynamical processes in complex plasmas*, Plasma Phys. Control. Fusion **44**, R1 (2002)

[98] P. K. Kaw and A. Sen, *Low frequency modes in strongly coupled dusty plasmas*, Phys. Plasmas **5**, 3552 (1998)

[99] G. Kalman, M. Rosenberg, and H. E. DeWitt, *Collective Modes in Strongly Correlated Yukawa Liquids: Waves in Dusty Plasmas*, Phys. Rev. Lett. **84**, 6030 (2000)

[100] R. L. Merlino, A. Barkan, C. Thompson, and N. D'Angelo, *Laboratory studies of waves and instabilities in dusty plasmas*, Phys. Plasmas **5**, 1607 (1998)

[101] G. Kalman and K. I. Golden, *Response function and plasmon dispersion for strongly coupled Coulomb liquids*, Phys. Rev. A **41**, 5516 (1990)

[102] J. P. Hansen, *Statistical Mechanics of Dense Ionized Matter. I. Equilibrium Properties of the Classical One-Component Plasma*, Phys. Rev. A **8**, 3096 (1973)

[103] W. L. Slattery, G. D. Doolen, and H. E. DeWitt, *Improved equation of state for the classical one-component plasma*, Phys. Rev. A **21**, 2087 (1980)

[104] W. L. Slattery, G. D. Doolen, and H. E. DeWitt, *N dependence in the classical one-component plasma Monte Carlo calculations*, Phys. Rev. A **26**, 2255 (1982)

[105] M. Bonitz and D. Semkat, eds., *Introduction to Computational Methods in Many Body Physics* (Rinton Press, Princeton, 2006)

[106] H. Kählert, *First-principle simulation of classical charged particles in traps*, Diploma thesis, Christian-Albrechts-Universität zu Kiel (2008)

[107] T. Fließbach and H. Walliser, *Arbeitsbuch zur Theoretischen Physik* (Spektrum Akademischer Verlag, München, 2004), 1st ed.

[108] Z. Donkó, *Molecular dynamics simulations of strongly coupled plasmas*, J. Phys. A: Math. Theor. **42**, 214029 (2009)

[109] L. Verlet, *Computer "Experiments" on Classical Fluids. I. Thermodynamical Properties of Lennard-Jones Molecules*, Phys. Rev. **159**, 98 (1967)

[110] M. Allen and D. Tildesley, *Computer simulation of liquids* (Oxford University Press, Oxford, 1989)

[111] R. Mannella, *Quasisymplectic integrators for stochastic differential equations*, Phys. Rev. E **69**, 041107 (2004)

[112] N. Metropolis, A. W. Rosenbluth, M. N. Rosenbluth, A. H. Teller, and E. Teller, *Equation of State Calculations by Fast Computing Machines*, J. Chem. Phys. **21**, 1087 (1953)

[113] M. S. Murillo, *Using Fermi Statistics to Create Strongly Coupled Ion Plasmas in Atom Traps*, Phys. Rev. Lett. **87**, 115003 (2001)

[114] F. Robicheaux and J. D. Hanson, *Simulation of the Expansion of an Ultracold Neutral Plasma*, Phys. Rev. Lett. **88**, 055002 (2002)

[115] D. H. E. Dubin, *Effect of correlations on the thermal equilibrium and normal modes of a non-neutral plasma*, Phys. Rev. E **53**, 5268 (1996)

[116] J. P. Schiffer, *Order in confined ions*, J. Phys. B: At. Mol. Opt. Phys. **36**, 511 (2003)

[117] H. Kählert and M. Bonitz, *How Spherical Plasma Crystals Form*, Phys. Rev. Lett. **104**, 015001 (2010)

[118] H. Kählert and M. Bonitz, *Time Evolution from Weak to Strong Coupling in a Spherically Confined Dusty Plasma*, Contrib. Plasma Phys. **51**, 519 (2011)

[119] V. Nosenko, J. Goree, and A. Piel, *Laser method of heating monolayer dusty plasmas*, Phys. Plasmas. **13**, 032106 (2006)

[120] T. E. Sheridan, *Continuum model for the breathing oscillation of a spherical complex plasma*, Phys. Plasmas **13**, 022106 (2006)

[121] D. H. E. Dubin and J. P. Schiffer, *Normal modes of cold confined one-component plasmas*, Phys. Rev. E **53**, 5249 (1996)

[122] P. Hartmann, G. J. Kalman, Z. Donkó, and K. Kutasi, *Equilibrium properties and phase diagram of two-dimensional Yukawa systems*, Phys. Rev. E **72**, 026409 (2005)

[123] T. Ott, M. Stanley, and M. Bonitz, *Non-invasive determination of the parameters of strongly coupled 2D Yukawa liquids*, Phys. Plasmas **18**, 063701 (2011)

[124] O. S. Vaulina and S. A. Khrapak, *Scaling law for the fluid-solid phase transition in Yukawa systems (dusty plasmas)*, J. Exp. Theor. Phys. **90**, 287 (2000)

[125] T. C. Killian, Y. C. Chen, P. Gupta, S. Laha, Y. N. Martinez, P. G. Mickelson, S. B. Nagel, A. D. Saenz, and C. E. Simien, *Ultracold neutral plasmas*, Plasma Phys. Control. Fusion **47**, A297 (2005)

[126] T. Pohl, T. Pattard, and J. M. Rost, *Kinetic modeling and molecular dynamics simulation of ultracold neutral plasmas including ionic correlations*, Phys. Rev. A **70**, 033416 (2004)

[127] V. Tsytovich and G. Morfill, *Dust Self-Organized Structures II. Solutions of Master Equations for Small Diffusion*, Contrib. Plasma Phys. **51**, 723 (2011)

[128] H. Totsuji, C. Totsuji, T. Ogawa, and K. Tsuruta, *Ordering of dust particles in dusty plasmas under microgravity*, Phys. Rev. E **71**, 045401(R) (2005)

[129] H. Totsuji, T. Ogawa, C. Totsuji, and K. Tsuruta, *Structure of spherical Yukawa clusters: A model for dust particles in dusty plasmas in an isotropic environment*, Phys. Rev. E **72**, 036406 (2005)

[130] A. Melzer, M. Klindworth, and A. Piel, *Normal Modes of 2D Finite Clusters in Complex Plasmas*, Phys. Rev. Lett. **87**, 115002 (2001)

[131] H. Kählert and M. Bonitz, *Fluid modes of a spherically confined Yukawa plasma*, Phys. Rev. E **82**, 036407 (2010)

[132] D. H. E. Dubin, *Theory of electrostatic fluid modes in a cold spheroidal non-neutral plasma*, Phys. Rev. Lett. **66**, 2076 (1991)

[133] J. J. Bollinger, D. J. Heinzen, F. L. Moore, W. M. Itano, D. J. Wineland, and D. H. E. Dubin, *Electrostatic modes of ion-trap plasmas*, Phys. Rev. A **48**, 525 (1993)

[134] A. Dantan, J. P. Marler, M. Albert, D. Guénot, and M. Drewsen, *Noninvasive Vibrational Mode Spectroscopy of Ion Coulomb Crystals through Resonant Collective Coupling to an Optical Cavity Field*, Phys. Rev. Lett. **105**, 103001 (2010)

[135] H. Kählert and M. Bonitz, *Collective excitations of a spherically confined Yukawa plasma*, Phys. Rev. E **83**, 056401 (2011)

[136] A. L. Fetter, *Ground state and excited states of a trapped dilute condensed Bose gas*, Czech. J. Phys. **46**, 3063 (1996)

[137] G. Baym and C. J. Pethick, *Ground-State Properties of Magnetically Trapped Bose-Condensed Rubidium Gas*, Phys. Rev. Lett. **76**, 6 (1996)

[138] S. Stringari, *Collective Excitations of a Trapped Bose-Condensed Gas*, Phys. Rev. Lett. **77**, 2360 (1996)

[139] A. Olivetti, J. Barré, B. Marcos, F. Bouchet, and R. Kaiser, *Breathing Dynamics for Systems of Interacting Particles in the Microcanonical and Canonical Descriptions*, Transp. Theory Stat. Phys. **39**, 524 (2011)

[140] G. B. Arfken and H. J. Weber, *Mathematical Methods for Physicists* (Elsevier Academic Press, New York, 2005), 6th ed.

[141] D. H. E. Dubin, *Displacement eigenmodes for cold-fluid and warm-fluid magnetized plasma oscillations*, Phys. Plasmas **12**, 042107 (2005)

[142] M. Abramowitz and I. A. Stegun, eds., *Handbook of Mathematical Functions With Formulas, Graphs, and Mathematical Tables* (National Bureau of Standards, Washington, D.C., 10th printing, 1972)

[143] E. W. Weisstein, *MathWorld—A Wolfram Web Resource*, last accessed Sept. 14, 2011, http://mathworld.wolfram.com (1999–2011)

[144] E. W. Weisstein, *Wolfram Functions—A Wolfram Web Resource*, last accessed Sept. 14, 2011, http://functions.wolfram.com (1998–2010)

[145] E. Barston, *Electrostatic oscillations in inhomogeneous cold plasmas*, Ann. Phys. **29**, 282 (1964)

[146] J. D. Jackson, *Classical Electrodynamics* (Wiley, New York, 1998), 3rd ed.

[147] M. Bonitz, K. Balzer, and R. van Leeuwen, *Invariance of the Kohn center-of-mass mode in a conserving theory*, Phys. Rev. B **76**, 045341 (2007)

[148] A. L. Fetter and D. Rokhsar, *Excited states of a dilute Bose-Einstein condensate in a harmonic trap*, Phys. Rev. A **57**, 1191 (1998)

[149] P. Hartmann, Z. Donkó, K. P. Tierney, C. J. Lee, and G. J. Kalman, *Higher harmonic generation in strongly coupled plasmas*, J. Phys. A: Math. Theor. **42**, 214040 (2009)

[150] R. Ramirez and R. Kjellander, *Effective multipoles and Yukawa electrostatics in dressed molecule theory*, J. Chem. Phys. **125**, 144110 (2006)

[151] W. H. Press, S. A. Teukolsky, W. T. Vetterling, and B. P. Flannery, *Numerical Recipes: The Art of Scientific Computing* (Cambridge University Press, Cambridge, 2007), 3rd ed.

[152] X. Wang, A. Bhattacharjee, and S. Hu, *Longitudinal and Transverse Waves in Yukawa Crystals*, Phys. Rev. Lett. **86**, 2569 (2001)

[153] R. Brout, *Sum Rule for Lattice Vibrations in Ionic Crystals*, Phys. Rev. **113**, 43 (1959)

[154] J. Cioslowski, *Properties of Coulomb crystals: Rigorous results*, J. Chem. Phys. **128**, 164713 (2008)

[155] P. Bakshi, Z. Donkó, and G. J. Kalman, *Einstein frequency distributions for strongly coupled plasmas*, Contrib. Plasma Phys. **43**, 261 (2003)

[156] J. Böning, A. Filinov, P. Ludwig, H. Baumgartner, M. Bonitz, and Y. E. Lozovik, *Melting of Trapped Few-Particle Systems*, Phys. Rev. Lett. **100**, 113401 (2008)

[157] C.-J. Lee and G. J. Kalman, *Nonlinear Quasi-localized Charge Approximation in a Strongly Coupled Classical Bilayer*, J. Korean Phys. Soc. **58**, 448 (2011)

List of Publications

Journal Publications

1. J. Schablinski, D. Block, A. Piel, A. Melzer, H. Thomsen, H. Kählert, and M. Bonitz,
Laser heating of finite two-dimensional dust clusters: A. Experiments
submitted for publication in Phys. Plasmas (2011)

2. H. Thomsen, H. Kählert, M. Bonitz, J. Schablinski, D. Block, A. Piel, and A. Melzer,
Laser heating of finite two-dimensional dust clusters: B. Simulations
submitted for publication in Phys. Plasmas (2011)

3. J. Wrighton, H. Kählert, T. Ott, P. Ludwig, H. Thomsen, J. W. Dufty, and M. Bonitz,
Charge Correlations in a Harmonic Trap,
accepted for publication in Contrib. Plasma Phys. (2011), arXiv:1110.2465

4. T. Ott, M. Bonitz, Z. Donkó, H. Kählert, and P. Hartmann,
Higher Harmonic Generation in Strongly Coupled Magnetized Two-Dimensional Yukawa Liquids,
IEEE Trans. Plasma Sci. **39**, 2768 (2011)

5. H. Bruhn, H. Kählert, T. Ott, M. Bonitz, J. Wrighton, and J. W. Dufty,
Theoretical description of spherically confined, strongly correlated Yukawa plasmas,
Phys. Rev. E **84**, 046407 (2011)

6. H. Kählert and M. Bonitz,
Collective excitations of a spherically confined Yukawa plasma,
Phys. Rev. E **83**, 056401 (2011)

7. H. Kählert and M. Bonitz,
Time Evolution from Weak to Strong Coupling in a Spherically Confined Dusty Plasma,
Contrib. Plasma Phys. **51**, 519 (2011)

8. H. Kählert and M. Bonitz,
Fluid modes of a spherically confined Yukawa plasma,
Phys. Rev. E **82**, 036407 (2010)

9. M. Bonitz, Z. Donkó, T. Ott, H. Kählert, and P. Hartmann,
Nonlinear Magnetoplasmons in Strongly Coupled Yukawa Plasmas,
Phys. Rev. Lett. **105**, 055002 (2010)

10. P. Ludwig, M. Bonitz, H. Kählert, and J. W. Dufty,
Dynamics of strongly correlated ions in a partially ionized quantum plasma,
J. Phys.: Conf. Ser. **220**, 012003 (2010)

11. J. Wrighton, J. W. Dufty, M. Bonitz, and H. Kählert,
Shell Structure of Confined Charges at Strong Coupling,
Contrib. Plasma Phys. **50**, 26 (2010)

12. H. Kählert and M. Bonitz,
How Spherical Plasma Crystals Form,
Phys. Rev. Lett. **104**, 015001 (2010)

13. J. Wrighton, J. W. Dufty, H. Kählert, and M. Bonitz,
Theoretical Description of Coulomb Balls: Fluid Phase,
Phys. Rev. E **80**, 066405 (2009)

14. C. Henning, H. Kählert, P. Ludwig, A. Melzer, and M. Bonitz,
Spectral properties of spherically confined dusty plasma crystals,
J. Phys. A: Math. Theor. **42**, 214023 (2009)

15. H. Kählert, P. Ludwig, H. Baumgartner, M. Bonitz, D. Block, S. Käding, A. Melzer, and A. Piel,
Probability of metastable configurations in spherical three-dimensional Yukawa crystals,
Phys. Rev. E **78**, 036408 (2008)

16. H. Baumgartner, D. Asmus, V. Golubnychiy, P. Ludwig, H. Kählert, and M. Bonitz,
Ground states of finite spherical Yukawa crystals,
New J. Phys. **10**, 093019 (2008)

17. S. Käding, D. Block, A. Melzer, A. Piel, H. Kählert, P. Ludwig, and M. Bonitz,
Shell transitions between metastable states of Yukawa balls,
Phys. Plasmas **15**, 073710 (2008)

18. H. Baumgartner, H. Kählert, V. Golubnychiy, C. Henning, S. Käding, A. Melzer, and M. Bonitz,
Shell Structure of Yukawa Balls,
Contrib. Plasma Phys. **47**, 281 (2007)

Book Chapters

- T. Ott, P. Ludwig, H. Kählert, and M. Bonitz,
Molecular Dynamics Simulation of Strongly Correlated Dusty Plasmas,

in: *Introduction to Complex Plasmas,* M. Bonitz, N. Horing, and P. Ludwig, eds. (Springer, Berlin, 2010)

Selected Contributions to Conferences

- H. Kählert and M. Bonitz,
  Fluid modes of a spherically confined Yukawa plasma,
  talk at 6th International Conference on the Physics of Dusty Plasmas,
  Garmisch-Partenkirchen, May 16–20 (2011)

- H. Kählert and M. Bonitz,
  Fluid Modes of a Spherically Confined Yukawa Plasma,
  poster at 52nd Annual Meeting of the APS Division of Plasma Physics,
  Chicago, IL (USA), November 8–12 (2010)

- H. Kählert and M. Bonitz,
  Normal modes of a confined Yukawa plasma,
  lecture at 2nd Graduate Summer Institute "Complex Plasmas",
  Greifswald, August 5–13 (2010)

- H. Kählert and M. Bonitz,
  Time-dependent correlation buildup in spherical Yukawa balls,
  talk at 51st Annual Meeting of the APS Division of Plasma Physics,
  Atlanta, GA (USA), November 2–6 (2009)

- H. Kählert and M. Bonitz,
  Short-time behavior of spherical Yukawa Balls,
  talk at 13th International Conference on the Physics of Non-Ideal Plasmas,
  Chernogolovka (Russia), September 13–18 (2009)

- H. Kählert, P. Ludwig, H. Baumgartner, and M. Bonitz,
  Probability of metastable states in spherical plasma crystals,
  lecture at Graduate Summer Institute "Complex Plasmas",
  Hoboken, NJ (USA), July 30–August 8 (2008)

Danksagung

Ich möchte mich vor allem bei Prof. Dr. Michael Bonitz für die Aufnahme in seine Arbeitsgruppe und die Betreuung dieser Arbeit bedanken. Seine wertvollen Kommentare und die zahlreichen Diskussionen haben viel zum Verständnis der Materie und zur Entstehung der Ergebnisse beigetragen.

Ein herzlicher Dank geht an alle jetzigen und ehemaligen Mitglieder der Arbeitsgruppe für den freundschaftlichen Umgang und die vielen gemeinsamen Unternehmungen. Neben David Hochstuhl und Torben Ott möchte ich hier Karsten Balzer, Sebastian Bauch, Dr. Henning Baumgartner, Dr. Jens Böning, Dr. Alexei Filinov, Kenji Fujioka, Dr. Christian Henning, Dr. Patrick Ludwig, Lasse Rosenthal, Tim Schoof und Hauke Thomsen erwähnen. Ich danke allen, die bei der Durchsicht der Arbeit geholfen haben.

Weiterhin möchte ich Prof. Dr. James W. Dufty und Dr. Jeffrey Wrighton von der University of Florida danken, durch die ich zusätzliche Einblicke in die Theorie stark gekoppelter Plasmen gewinnen konnte. Für viele interessante Diskussionen und Einblicke in die Experimente danke ich auch den Kollegen aus der Experimentalphysik in Kiel und Greifswald.

Ein abschließender Dank geht an meine Eltern für ihre Unterstützung.

Selbständigkeitserklärung

Hiermit erkläre ich, dass diese Dissertation – abgesehen von der Beratung durch den Betreuer Prof. Dr. Michael Bonitz – nach Inhalt und Form die eigene Arbeit ist.

Außerdem erkläre ich, dass die vorliegende Arbeit weder ganz noch zum Teil bereits einer anderen Stelle im Rahmen eines Prüfungsverfahrens vorgelegen hat. Die hier vorgestellten Ergebnisse sind zum größten Teil bereits in wissenschaftlichen Fachzeitschriften publiziert worden. Eine ausführliche Publikationsliste findet sich auf S. 97 ff.

Die Arbeit ist unter Einhaltung der Regeln guter wissenschaftlicher Praxis der Deutschen Forschungsgemeinschaft entstanden.

Kiel,